Molecular dynamics studies of static and dynamic melting points, using numerical modelling and simulated tampers

Caroline Emma Lumsdon

Doctor of Philosophy

University of York

Physics

September 2021

Abstract

The pressures required for high energy density physics are achieved experimentally using laser shock compression. This is a dynamic process, with picosecond time scales. Establishing a melt temperature in a dynamic system is made non trivial by overshoot of the melting point due to the kinetic barrier for the phase change. There is therefore a need to be able to model dynamic melt temperatures in such a way that a static melt curve can be predicted, and to link these simulations to an experimental method.

By tracking liquid growth to create a numerical melt model, static melt curves of Cu and Ta (in the range 0-10 GPa) were obtained from dynamic heating simulated using molecular dynamics. These were in agreement, within an error of 1%, to literature melt curves and also to the values found using the established static coexistence method, with the computational cost reduced by two orders of magnitude.

A typical shock target consists of an ablator, the target material and a tamper. A shock impedance method was developed to model the tamper as a mobile wall which returned the expected release wave through the bulk material. Different tamper materials could therefore be used to alter the cooling rate during release. With Cu as the test material, the literature melt curve (in the range 50-110 GPa) was recreated, with a 7% error in temperature. This method of modelling a tamper in molecular dynamics removes the need to know the potential of the tamper material.

Both novel methods developed in this thesis have succeeded in reproducing established static melt curves, by modelling dynamic systems. These methods could be applied to laser shock experiments, in order to verify simulated melt curves at high pressures.

Contents

List of Figures

Acknowledgements

This work was supported by the Engineering and Physical Sciences Research Council [EP/L01663X/1] and AWE.

I am extremely grateful to my supervisor, Andrew Higginbotham, for his expertise, guidance and support throughout my PhD. Thank you to the rest of the research group: Ashley Poole, Liam Douglas-Mann and Luca Antonelli. I would also like to thank Andrew Comley, Nigel Woolsey, Chris Murphy, Matthew Selwood and Adam Dearling.

Finally, a huge thank you to my parents and everyone in the CDT.

Declaration

I declare that this thesis is a presentation of original work and I am the sole author. This work has not previously been presented for an award at this, or any other, University. All sources are acknowledged as References.

Chapter 1

Introduction

1.1 Background and motivation

High Energy Density Physics is defined as occurring at pressures greater than 100 GPa. At these high pressures new exotic states are formed, which are pertinent to geology and materials science. The Earth's central pressure is 0.37 TPa and Jupiter's is 4.5 TPa. Knowledge of the melt curve at these pressures is therefore necessary for understanding the structure of planets and the behaviour of their cores. When shocking materials, either to reach high pressure solid phases or for inertial confinement fusion, the melt curve needs to be known. For fusion, melting is required during the first compression stage in order to avoid complex solid state effects such as solid-solid phase transitions.

Laser shock compression is used to reach these high pressures, because they are generally not easily achievable using the more traditional method of a diamond anvil cell. Laser shocks are a dynamic process and interpreting the experimental data to make it applicable for static systems is complex. The melt curve can be accessed directly from the shock, or on release afterwards. In the short timescales involved, thermodynamic equilibrium is not reached. The melt temperature observed is therefore a dynamic rather than static result, caused by an overshoot which is dependent on the rate of temperature change.

Existing methods for determining the static melt curve using molecular dynamics are computationally expensive and have no experimental analogue. A method of modelling shock melting is therefore needed which can be verified by experimental results and which will link dynamic to static melt temperatures. This thesis uses a range of dynamic results to infer the static value. Chapter 3 studies the melt temperature observed at rapid heating rates, and Chapter 4 models melt on release from a tamper after a shock.

Pressures used in this work are relatively low (1-10 GPa in Chapter 3 and 10-100 GPa in Chapter 4) where potentials are known to be accurate, and the focus has been on melting throughout, as it is an easily diagnosed phase change in this pressure range. These conditions were chosen in order to establish proof of principle methods, with the aim of being applicable to higher pressure experiments, and possibly different phase changes.

A shock target's design often includes a tamper. This is used to reduce the free surface expansion or to provide structural support for the target. Rather than the shock wave reaching the back of the target (causing a release wave to return through the target as the surface expands into a vacuum), there is instead a reflected and a transmitted wave generated at the bulk material to tamper boundary, the velocities of which depend on shock impedance.

The tamper therefore has a large effect on the behaviour of the target on release. However, it is often neglected from simulations due to a lack of potentials for the tamper materials (and interaction potentials for the bulk and tamper), and the increased computational cost of a larger simulation box. The proposed tamper method eliminates both of these factors.

Throughout the thesis, the molecular dynamics (MD) code LAMMPS has been used to simulate melting, and this has formed the basis for the rest of the analysis.

1.2 Overview of thesis

The second chapter provides background information: explaining the motivation, previous work and methods used. It has an introduction to high energy density physics, to place this work in context. Each of the results chapters requires an understanding of shock waves, and for this, the elastic response of solids and the propagation of shock waves are described. These are followed by an outline of molecular dynamics, and in particular the code LAMMPS. The simulations carried out in this work depend on shock impedance, dynamic melting and material behaviour on release after a shock, and an overview of each is given in the background.

In Chapter 3, a numerical melt model is developed. The z shaped temperature profile formed during dynamic melting is generated using LAMMPS. A simple melt model tracking the amount of liquid growth is then fitted to it, to obtain the static melt temperature. This novel approach to finding the static melt curve from dynamic MD simulations is tested for Cu and Ta.

Chapter 4 expands upon this method by applying it to an experimental setup, modelling a shocked target with a tamper material to control release. The MD simulations are described and a new method of modelling the tamper is proposed, which would be applicable to other systems incorporating a tamper. From this, the onset of melt for a Cu target is obtained at different cooling rates, corresponding to different tamper materials. A power law fit is used to calculate each static melting point from several dynamic melting points found in MD, implying that a static melt curve could be created from dynamic laser shock experiments.

The conclusion is presented in Chapter 5, in which the methods are summarised and key results reiterated. Suggestions are given to further develop the MD models, and a potential shock-release experiment is described.

Chapter 2

Background

The background chapter begins with an introduction to high energy density physics and shock waves. This is followed by a section on molecular dynamics, focusing on the code LAMMPS which is used throughout the thesis. Background information on dynamic melting (which is needed for Chapter 3) and material behaviour on release after a shock (needed for Chapter 4) is then discussed.

2.1 High energy density physics

In High Energy Density Physics (HEDP), the energy density is on the scale of 1-10 eV, so is comparable to the Fermi energy. It can therefore change chemical bonds and cause ionisation. This occurs at pressures greater than 1 Mbar (100 GPa). As a result, new exotic states are formed, and the insulating properties and chemical processes are altered [1]. Pressures over 10 Mbar give rise to such extreme conditions that electride structures are created, in which strong interaction between valance and core electrons leads to a localisation of electron density, effectively producing anions.

As well as opening up possibilities for materials science, these pressures are also relevant to geology. The central pressures of the planets fit into this category, at 0.37 TPa for Earth and 4.5 TPa for Jupiter. These pressures are not routinely achievable experimentally using a diamond anvil cell, the traditional method of accessing high pressures, but they can be reached by using laser compression to produce a shock wave with velocity greater than 10km/s. HEDP is studied by both simulations and laser experiments.

2.2 Achieving high pressures experimentally

2.2.1 Diamond Anvil Cells

A well established method for achieving static compression is to use a Diamond Anvil Cell (DAC), for which the typical set up is shown in figure 2.1. Diamonds have a high compressive strength and hardness, and are also transparent to visible light, UV and X-rays, meaning DACs can be used with a range of diagnostics. One such diagnostic is a ruby pressure gauge. The wavelength of the fluorescence emission of a ruby, placed alongside the target material, changes with pressure and can be calibrated [2]. Normal use of a DAC is below 100 GPa [1]: it is difficult but possible to achieve pressures over 200 GPa and in a few experiments over 600 GPa [1, 3], the limiting factor being diffusion between the diamond and the target. However, reaching these higher pressures is more easily carried out using dynamic methods.

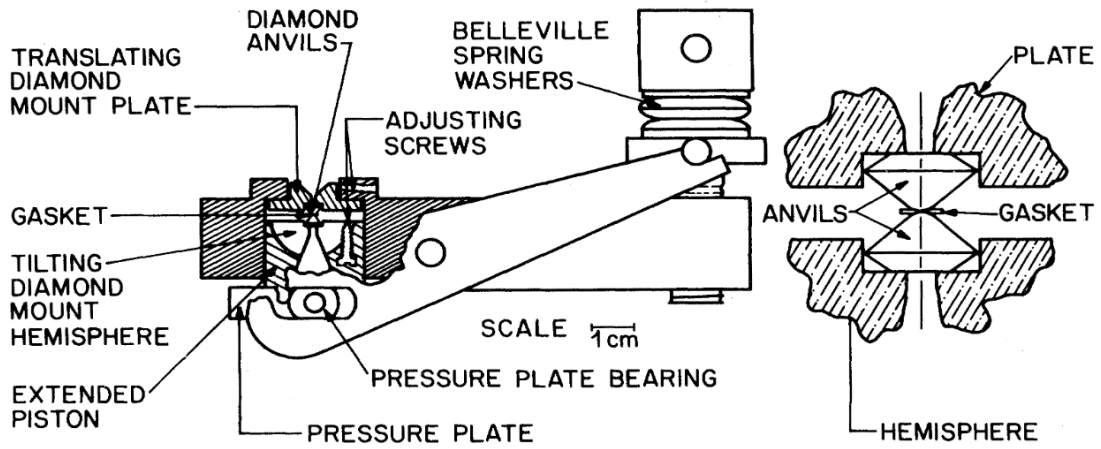

Figure 2.1: Diagram of a typical Diamond Anvil Cell showing the main pressure loading components, with a close up (right) of the diamond anvils and the target carrying gasket [4]. (Reprinted figure with permission from A. Jayaraman, Reviews of Modern Physics, 55, 67, 1983. Copyright 1983 by the American Physical Society.)

2.2.2 Laser compression

The rapid deposition of energy from a laser onto the surface of a material causes ablation. Due to conservation of momentum, a shock wave is then driven into the material.

The initial absorption mechanism is multiphoton absorption, by which the laser produces free electrons and ions in the timescale of femtoseconds. Multiphoton absorption can occur for intensities greater than $10^{10} W/cm^2$, as at this intensity the probability of multiple photons interacting with an atom at the same time becomes significant. The energy absorbed from the photons needs to be greater than the sum

of the ionisation potential and the ponderomotive potential in order to release an electron, and for typical laser energies multiple photons are required.

As the free electrons expand into the vacuum, they oscillate in the electric field of the laser, gaining energy through inverse Bremsstrahlung absorption; radiation is absorbed by an electron while in the Coulomb field of an ion, causing the electron to accelerate. This generates more free electrons through cascade ionisation due to impacts between the free electrons and atoms. Inverse Bremsstrahlung absorption is more prevalent in the presence of ions than atoms, so the further ionisation enhances laser coupling.

Many factors affect the pressure achieved by the laser, such as the laser-target coupling, laser pulse temporal shape and intensity [5]. The pressure obtainable (in GPa) can be calculated from scaling laws such as

$$P = 860 \left(\frac{I(W/cm^2)}{10^{14}} \right)^{2/3} (\lambda(\mu m))^{-2/3} \left(\frac{A}{2Z} \right)^{1/3} \tag{2.1}$$

where I is the laser intensity, λ is the laser wavelength, and A and Z are the mass number and the atomic number of the target material [6]. This is shown in figure 2.2 for an infrared laser with a mid-Z element target. Pressure has a strong dependence on laser parameters and a weaker dependence on the material properties. Equation 2.1 is only valid below the ablation pressure limit of $10^{14} W/cm^2$, because above this pressure the coupling between the target and the laser decreases.

Other methods of dynamic compression include using Z-pinch or explosives, but laser compression is the focus of this thesis.

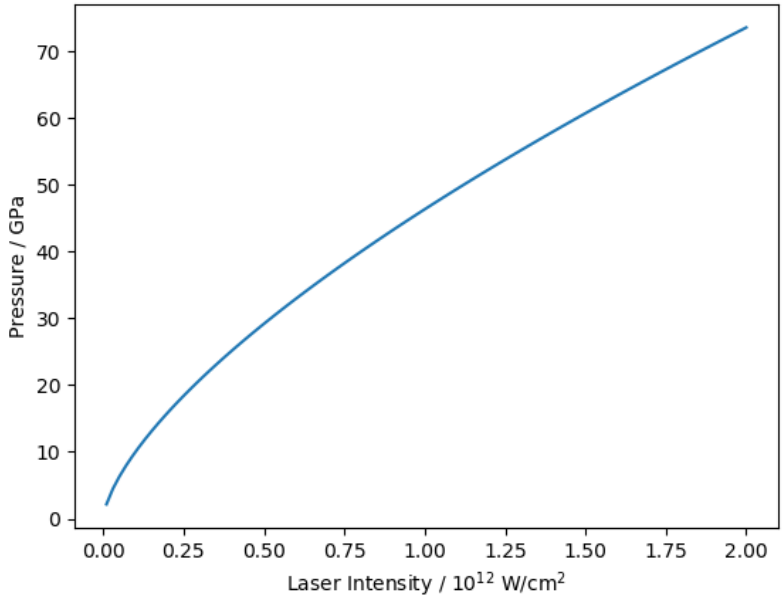

Figure 2.2: An example of the scaling law given in equation 2.1 for an infrared laser ($\lambda = 0.8\mu m$) with A=2Z .

2.3 Shock Waves

A shock wave has a rise time so rapid that it causes a discontinuity in pressure, strain, velocity and temperature [7]. The wave speed, c, in a gas is related to pressure, P, and density, ρ, by γ, the adiabatic index (the ratio of the constant pressure to constant volume specific heat capacities).

$$c = \left(\frac{\gamma P}{\rho}\right)^{1/2} \tag{2.2}$$

Therefore in the shocked region, where pressure is increased, the shock speed increases. This positive feedback increases the pressure gradient, forming the pressure discontinuity. Typically shocks only form in compression, as a decompression causes the shock speed to decrease as pressure decreases.

2.3.1 Rankine-Hugoniot Equations

The Rankine-Hugoniot relationships occur as a result of conserving mass, momentum and energy across the shock discontinuity. U_s is the shock velocity and u_p is the particle velocity. ρ, P and e are the density, pressure and specific internal energy (with subscripts 0 and 1 for before and after the shock passes through the material). A is the cross sectional area and δt is the time step.

Conserving mass before and after the shock

$$\rho_1 A\delta t(U_s - u_p) = \rho_0 A\delta t U_s \tag{2.3}$$

$$(U_s - u_p)\rho_1 = U_s\rho_0 \tag{2.4}$$

The increase in momentum (left in equation 2.5) is equal to the impulse from the shock front (right)

$$u_p(U_s\rho_0 A\delta t) = (P_1 - P_0)A\delta t \tag{2.5}$$

$$P_1 - P_0 = \rho_0 U_s u_p \tag{2.6}$$

And equating the energy increase with the work done by the piston gives

$$\rho_0 A\delta t U_s \left(e_1 - e_0 + \frac{1}{2}u_p^2\right) = P_1 u_p A\delta t \tag{2.7}$$

$$P_1 u_p = \rho_0 U_s \left(e_1 - e_0 + \frac{u_p^2}{2}\right) \tag{2.8}$$

Together equations 2.4, 2.6 and 2.8 are the Rankine-Hugoniot relationships. From these, the Hugoniot equation can be formed by combining to eliminate U_s and u_p.

2.3.2 Shock waves in an ideal gas

Before looking at how shock waves propagate in a solid, it is easier to consider an ideal gas. The ideal gas approximation

$$e = \frac{1}{\gamma - 1}\frac{P}{\rho} \tag{2.9}$$

is used with the Rankine Hugoniot equations, to form the Hugoniot equation of an ideal gas

$$\frac{\rho_1}{\rho_0} = \frac{(\gamma + 1)\frac{P_1}{P_0} + (\gamma - 1)}{(\gamma + 1) + (\gamma - 1)\frac{P_1}{P_0}} \tag{2.10}$$

For a monatomic gas

$$\gamma = \frac{5}{3}$$

At infinite pressure

$$\frac{\rho_1}{\rho_0} = \frac{\gamma + 1}{\gamma - 1} = 4 \tag{2.11}$$

so the limit of compression for a single shock in an ideal monatomic gas is fourfold.

2.3.3 Shock waves in a solid

Shock velocity, U_s, is found to be linear with particle velocity, u_p, for most materials.

$$U_s = Su_p + c_0 \tag{2.12}$$

This linear relationship is an approximation, with S and c_0 as constants, and is shown for Cu in figure 2.3.

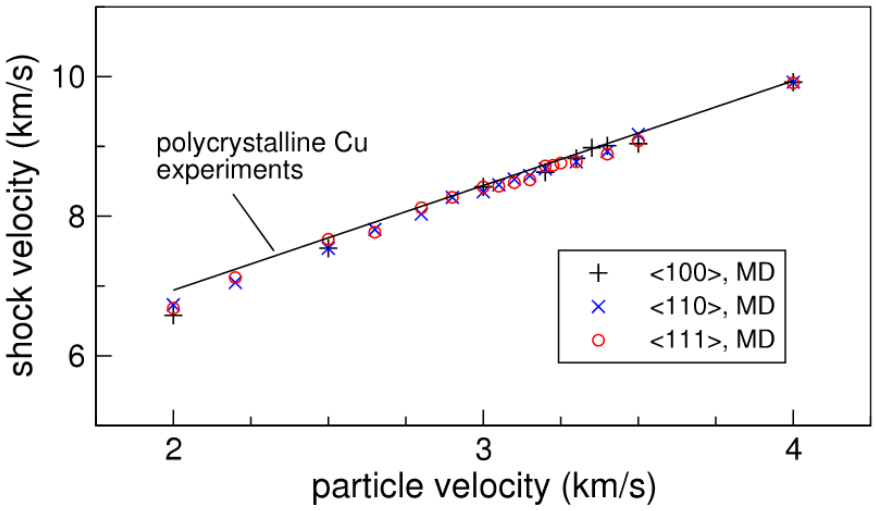

Figure 2.3: The linear relationship between shock velocity, U_s, and particle velocity, u_p, for Cu from experimental data (solid line) and MD (data points) [8]. This graph shows close agreement between each of the three crystallographic directions simulated (shown in the legend), and the multidirectional polycrystalline experiments. (Figure from Q. An, S. N. Luo, L. B. Han, L. Zheng and O. Tschauner, Melting of Cu under hydrostatic and shock waveloading to high pressures, Journal of Physics: Condensed Matter, 20, 095220, 2008. IOP Publishing. Reproduced with permission. All rights reserved.)

The propagation of a shock wave in a solid depends on its elasticity. Young's modulus, E, is defined as the ratio of stress, σ, to strain, ϵ,

$$E = \frac{\sigma}{\epsilon} \tag{2.13}$$

and it is related to the bulk modulus, K, and the shear modulus, μ, by Poisson's ratio, ν. The bulk modulus is a measure of the material's resistance to compression, and shear modulus is its resistance to shear deformation.

$$E = 2\mu(1+\nu) = 3K(1-2\nu) \tag{2.14}$$

The speed of sound, c, in a solid is dependent on these values, and density, ρ. For longitudinal waves

$$c_{longitudinal} = \sqrt{\frac{K + \frac{4}{3}\mu}{\rho}} \tag{2.15}$$

and for transverse waves

$$c_{transverse} = \sqrt{\frac{\mu}{\rho}} \tag{2.16}$$

For a one dimensional solid, the sound speed of a pressure wave can be simplified to

$$c_{solid} = \sqrt{\frac{E}{\rho}} \tag{2.17}$$

For a liquid, the bulk modulus is required instead of E, and for a gas γP where P is pressure and γ is the adiabatic index.

$$c_{liquid} = \sqrt{\frac{K}{\rho}} \tag{2.18}$$

$$c_{gas} = \sqrt{\frac{\gamma P}{\rho}} \tag{2.19}$$

Equation 2.13 can also be written with an elasticity tensor, C, linking stress, σ, and strain ϵ

$$\sigma = C\epsilon \tag{2.20}$$

In a cubic system, only three components of C are independent and non-zero (C_{11}, C_{12} and C_{44}). The bulk modulus, K, and shear modulus, μ, can be expressed in terms of these components

$$K = \frac{1}{3}(C_{11} + 2C_{12}) \tag{2.21}$$

$$\mu = C_{44} \tag{2.22}$$

From the definition of the bulk modulus as volumetric stiffness in terms of pressure, P,

$$K = -v\frac{dP}{dv} = \rho\frac{dP}{d\rho} \tag{2.23}$$

where v is the specific volume

$$v = \frac{1}{\rho} \tag{2.24}$$

The bulk modulus is found experimentally to be approximately linear with pressure [9], so can be written as

$$K(P) = K_0 + K_0' P \tag{2.25}$$

where K_0 and K_0' are constants. Substituting this into equation 2.23,

$$\frac{d\rho}{\rho} = \frac{dP}{K_0 + K_0' P} \tag{2.26}$$

which integrates to form the Murnaghan equation of state [9]

$$P(\rho) = \frac{K_0}{K_0'} \left[\left(\frac{\rho}{\rho_0} \right)^{K_0'} - 1 \right] \tag{2.27}$$

where ρ_0 is the initial density.

Using equation 2.12, the equation of state (equation 2.27) can be rearranged in order to find K_0 and K_0' in terms of the constants c_0 and S. To do this equations 2.28 and 2.29 are also needed.

$$P = \rho_0 U_s u_p \tag{2.28}$$

$$u_p = \left(1 - \frac{\rho_0}{\rho} \right) U_s \tag{2.29}$$

From this it can be shown that

$$P(\rho) = \frac{\rho_0 c_0^2 \left(1 - \frac{\rho_0}{\rho} \right)}{\left(1 - S \left(1 - \frac{\rho_0}{\rho} \right) \right)^2} \tag{2.30}$$

By making a substitution to use strain, ϵ, instead of density, where

$$\epsilon = 1 - \frac{\rho_0}{\rho} \tag{2.31}$$

and finding the binomial expansion of equations 2.27 and 2.30, then equating the first and second order terms of ϵ, the values of K_0 and K_0' can be expressed as

$$K_0 = \rho_0 c_0^2 \tag{2.32}$$

$$K_0' + 1 = 4S \tag{2.33}$$

linking the wave velocity with the material's resistance to compression [9].

As with an ideal gas, the Rankine-Hugoniot relationships for a solid can be found by conserving mass, momentum and energy [10]. The Hugoniot, which describes the possible end states from a single shock, can be obtained from these equations. Additional shocks would form another Hugoniot, beginning at the end state of the previous shocks. The Cu Hugoniot [11] is given as an example in figure 2.4.

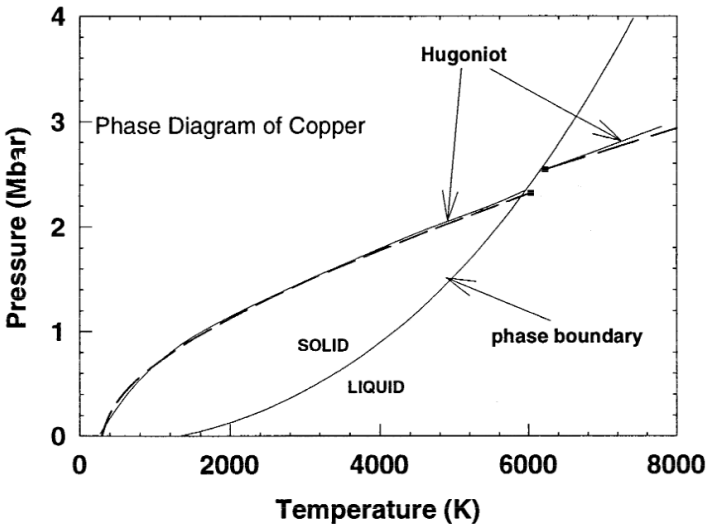

Figure 2.4: The phase diagram of Cu, showing the solid and liquid phases and the Hugoniot up to 4 Mbar (400 GPa). The dashed and solid lines show two different studies which closely agree [11]. The Hugoniot jumps at the phase transition. (Reprinted from D. Hayes, R. S. Hixson and R. G. McQueen. High pressure elastic properties, solid-liquid phase boundary and liquid equation of state from release wave measurements in shock-loaded copper. AIP Conference Proceedings, 505:483, 2000, with the permission of AIP Publishing.)

2.4 Molecular Dynamics

Molecular Dynamics (MD) is based on the equations of motion, and was developed in the 1950s [12]. It has an advantage over similar techniques, such as the Monte Carlo method, in that MD allows access both to thermodynamic properties and time-dependent effects [12]. In 1959, MD was limited to running simulations with fewer than 500 molecules, due to the memory capacity and speed of the computers available [13]. Now, however, simulations with over 10^9 particles are possible [14], allowing MD studies of HEDP to precede experimental work.

MD applies Newton's equations of motion to a set of interacting particles. The simplest way this can be expressed algebraically is

$$x_{i+1} = x_i + \delta_t v_i \tag{2.34}$$

$$v_{i+1} = v_i + \frac{\delta_t F(x_i)}{m} \tag{2.35}$$

to define the position, x, and velocity, v, of each atom, of mass m, for subsequent time steps.

The force, F, acting on an atom is calculated from the gradient of the potential,

E,

$$F = -\nabla E \tag{2.36}$$

LAMMPS uses the more complex Verlet method of time integration, which applies the central difference approximation rather than the forward difference approximation used in the previous equations.

$$\frac{\Delta^2 \boldsymbol{x}_n}{\Delta t^2} = \frac{\dfrac{\boldsymbol{x}_{n+1} - \boldsymbol{x}_n}{\Delta t} - \dfrac{\boldsymbol{x}_n - \boldsymbol{x}_{n-1}}{\Delta t}}{\Delta t} = \frac{\boldsymbol{x}_{n+1} - 2\boldsymbol{x}_n + \boldsymbol{x}_{n-1}}{\Delta t^2} = \boldsymbol{a}_n \tag{2.37}$$

This therefore determines the next position vector from the previous two

$$\boldsymbol{x}_{n+1} = 2\boldsymbol{x}_n - \boldsymbol{x}_{n-1} + \boldsymbol{a}_n \Delta t^2 \tag{2.38}$$

It incorporates the acceleration, $\mathbf{a}_n$, determined by the potential, but not the velocity.

Quantum MD is possible using a potential which accounts for quantum effects. An alternative to quantum MD is Density Functional Theory (DFT), which is based on electron structure. Similar simulations to those which are described in this thesis, notably for coexistence and Z-method of melting, are routinely carried out in DFT [15, 16] as well as in MD.

2.4.1 LAMMPS

LAMMPS (Large scale Atomic/Molecular Massively Parallel Simulator) is a classical MD code distributed by Sandia National Laboratories [17]. LAMMPS can model particles in a solid, liquid or gas, using a variety of force fields and boundary conditions to simulate different systems [18]. It is derived from classical dynamics, and the atomic interactions are modelled from the inputted potential and initial parameters.

MD calculates the positions and velocities of all the particles at each time step. These can then be converted to macroscopic properties, such as pressure and energy, by statistical mechanics [12]. This classical method produces a good match for experimental results, even for metals where quantum effects would be expected to be significant [17].

Alternatives to LAMMPS include Amber, DL_POLY, Gromacs and NAMD. The older codes (such as Amber and early versions of DL_POLY) use the replicated data model, which requires all atomic information to be replicated on all processors. More recent codes (including DL_POLY version 4 [19], NAMD and LAMMPS),

use spatial domain decomposition techniques, so that the amount of atomic data stored on each processor is approximately inversely proportional to the number of processors [12].

LAMMPS uses neighbour lists to keep track of nearby particles, within a cut off distance, in order to calculate the force the atoms are exerting on each other. The lists are optimised for systems with particles that are repulsive at short distances, so that the local density never becomes too large. When run in parallel, LAMMPS partitions the simulation domain into three dimensional sub-domains, one for each processor. The processors communicate and store information for ghost atoms that border their sub-domain [18].

2.4.2 Potentials

The force experienced between a pair of atoms, within a set cut-off distance, is described using a potential. These have a range of complexity: two commonly used ones are the Leonard-Jones potential and the EAM (Embedded Atom Model) potential. The Leonard-Jones potential is one of the simplest, and describes interatomic energies as

$$E = 4A\left(\left(\frac{B}{r}\right)^{12} - \left(\frac{B}{r}\right)^{6}\right) \tag{2.39}$$

below the cutoff distance, where r is the distance between atoms and A and B are constants. The minimum of this potential occurs at $r = 2^{1/6}B$ where $E = -A$.

EAM potentials use the formula

$$E_i = F_\alpha\left(\sum_{j\neq i}\rho_\beta(r_{ij})\right) + \frac{1}{2}\sum_{j\neq i}\phi_{\alpha\beta}(r_{ij}) \tag{2.40}$$

The embedding energy, F, is a function of the electron density, ρ, and the pair potential interaction, ϕ. α and β are the elements of the atoms i and j. This method incorporates the electron cloud, as well as the pair interactions between atoms, and so is more accurate than the Leonard-Jones potential for modelling metals [20].

These potentials are found either empirically by matching with experimental data or from quantum mechanics using DFT. Potentials only have guaranteed accuracy for the pressure range over which they were modelled. Accuracy tends to decrease at pressures above 100 GPa, due to a lack of experimental data.

2.4.3 Ensembles

Possible ensembles are NVT, NVE, NPH and NPT. The letters refer to the properties which are held constant. N is the number of atoms, V is volume, T is temperature, E is the total energy of the system, P is pressure and H is the enthalpy.

NVT, the canonical ensemble, is used for a system that is in thermal equilibrium with a heat bath. The NVE is the microcanonical ensemble, which has an exactly specified total energy. NPH, the isoenthalpic–isobaric ensemble, maintains constant enthalpy and constant pressure. Enthalpy is defined as

$$H = E + PV \tag{2.41}$$

The isothermal–isobaric ensemble, NPT, is useful for measuring the equation of state.

2.4.4 Box Size

By applying periodic boundary conditions, which mean that if an atom passes through one side of the simulation box it will reappear on the opposite side, a smaller number of atoms can be used to represent a much larger system and thus reduce the run time of the simulation. When a system is anisotropic, for example if a shock wave is travelling in one direction, the boundaries in that direction cannot be periodic. In this case, the boundaries would be either fixed and atoms passing through would be lost, or shrink-wrapped so the box size grows in this direction to accommodate atoms that would otherwise escape.

Increasing the number of atoms in a simulation reduces thermal noise, as the distribution of velocities becomes closer to the ideal Gaussian distribution. The box must be larger than the cutoff distance of the potential, otherwise an atom will be exerting a force on itself.

In each simulation, a seed is needed to randomly distribute the initial velocity of the atoms, with the mean velocity determined by the temperature. Running simulations with different velocity seeds, and then taking an average of the results, provides a method of reducing thermal noise without increasing the box size.

For melting to take place, a certain number of defects (such as lattice vacancies, interstitials and dislocations) need to be present in the regular pattern of the crystal structure [21]. Figure 2.5 shows that the fraction of these defective atoms, α_d, needed to trigger melting is the same for two different box sizes, but occurs at a higher temperature for the larger simulation box. This increase in melting temperature

with box size is shown in figure 2.6.

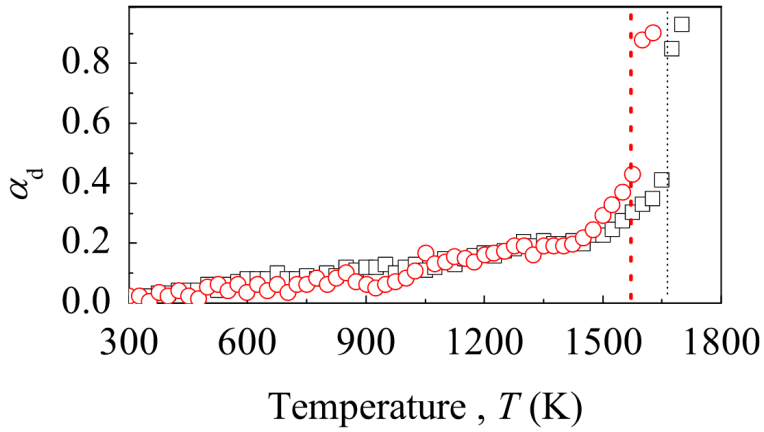

Figure 2.5: The fraction of defective atoms, α_d, as a function of the temperature for Cu MD simulations with 500 atoms (circles) and 6912 atoms (squares) [21]. The vertical jumps show melting, with a higher melting temperature for the larger box size, in agreement with figure 2.6. (Reprinted with permission.)

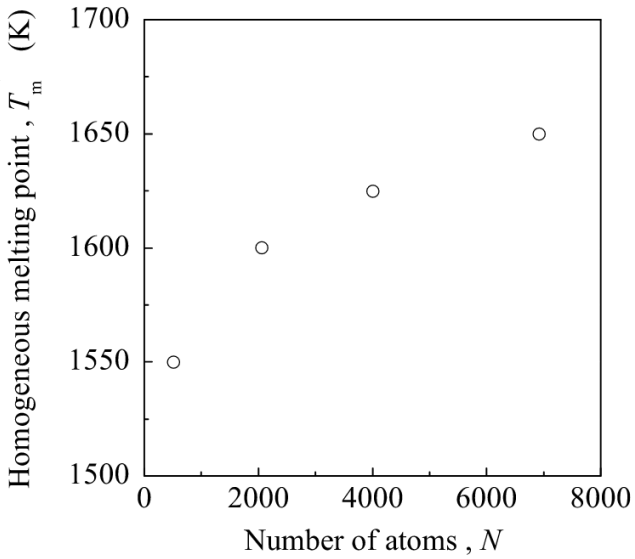

Figure 2.6: Dependence of homogeneous melting in Cu on box size in MD [21]. The melting point increases with box size, with a stronger size dependence for a smaller box. (Reprinted with permission.)

While figure 2.6 shows that a smaller number of atoms leads to a lower melting point, if the simulation size is not sufficiently large then melting will be suppressed because phonons with a wavelength longer than the simulation cell cannot be modelled [22].

2.4.5 Shock Waves in LAMMPS

There are three mechanisms that can be used to create a shock compression in LAMMPS: a momentum mirror, a constant force piston and a constant velocity piston [18]. A momentum mirror forms a wall which will, if an atom from the bulk moves through the wall, reflect it back into the bulk material with the same speed. This carries out the same function as the constant velocity piston. Experimentally, a laser is more intuitively described as a constant force piston, as the laser intensity determines the ablation pressure, and therefore the driving force. In practice, all three systems produce the same results.

Alternatively, target pressures can be reached using barostatting (and temperatures by thermostatting). The Hugoniostat utilises a thermostat, barostat or both to reach a P-T point on the Hugoniot for a given pressure [23], from which time dependent temperatures satisfying the Rankine Hugoniot equations can be reached [18].

$$T_t - T = \frac{\frac{1}{2}(P + P_0)(V_0 - V) + e_0 - e}{N_{dof} k_B} \tag{2.42}$$

where N_{dof} is the number of degrees of freedom, and T and T_t are the instantaneous and target temperatures. For pressure, volume and internal energy, P_0, V_0 and e_0 are the reference values, P, V and e are the instantaneous values.

2.5 The Kinetics of Melting

2.5.1 Homogeneous and Heterogeneous Melting

There are two types of melting: homogeneous and heterogeneous. Heterogeneous melting occurs at a boundary, such as a dislocation or a grain boundary. Homogeneous melting has a higher nucleation energy barrier, and is therefore less common in real materials, as these will generally have imperfections which allow heterogeneous melting. However, it is useful to study homogeneous melting for the parameters that can be extracted from it, which also apply to heterogeneous melting. Homogeneous melting can be simulated more easily, and will be the focus of this thesis as it is the dominant type of melting in a dynamic system where the solid is superheated.

The upper limit of superheating for homogeneous melting is set by a series of instabilities in the crystal structure. The rigidity catastrophe (due to the vanishing shear modulus) and the kinetic instability (from the vibrations breaking up the lattice) are the first to be reached, so cause the onset of melting [1]. Instabilities which occur at higher temperatures than these are the isochoric, isenthalpic and isentropic conditions, which occur at the temperatures where the solid and liquid

have the same volume, enthalpy and entropy respectively [24].

In homogeneous nucleation, for a melted region to remain liquid and then grow, it must be larger than the critical radius.

2.5.2 The Critical Radius

At the point of melting, energy is needed to overcome the nucleation barrier. The solid-liquid interface of a nucleation site has an associated energy, so the liquid region must be sufficiently large, greater than the critical radius, in order not to solidify. The critical size of a nucleus is predicted to have 200-500 particles for homogeneous nucleation [24]. This size is determined by the Gibbs free energy.

The Gibbs free energy of the total system is

$$G = U - TS + PV \tag{2.43}$$

where U and S are the total energy and entropy. T, P and V are temperature, pressure and volume. The Gibbs free energy of two phases excluding the interface is

$$G_b = \mu N \tag{2.44}$$

where μ is the chemical potential and N is the number of moles [25]. The interface tension, σ, can be defined by this difference

$$\sigma A = G - G_b \tag{2.45}$$

where A is the area of the interface. The free energy difference between the initial (crystal) and final (liquid) state is

$$\Delta G_V = G_l - G_c \tag{2.46}$$

The energy of fusion, ΔE_F, can be seen for Fe in figure 2.7 as the jump in total energy at the homogeneous melting temperature, T_{hm} [26]. It is this energy which is lost as latent heat in a first order phase transition.

To form a liquid sphere in a perfect lattice, the total Gibbs free energy change is

$$\Delta G(t) = \frac{4}{3}\pi r^3(\Delta G_V + \Delta E_F) + 4\pi r^2 \gamma_{sl} \tag{2.47}$$

where γ_{sl} is the interface energy [27].

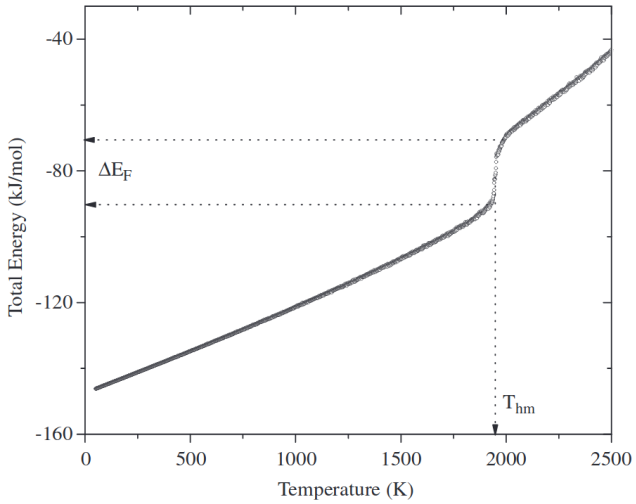

Figure 2.7: Melting curve for BCC Fe, showing the increase in energy with temperature [26]. The large jump in energy (the energy of fusion, ΔE_F) occurs during melting, at the homogeneous melt temperature T_{hm}. (Reprinted from Physica B, 407, T. P. Duy and V. V. Hoang, Atomic mechanism of homogeneous melting of BCC Fe at the limit of superheating, 978, Copyright 2012, with permission from Elsevier.)

This gives a critical radius, the value of r where $\Delta G(t)$ is at a maximum, of

$$r^*(T) = \frac{-2\gamma_{sl}}{\Delta G_V + \Delta E_F} \tag{2.48}$$

which corresponds to a critical energy of nucleation

$$\Delta G^*(T) = \frac{16\pi\gamma_{sl}^3}{3(\Delta G_V + \Delta E_F)^2} \tag{2.49}$$

ΔE_F can be expressed by the elastic properties of the material

$$\Delta E_F = \frac{(18\mu K\epsilon^2 f)}{(4\mu + 3K)} \tag{2.50}$$

μ and K are the shear and bulk moduli, f accounts for a free surface (so is 1 in the case of homogeneous nucleation), and ϵ is the hydrostatic strain due to the change in volume.

ΔG_V can be approximated by using the enthalpy change of fusion ΔH_M

$$\Delta G_V \sim \frac{\Delta H_M(T_m - T)}{T_m} \tag{2.51}$$

if the difference in heat capacity between the solid and liquid is ignored [27].

2.5.3 Criteria of Melting

One way of defining melting is the Lindemann criterion, which states that melting occurs when the root mean square displacement of the atoms reaches a critical fraction of the interatomic distance. This is due to melting being a vibrational lattice instability [1]. The value of Lindemann's constant, the critical fraction c_L, depends on the element; a typical value is around 0.1 [28].

This can be quantified assuming all atoms vibrate around their equilibrium position with the same frequency ν_E, the Einstein frequency.

$$E = 4\pi^2 m\nu_E^2 < u^2 >= k_B T \tag{2.52}$$

where $< u^2 >$ is the mean square thermal average amplitude of vibration, E is average thermal energy and m is the atomic mass. From the Lindemann criterion, at the onset of melting

$$< u^2 >= c_L a^2 \tag{2.53}$$

where a is the lattice parameter, so the melt temperature can be calculated as

$$T_m = \frac{4\pi^2 m\nu_E^2 c_L a^2}{k_B} \tag{2.54}$$

The relationship between the mean square displacement (called the Lindemann ratio), and the temperature at the onset of melt, T_{on}, and at full homogeneous melt, T_{hm} is shown in figure 2.8.

The Born criterion uses the structural definition of melt, based on a liquid, unlike a crystal, having no resistance to shear stress. It is dependent on the bulk modulus, K, the shear modulus, μ, and the shear elastic coefficients C_{11}, C_{12} and C_{44}, described in section 2.3.3. The stability criteria for a lattice are

$$K = \frac{1}{3}(C_{11} + 2C_{12}) > 0 \tag{2.55}$$

$$C_{11} - C_{12} > 0 \tag{2.56}$$

$$\mu = C_{44} > 0 \tag{2.57}$$

Melt occurs when these criteria are not met, and it has been shown that equation 2.56 fails first, so it is this condition which causes structural melting [29]. The shear modulus, μ, of Cu is shown in figure 2.9, during melting. The shear modulus decreases on approaching the melt curve, and the solid to liquid transition is inter-

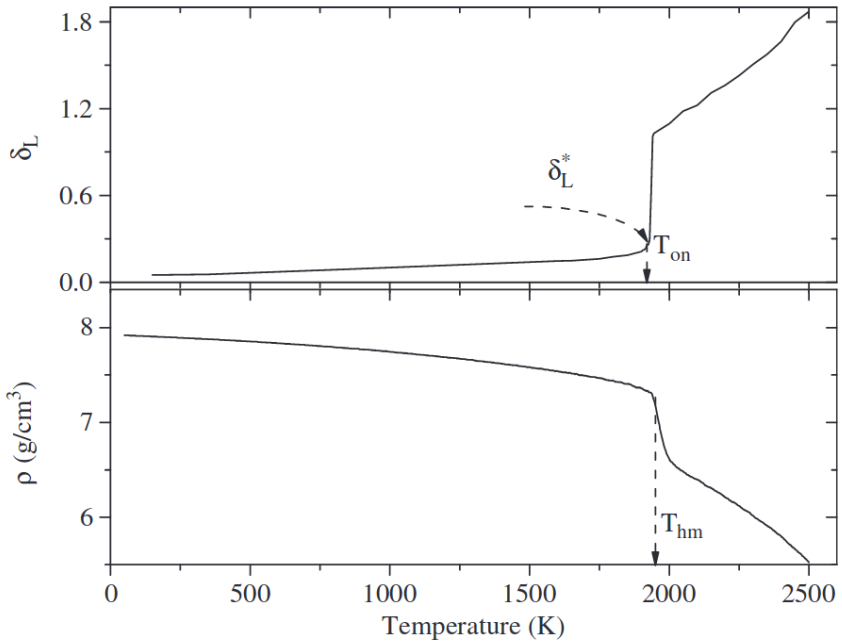

Figure 2.8: Lindemann ratio, δ_L, and density, ρ, as a function of temperature for Fe. The critical value of the Lindemann ratio is labelled δ_L^* [26]. The temperature at onset of melt, T_{on}, and the temperature of full homogeneous melt, T_{hm} are also marked. (Reprinted from Physica B, 407, T. P. Duy and V. V. Hoang, Atomic mechanism of homogeneous melting of BCC Fe at the limit of superheating, 978, Copyright 2012, with permission from Elsevier.)

preted as occurring when the shear modulus reaches zero [11].

The Born and Lindemann criteria are met at the same temperature when a surface free crystal is heated, causing homogeneous melting. This temperature is the limit of superheating [30].

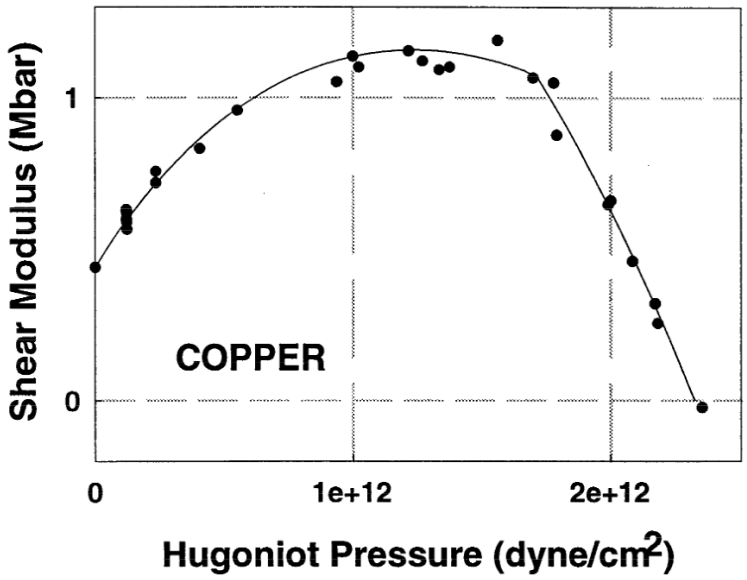

Figure 2.9: The experimental Cu shear modulus along the Hugoniot shown approaching the solid-liquid transition where the shear modulus = 0 [11]. 1 dyne/cm^2 = 0.1 Pa. (Reprinted from D. Hayes, R. S. Hixson and R. G. McQueen. High pressure elastic properties, solid-liquid phase boundary and liquid equation of state from release wave measurements in shock-loaded copper. AIP Conference Proceedings, 505:483, 2000, with the permission of AIP Publishing.)

2.6 Diagnosing Melting

2.6.1 Diagnosing Melt in Simulations

The mean square displacement (MSD) of a group of atoms can be used to determine if they are in a solid or liquid environment, due to the Lindemann criteria.

$$MSD = \frac{1}{N}\sum_{i=0}^{N}\left(dx_i^2 + dy_i^2 + dz_i^2\right) \tag{2.58}$$

for N atoms, with displacements dx, dy and dz from each atom's initial position. As the solid is heated, MSD will increase. There is then a sharp rise upon melting, after which the MSD will continue to increase, with a steeper gradient than when solid.

The centro-symmetry parameter (CSP) gives another way melting can be identified. As it is a measure of the disorder of a system, it can determine whether an atom is in a crystal or a liquid environment (although it could not be used to distinguish between liquid and an amorphous solid). For a perfect structure which is centrosymmetric about each atom, CSP = 0.

It is calculated using the equation

$$CSP = \sum_{i=1}^{N/2} |\mathbf{R}_i + \mathbf{R}_{i+N/2}|^2 \tag{2.59}$$

for N nearest neighbours whose positions are given by the vectors $\mathbf{R}$. CSP has a similar temperature dependence to MSD, but can be used to track individual atoms rather than just groups. The distribution of CSP is useful as well as the mean value; a liquid histogram shows a broader range of CSP than a solid.

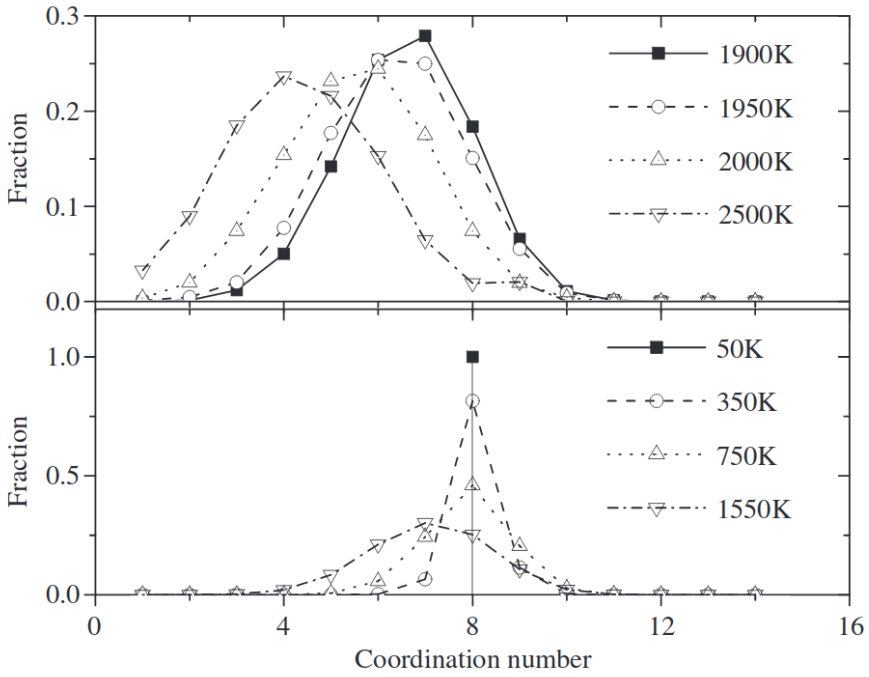

Figure 2.10: Change in coordination number with increasing temperature for Fe, shown over two plots for clarity. The single point at 8 is for a BCC solid, and this decreases and broadens during melting [26]. Broadening also takes place with disorder caused by increasing temperature, prior to melting. (Reprinted from Physica B, 407, T. P. Duy and V. V. Hoang, Atomic mechanism of homogeneous melting of BCC Fe at the limit of superheating, 978, Copyright 2012, with permission from Elsevier.)

The coordination number is a further way of diagnosing melt. It is the number of atoms a central atom is bonded to. In a crystal lattice the coordination number will be known (eg. 12 for FCC and 8 for BCC). This will change during melt as demonstrated in figure 2.10 for an MD simulation of Fe [26]. Defects will alter the coordination number slightly, and a change of phase will see a larger shift. Amorphous materials such as a liquid have a broad profile of coordination numbers.

The CSP and coordination number of each atom can be obtained from LAMMPS,

and MSD can be found for a group of atoms. In all cases, solid and liquid regions can be differentiated, although the exact point of transition has some uncertainty, as thermal effects and defects in the solid give the lattice a more liquid like structure.

2.6.2 X-Ray Diffraction

X-Ray Diffraction (XRD) is a technique that allows melt to be observed experimentally by determining the atomic structures of materials. It can be used *in situ*, at the pressures achieved by a diamond anvil cell or through laser compression. The readings can be carried out in femtoseconds, so this diagnostic can take multiple measurements over nanosecond timescales, making it ideal for dynamic shock experiments.

The diffraction pattern of a material can be simulated by taking a Fourier transform, $F(\mathbf{q})$, [31].

$$I(\mathbf{k}_s) \propto |F(\mathbf{q})|^2 \propto \left| \sum_{j=1}^{N} Z_j exp(i\mathbf{q} \cdot \mathbf{r}_j) \right|^2 \tag{2.60}$$

where the scattered intensity is $I(\mathbf{k}_s)$, and Z_j is the atomic number of the jth atom at position $\mathbf{r}_j$.

The wavevector, $\mathbf{k}_s$, is defined by the x-ray vector, $\mathbf{k}_0$, and the reciprocal lattice vector, $\mathbf{q}$.

$$\mathbf{k}_s = \mathbf{k}_0 + \mathbf{q} \tag{2.61}$$

The XRD pattern is caused by interference of the diffracted x-rays. Constructive interference occurs when the Bragg condition

$$n\lambda = 2d_{hkl} sin\theta \tag{2.62}$$

is met, and the path difference is equal to an integer number, n, of wavelengths. d_{hkl} is the distance between the (hkl) planes and θ is the angle between the incoming x-rays and the surface of the material. Another way of expressing this is using the scattering vector $\mathbf{Q}$

$$\mathbf{Q} = 2\mathbf{k}_0 sin\theta \tag{2.63}$$

where the wavevector of the x-ray is $\mathbf{k}_0$

$$\mathbf{k}_0 = \frac{2\pi}{\lambda} \tag{2.64}$$

XRD can be used on liquids as well as for crystals. Liquids have a mean spacing between atoms, although they do not have a well defined crystal structure, which results in broad diffraction peaks. This makes XRD a useful diagnostic for identifying

the change from a crystalline solid to a liquid (an amorphous glass will however have the same type of diffraction pattern as a liquid). Figure 2.11 shows the evolution of the XRD pattern of Bi during melt, compared with its static liquid diffraction pattern.

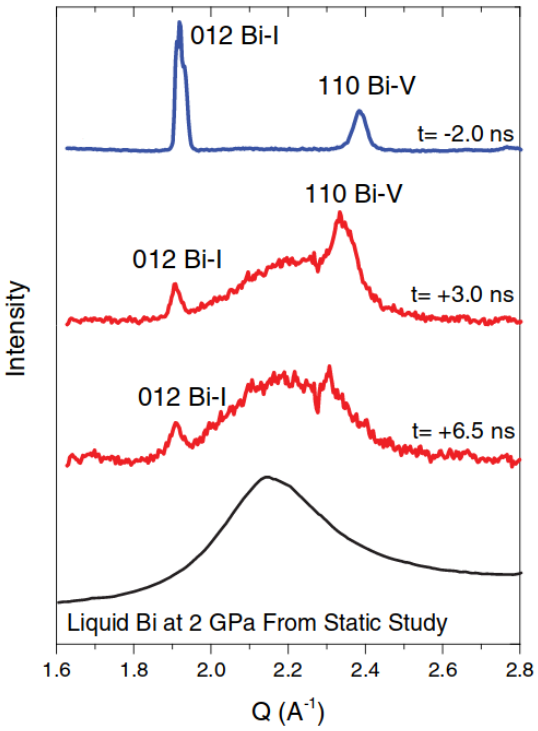

Figure 2.11: XRD patterns for the transition of Bi from a crystal to a liquid [32]. Time relative to the shock is given in ns. Before the shock, the Bi is solid, shown in blue with well defined peaks. Melting on release from the shock is shown in red. For comparison, a static diffraction pattern of liquid Bi is in black. This confirms that the broad peak of the red patterns is liquid. (Reprinted figure from M. G. Gorman, R. Briggs, E. E. McBride, A. Higginbotham, B. Arnold, J. H. Eggert, D. E. Fratanduono, E. Galtier, A. E. Lazicki, H. J. Lee, H. P. Liermann, B. Nagler, A. Rothkirch, R. F. Smith, D. C. Swift, G. W. Collins, J. S. Wark and M. I. McMahon, Physics Review Letters, 115, 1, 2015. Copyright 2015 by the American Physical Society.)

The structure of liquids is defined by the radial distribution function, and it is this that XRD, or simulated XRD, can measure. The radial distribution function, $g(r)$, is the density at distance r from a given particle, divided by the mean density. In figure 2.12, the radial distributions obtained in an MD simulation of Fe [26] contrast typical plots for solids and liquids.

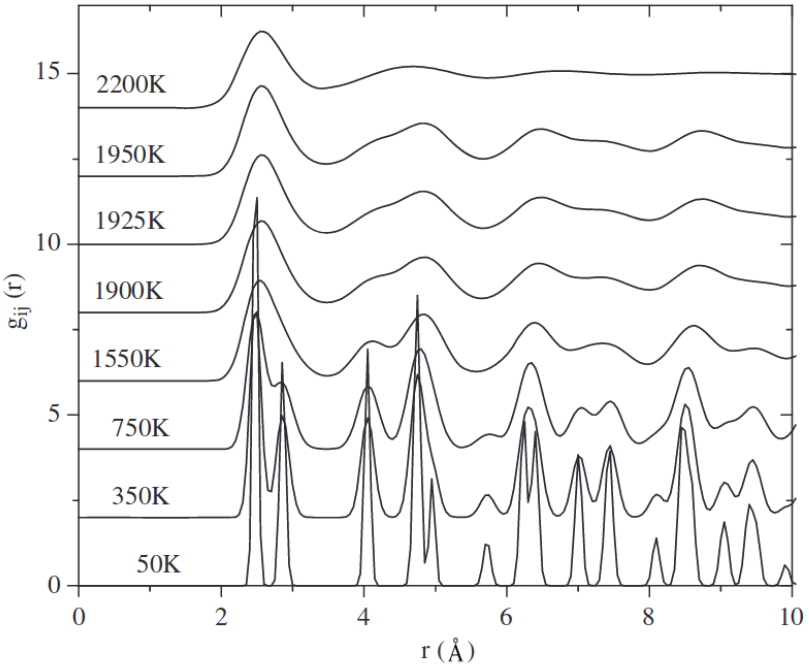

Figure 2.12: The radial distribution of Fe during melting. The sharp BCC crystal peaks with high intensities transform into a smooth liquid distribution with increased temperature [26]. The intensity of the plots is offset with temperature. (Reprinted from Physica B, 407, T. P. Duy and V. V. Hoang, Atomic mechanism of homogeneous melting of BCC Fe at the limit of superheating, 978, Copyright 2012, with permission from Elsevier.)

2.7 Simulating Melting

2.7.1 One Phase Method

As the nucleation energy barrier has to be overcome for a solid to melt, when a block of material is heated too fast for thermodynamic equilibrium to be obtained, it will become superheated before melting, causing an overestimation of the static melting point. Modelling melting using this method is known as the one phase method or the HUM (heat-until-it-melts) method [33], and is quick and simple to perform but does overestimate melt temperature by up to about 20% [25]. This superheating can be reduced by decreasing the heating rate, or avoided by using a different method.

2.7.2 The Hysteresis Method

The hysteresis method utilises the superheating from the one phase method, together with the fact that supercooling also occurs upon solidification. This supercooled melt temperature, T_l, can be combined with the overheated T_s to estimate the melt

temperature T_m. The empirical equation

$$T_m = T_l + T_s - \sqrt{T_l T_s} \tag{2.65}$$

matches experimental results but has no physical meaning [33]. An example of this method is given for Al in figure 2.13.

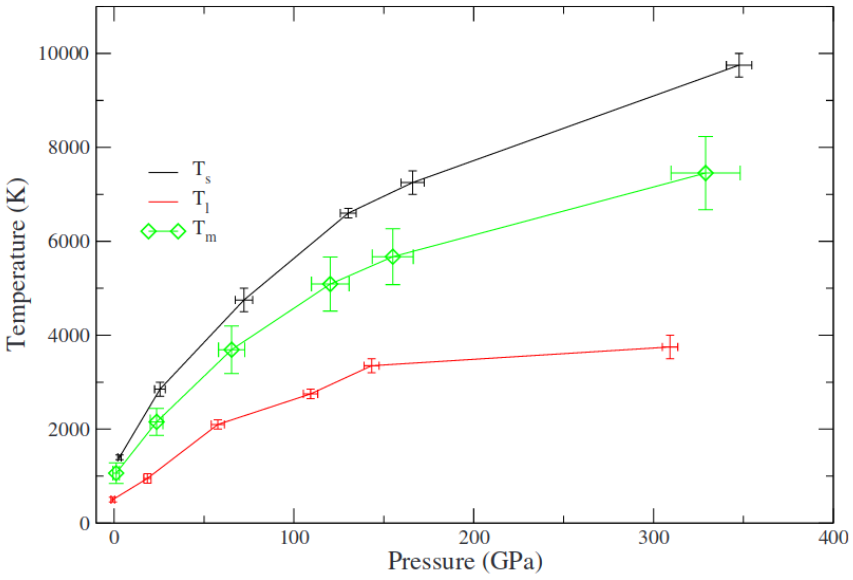

Figure 2.13: Melt temperature T_m (green) for Al obtained from the hysteresis method, compared to the limits of superheating (black) and supercooling (red) T_s and T_l [34]. (Reprinted figure with permission from J. Bouchet, F. Bottin, G. Jomard and G. Zèrah, Physical Review B, 80, 094102, 2009. Copyright 2009 by the American Physical Society.)

The temperature and volume relationship for Cu during melt and solidification is shown in figure 2.14. The jumps in volume correspond to a change in phase, and the hysteresis method calculates the melt temperature to be in between the two temperatures at which these occur [8]. The hysteresis method is used as a computationally cheaper alternative to produce similar results to the coexistence method, despite being based on an empirical equation [35].

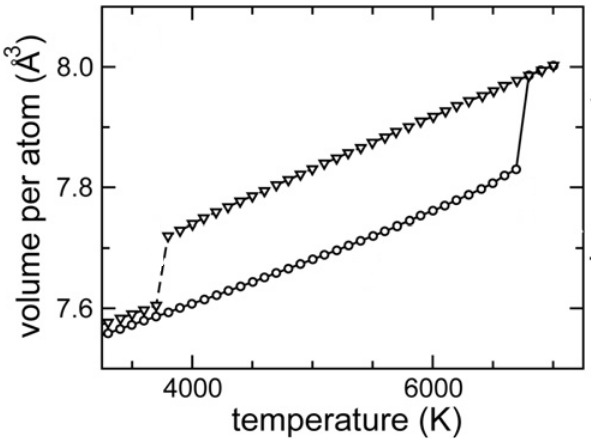

Figure 2.14: A hysteresis loop upon heating (circles) and cooling (triangles) of Cu modelled in MD [8]. The jump in volume per atom indicates a phase change, showing a large difference of over 2000K between melting and solidifying. The hysteresis method can be used to estimate the actual melt temperature in between the two extremes. (Figure from Q. An, S. N. Luo, L. B. Han, L. Zheng and O. Tschauner, Melting of Cu under hydrostatic and shock waveloading to high pressures, Journal of Physics: Condensed Matter, 20, 095220, 2008. IOP Publishing. Reproduced with permission. All rights reserved.)

2.7.3 The Two Phase Method and the Coexistence Method

The two phase method is an established technique for simulating the melting temperature of a material. It provides an interface between the solid and the liquid, which allows one phase to grow without the need to overcome an initial nucleation barrier. The simulation is carried out in the NPT ensemble, and the phase which remains determines whether the pressure-temperature point is above or below the melt curve. This is then repeated iteratively until the melting point is found [36].

A similar approach to the two phase method is the coexistence method, in which a cell containing both solid and liquid is allowed to equilibrate. The main differences are that the coexistence method is carried out in the NVE ensemble, and both phases are present at the end [33]. This is demonstrated in figure 2.15, where both solid and liquid areas can be seen. An equilibrium is reached with one of the phases growing and the other shrinking, but unlike the two phase method, a homogeneous end state is not required.

Both of these methods are intrinsically computationally expensive as they require large simulation cells and long simulations [35]. As a result of this, although these methods have been used since the 1970s, it is only more recently that they have been able to produce accurate results [38].

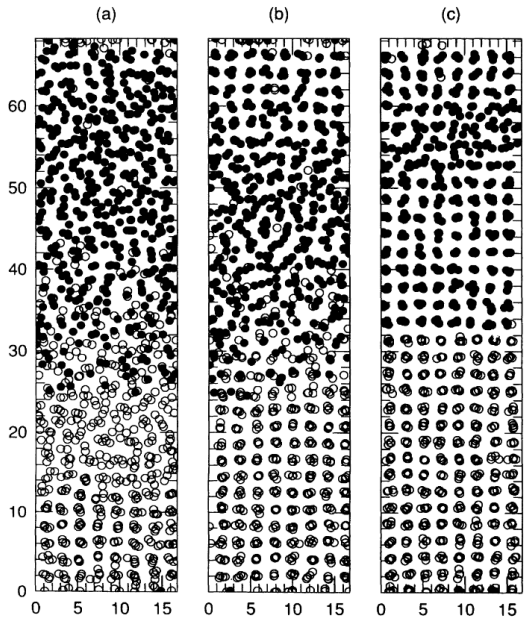

Figure 2.15: Possible end configurations of the coexistence method [37]. The liquid, disordered, can be distinguished from the ordered solid crystal, with an intermediate region between the two. (Reprinted figure with permission from J. R. Morris, C. Z. Wang, K. M. Ho and C. T. Chan, Physical Review B, 49, 3109, 1994. Copyright 1994 by the American Physical Society.)

2.7.4 The Z Method

An alternative method of simulating melt is the Z method. This begins with one phase and makes use of the superheating phenomenon to reduce the computing requirements.

Melting causes a drop in temperature of the system due to the latent heat, which acts as a sink of energy for the first order phase transition. This reduction in temperature, combined with the increase in temperature from external heating, results in the characteristic Z shaped isochores which give the method its name [34]. The pressure and temperature of the liquid immediately after melt is taken to be the melting point [33]. This method has been found to produce similar results to the two phase and coexistence methods, although results deteriorate with fewer atoms and shorter runs [33]. An example of the z-profiles is given in figure 2.16, which shows that the trough of the z-profile overshoots the melt curve with a small box size, but agrees with the coexistence method well as the box size is increased [33].

The solid is simulated in the NVE ensemble at a temperature above the estimated melting temperature. If the simulation is sufficiently long, and the temperature is above the limit of superheating, T_{LS}, the solid should melt spontaneously and the temperature will drop to T_m [34]. This drop is shown by the sharp decrease in

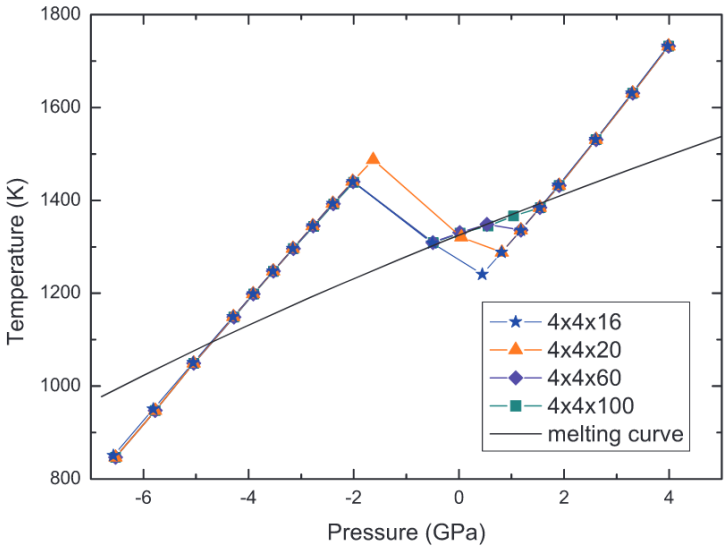

Figure 2.16: Comparison of isochoric curves, with box size given in the legend in number of unit cells. The melt curve was obtained using the coexistence method [39]. (Reprinted from S. Wang, G. Zhang, H. Liu and H. Song. Modified Z method to calculate melting curve by molecular dynamics. The Journal of Chemical Physics, 138(13):134101, 2013, with the permission of AIP Publishing.)

temperature in the z-profile. It can be repeated at decreasing temperatures to find T_{LS}, the lowest temperature at which melting should occur spontaneously.

MD simulations of Fe found T_{LS} to have a dependence on T_m which was constant with pressure [40]

$$\frac{T_{LS}}{T_m} - 1 = \frac{ln2}{3} \tag{2.66}$$

The time before melt occurs is the waiting time τ_w. This is shown in figure 2.17 for four simulations under the same initial conditions. The difference in pressure and temperature remain constant but the waiting time varies. One limitation of this method is that it can be difficult to estimate the wait time required to be sure the lower liquid temperature has been found [34]. The probability distribution of the waiting time is roughly exponential, and the mean value of τ_w depends strongly on how much higher the temperature of the solid is than T_{LS} [41].

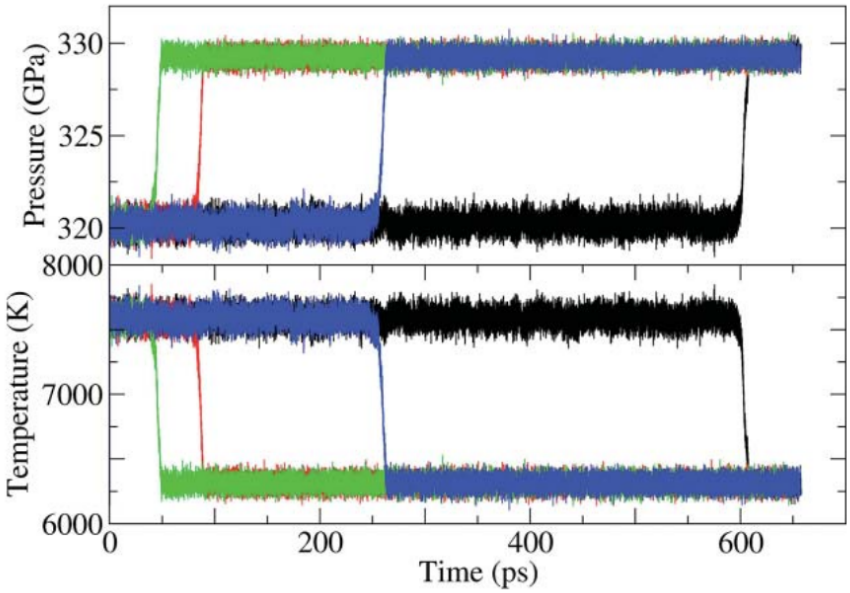

Figure 2.17: Four independent simulations, with the same initial pressure and temperature, demonstrating the range of waiting times before melting [41]. (Reprinted from D. Alfè, C. Cazorla and M. J. Gillan. The kinetics of homogeneous melting beyond the limit of superheating. The Journal of Chemical Physics, 135(2):024102, 2011, with the permission of AIP Publishing.)

2.8 Melting Rate

There are two contributing factors to the growth of melt: the increase in the number of nucleation sites and the growth of existing nucleation sites.

One expression for the nucleation rate is equation 2.67, where n_{hom} is the rate of formation of homogeneous nucleation sites [42]

$$n_{hom} = n_0 exp\left(\frac{-\Delta G^*(T)}{kT}\right) exp\left(\frac{-Q}{kT}\right) \tag{2.67}$$

This equation is made up of the driving force term

$$exp\left(\frac{-\Delta G^*(T)}{kT}\right) \tag{2.68}$$

where ΔG^* is the energy barrier to nucleation, and the diffusivity term

$$exp\left(\frac{-Q}{kT}\right) \tag{2.69}$$

where Q is the activation energy of diffusion [27].

For a superheated crystal, the increasing temperature will have an exponential effect

on both of these terms, rapidly increasing the nucleation rate [27].

The pre-exponential factor can be approximated as

$$n_0 \sim \frac{nkT}{h} \tag{2.70}$$

where n is the number density of atoms, k is Boltzmann's constant, and h is Planck's constant.

An equation for growth rate, u, is given in equation 2.71

$$u = u_0 exp\left(\frac{-Q}{kT}\right)\left(1 - exp\left(\frac{\Delta G_V}{kT}\right)\right) \tag{2.71}$$

where ΔG_V is the free energy difference between the initial and final state [42]. This can also be expressed in terms of the difference in enthalpy before and after melting, ΔH_m, in the form [43]

$$u = u_0 exp\left(\frac{-Q}{kT}\right)\left(1 - exp\left(\frac{\Delta H_m}{kT}\frac{(T - T_m)}{T_m}\right)\right) \tag{2.72}$$

which can be simplified as

$$u = u_0' exp\left(\frac{-Q}{kT}\right)\left(\frac{T - T_m}{T_m}\right) \tag{2.73}$$

where u_0 and u_0' are constants.

2.9 Crossing Phase Transitions

2.9.1 Shock Driven

As seen in phase diagrams such as figure 2.4, a method of reaching the melting point, both experimentally and in simulations, is to pass a shock through the solid material. The melting temperature, T_M, can be obtained from shock temperature, T_H, in a solid-liquid mixed phase zone because

$$T_H = T_M \tag{2.74}$$

for partial melting on the Hugoniot [44], although temperature cannot be measured directly from XRD, and must be inferred from the strain. This can give the melting point on the Hugoniot, but using the release after a shock allows more of the phase diagram to be explored.

2.9.2 On Release

An experiment at the Linac Coherent Light Source (LCLS) in 2015, compressing bismuth to 10 GPa, demonstrated how liquid XRD could be used to find the melt curve at pressures achieved by shock compression [32]. The path of decompression after the shock wave can be seen in figure 2.18. The shock takes the material to a point on the Hugoniot. Temperature and pressure then decay quasi-isentropically until the melt curve is reached. At this point, the latent heat of melting acts as a sink of energy, causing the path to travel along the melt curve instead of the release isentrope (line of constant entropy). Once all of the sample has melted, the path continues along an isentrope, on the liquid side of the melt curve. A free electron laser was used as the X-ray source and the phase change was observed using XRD, as shown earlier in figure 2.11.

A more recent study (McGonegle 2019 [45]) suggests that the release in a solid is not completely isentropic, due to plastic effects in the material. The release temperatures in MD simulations for Ta were found to be higher than would be expected for isentropic release, and this was corroborated by experimental results.

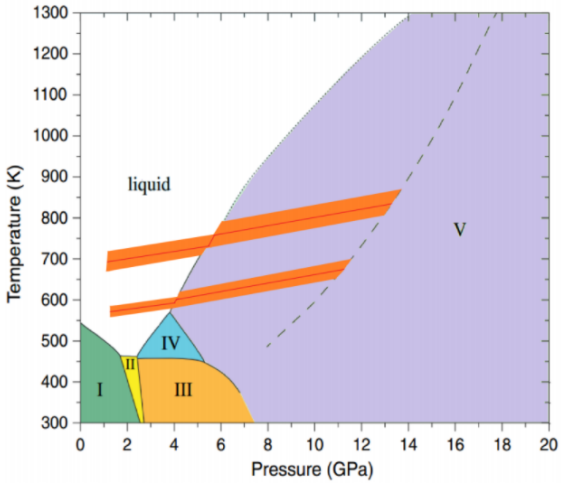

Figure 2.18: Phase diagram showing the release isentropes (red, with orange error estimate) for Bi. The dashed line shows the Hugoniot, and the dotted line is the melt curve [32]. (Reprinted figure from M. G. Gorman, R. Briggs, E. E. McBride, A. Higginbotham, B. Arnold, J. H. Eggert, D. E. Fratanduono, E. Galtier, A. E. Lazicki, H. J. Lee, H. P. Liermann, B. Nagler, A. Rothkirch, R. F. Smith, D. C. Swift, G. W. Collins, J. S. Wark and M. I. McMahon, Physics Review Letters, 115, 1, 2015. Copyright 2015 by the American Physical Society.)

2.10 Mirror image method

After a shock, release waves propagate inwards in the target from free surfaces, causing a decrease in pressure. Release waves, unlike shock waves, do not have a

pressure discontinuity, due to the dependence of wave speed on pressure described in section 2.3. The change in pressure is therefore adiabatic and nearly reversible, so release paths are approximately isentropic [46]. This approximation, which is required by the mirror image method, is valid unless shock melting occurs.

The Hugoniot can be defined using the relationship between pressure and particle velocity, P_H and u_H.

$$P_H = \rho_0 U_s u_H \tag{2.75}$$

where ρ_0 is the initial density of the material. As shock velocity, U_s, is linear with particle velocity for most metals, this can be expressed as

$$P_H = \rho_0 u_H (c_0 + S u_H) \tag{2.76}$$

where c_0 and S are constants.

It has been shown experimentally, on release after a shock, that

$$2u_H \approx u_{FS} \tag{2.77}$$

where u_{FS} is the velocity of the rarefaction wave from a free surface. This is expanded upon to include other release velocities, when the shock wave reaches a boundary with a different material, in the mirror image method [47]. The curve showing possible release states is found to be a mirror of the Hugoniot, reflected at the particle velocity of the shock [48].

This is shown in figure 2.19. The Hugoniot is reflected for several given particle velocities, and these mirror images show the possible new velocities and pressures of either a release rarefaction wave, or a reflected shock wave (if the new material is of greater impedance), when the shock wave reaches a material boundary.

The free surface velocity, u_r, is given by the equation

$$u_{FS} = u_H + u_r \tag{2.78}$$

and so the approximation in equation 2.77 can be written as

$$\frac{u_r}{u_H} \approx 1 \tag{2.79}$$

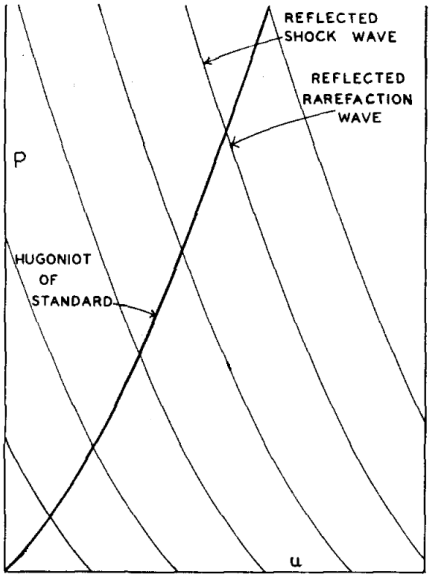

Figure 2.19: The Hugoniot of a material can be shown as pressure, P, against particle velocity, u. For any given particle velocity, the mirror image of the Hugoniot at that point shows the pressure-velocity states that can be found either on release as a rarefaction wave, or as a further shock wave if there is a boundary with a material of higher shock impedance [47]. (Reprinted from J. W. Enig. A complete E, P, V, T, S thermodynamic description of metals based on the P-u mirror image approximation. Journal of Applied Physics, 34(4):746, 1963, with the permission of AIP Publishing.)

This is shown to be the case for metals [47], using the Hugoniot relationship and equation 2.80 for adiabatic release

$$u_r = -\int_0^{P_1} \left(\left(-\frac{dV}{dP} \right)^{1/2} dP \right)_{adiabatic} \tag{2.80}$$

From an initial state (P_0, V_0) shocked to (P_1, V_1), and then released to (P_0', V_0'), the total energy change is given by

$$E' - E_0 = \beta(V_0' - V_0) = \frac{1}{2}(P_1 - P_0)(V_0 - V_1) - \int_{V_1}^{V_0'} (PdV)_{adiabatic} \tag{2.81}$$

where

$$\beta = \frac{C_p}{\alpha V_0} \tag{2.82}$$

C_p is the specific heat capacity and α is the thermal coefficient of volume expansion. Making the substitutions

$$V_0' = V_1 - \int_0^{P_1} \left(\left(\frac{dV}{dP} \right) dP \right)_{adiabatic} \tag{2.83}$$

and

$$\int_{V_1}^{V_0'} (PdV)_{adiabatic} = \int_0^{P_1} (VdP)_{adiabatic} - P_1V_1 \tag{2.84}$$

gives

$$\int_0^{P_1} \left(\left(V - \beta \frac{dV}{dP} \right) dP \right)_{adiabatic} = \frac{P_1(V_0 + V_1)}{2} + \beta(V_0 - V_1) \tag{2.85}$$

Integrating this produces the P-V hyperbola

$$(P + \beta)(V - V_1) + \frac{(P - P_1)(V_0 - V_1)(\beta + \frac{1}{2}P_1)}{(P_1 + \beta) ln \left(\frac{P_1 + \beta}{\beta} \right)} = 0 \tag{2.86}$$

From this, the accuracy of the mirror image approximation can be found [47].

$$\left(\frac{u_r}{u_H} \right)_{max} = \left(\frac{P_1 + 2\beta}{2P_1} ln \frac{P_1 + \beta}{\beta} \right)^{1/2} \tag{2.87}$$

This difference between equations 2.79 and 2.87 is shown in figure 2.20 to be less than 1% for three metals over a pressure range of 10-50 GPa, so the mirror image approximation is valid [49]. This analysis was modified to include a phase change on release, by incorporating an additional term to account for the change in volume between phases, and, in the tested cases of Sn and Pb, the deviation from the mirror image approximation was shown to still be negligible [50].

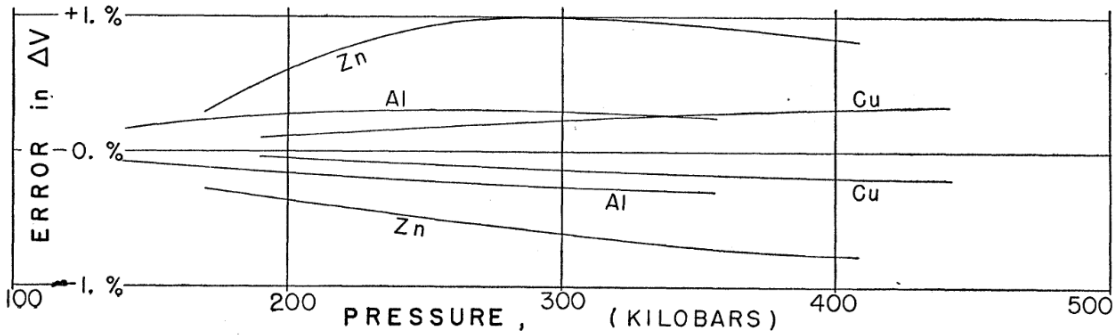

Figure 2.20: The deviation in volume of the mirror image method from the actual volume on release, found using equation 2.87, is shown to be less than 1% for three different metals [49]. (Reprinted figure from J. M. Walsh and R. H. Christian, Physical Review, 97, 1544, 1955. Copyright 1955 by the American Physical Society.)

Cu is the principal test material used for this thesis, and the mirror image approximation was shown to agree with experimental data for Cu in figure 2.21 [51].

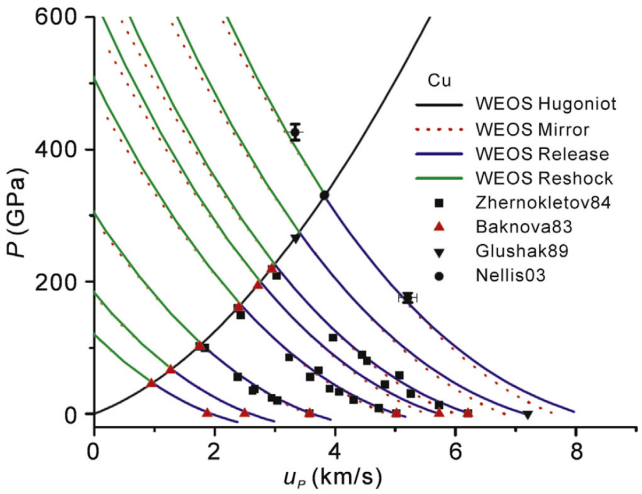

Figure 2.21: A modelled Hugoniot for Cu, using the Wide Regime Equation of State (WEOS) [51]. The mirror images found at various particle velocities match experimental release pressures, shown as data points. (H. Liu, H. Song, Q. Zhang, G. Zhang and Y. Zhao, Matter and Radiation at Extremes, 1, 123, (2016); licensed under a Creative Commons Attribution (CC BY) license.)

2.11 Impedance

Acoustic impedance, $Z_{acoustic}$, is defined as

$$Z_{acoustic} = \rho c_s \tag{2.88}$$

where c_s is the speed of sound in a material and ρ is density.

Similarly, shock impedance, Z, is determined by the shock velocity, U_s, and density

$$Z = \rho U_s \tag{2.89}$$

Shock impedance is the ratio of pressure to volume flow. It is analogous to electrical impedance, the ratio of potential difference to current.

At a boundary between materials with different shock impedances Z_1 and Z_2, the coefficients of pressure reflection and transmission, R_p and T_p, give the reflected and transmitted pressure relative to the incident pressure (P_r, P_t and P_i) defined as

$$R_p = \frac{P_r}{P_i} = \frac{Z_2 - Z_1}{Z_2 + Z_1} \tag{2.90}$$

$$T_p = \frac{P_t}{P_i} = \frac{2Z_2}{Z_2 + Z_1} \tag{2.91}$$

The coefficient of power reflection, R_w, is given by

$$R_w = \frac{P_r^2/Z_1}{P_i^2/Z_1} = R_p^2 \tag{2.92}$$

Equations 2.90 and 2.91 can also be derived by considering the wave equations, which must be continuous across the barrier of the two materials [52]. A general solution to the wave equation

$$\frac{\partial^2 u}{\partial t^2} - c^2 \frac{\partial^2 u}{\partial h^2} = 0 \tag{2.93}$$

is

$$u(h,t) = f(h - ct) + g(h + ct) \tag{2.94}$$

where u is the wave function and h is the displacement, with functions f and g. A similar equation applies to stress, σ,

$$\frac{1}{\rho c}\sigma(h,t) = f(h - ct) + g(h + ct) \tag{2.95}$$

The continuity at the boundary where $h = 0$, for the initial ($f(-c_1t)$), reflected ($g(c_1t)$) and transmitted ($k(-c_2t)$) waves can be expressed as

$$f(-c_1t) + g(c_1t) = k(-c_2t) \tag{2.96}$$

and for stress

$$Z_2 f(-c_1t) - Z_2 g(c_1t) = Z_1 k(-c_2t) \tag{2.97}$$

From this it can be shown that

$$\frac{g(c_1t)}{f(-c_1t)} = \frac{Z_2 - Z_1}{Z_1 + Z_2} \tag{2.98}$$

and

$$\frac{k(c_1t)}{f(-c_1t)} = \frac{2Z_2}{Z_1 + Z_2} \tag{2.99}$$

which is in agreement with the definitions of R_p and T_p

The dependence of equations 2.90 and 2.91 on Z_2/Z_1 are shown in figure 2.22. At the limit where $Z_2/Z_1 = 0$, $R_p = -1$ and $T_p = 0$ so all the pressure is reflected. When $Z_2/Z_1 \to \infty$, $T_p \to 2$ and $R_p \to 1$ and all of the pressure wave is transmitted.

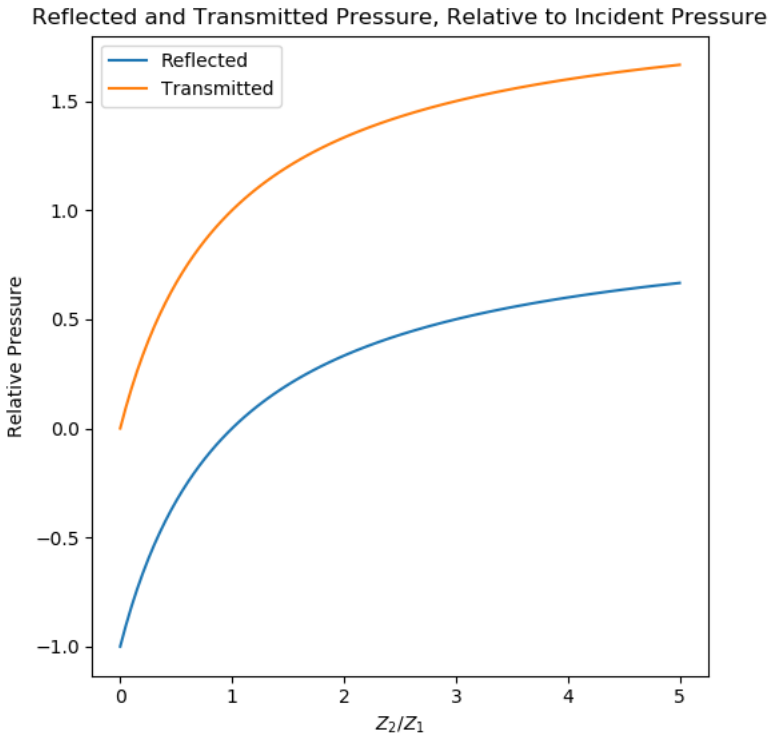

Figure 2.22: The effect of the difference in impedance Z_2/Z_1 on the reflected pressure, R_p, and transmitted pressure, T_p. At $Z_1 = Z_2$, $T_p = 1$ and $R_p = 0$ as this is equivalent to no boundary.

2.11.1 Tampers

A standard shock target design is ablator/target/tamper. The ablator layer interacts with the laser, as described in section 2.2.2, and it ablates due to the energy dump. A shock wave then propagates through the target due to conservation of momentum. Experiments can also be carried out with the target material being ablated directly. However, using a separate ablator creates a smoother shock wave and the choice of material can improve laser coupling.

The target is the material which is being studied under pressure; it is initially compressed by the ablator, then release or further compression is caused by the tamper.

Tampers such as LiF [44], PMMA [5] and Be [53] are used to prevent free surface expansion into a vacuum when the shock wave reaches the back of the target. Instead, a release wave (or a shock wave, if the tamper's shock impedance is greater than that of the target material) is reflected back through the target, and a transmitted wave continues forward through the tamper. The tamper's purpose may also be structural, as it can support a thin layer of target material or allow a more complex

target design to be deposited onto it.

Using a tamper causes new difficulties in modelling the target, as it would increase the size of the simulation box, and a potential for the tamper material, as well as an interaction potential for the target and tamper materials, would be required. The tamper is therefore sometimes neglected from simulations, which causes a difference between experimental and simulated results [54].

Chapter 3

Developing a numerical melt model to obtain static melt curves from dynamic simulations

In this chapter, a novel method for finding the melt temperature of simple metals using molecular dynamics (MD) simulations is described, referred to in this thesis as the numerical melt method. It uses dynamic results to calculate a static melt temperature. This bridges the gap between dynamic laser shock compression experiments and the static values relevant to materials and planetary sciences at high pressures. The coexistence method is the established static technique for finding the melting point using molecular dynamics, and the proposed method was able to reproduce results obtained from the coexistence method, with the computational cost reduced by two orders of magnitude. Using Cu and Ta as test elements, static melt curves have been found accurately for the pressure range 0 to 10 GPa.

3.1 Introduction

This new method for finding melting points in MD uses a numerical model to determine the static melt temperature. It has reduced computing times compared with the coexistence method, and the ability to find the static melt temperature from dynamic measurements leads to potential applications in dynamic high powered laser experiments.

Establishing the melt temperature in MD is non trivial, due to the kinetic barrier for melting leading to overshoot of the melting point, which is explained in Chapter 2. The two phase and coexistence methods are standard ways of determining the melt temperature in MD, and are based on static rather than dynamic simulations. In the coexistence method, solid and liquid regions are both present in order to avoid the kinetic barrier. However the computational cost is high because multiple simulations

are needed to iteratively determine the melt temperature, using large box sizes and long simulation times. One phase models, which have lower computational costs, are the z-method and the hysteresis method. The hysteresis method produces melt temperatures which agree with other methods, but has no physical basis. The theory behind all of these is discussed in Chapter 2.

Rapidly heating a material until it melts forms a z-profile when plotting temperature against pressure or time. The latent heat acts as a sink, as energy is used to carry out a first order phase transition. In a static environment, the temperature would remain constant until all the liquid has melted, but this is not the case in dynamic situations, such as laser shock compression, where the heating rate is too high for an equilibrium to be established. The aim of this thesis is therefore to model dynamic melt, and from that infer the static melt temperature, since high pressure experimental methods are dynamic but their physical applications are static.

In this chapter, MD simulations were used to study the z-profile at different heating rates and pressures. Further modelling was carried out on these simulations in order to extract the static melt temperature, latent heat and specific heat capacity, and to measure the growth rate of melt.

Cu and Ta were modelled, to check the method on both a face centered cubic (FCC) and a body centered cubic (BCC) simple metal. Each has an established MD potential. Previous work defining the Cu melt curve up to 300 GPa is shown in figure 3.1 [55], with Ta up to 500 GPa [56].

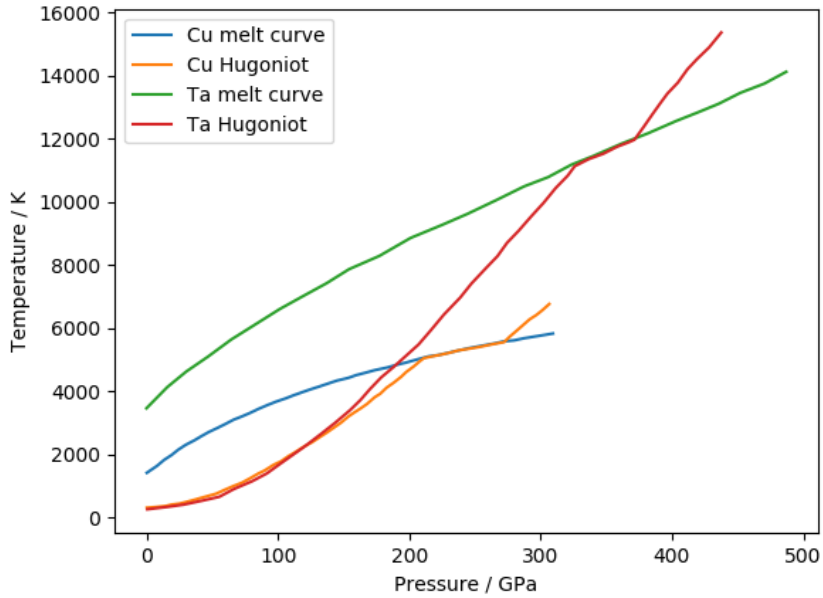

Figure 3.1: Literature melt curve and Hugoniot for Cu [57] (from DAC experiments) and Ta [56] (from simulations).

3.2 Method

3.2.1 Overview

Simulations were carried out using the MD code LAMMPS [58]. A block of Cu or Ta was heated at different rates, and the global temperature was recorded. The onset of melt could be seen in the mean square displacement (MSD) and the centrosymmetry parameter (CSP), as well as from the drop in temperature due to the latent heat. The temperature profile forms a z-shape and the melting process was fitted to this using a numerical melt model in order to obtain the melt temperature and kinetic variables. The coexistence method and the hysteresis method were also carried out so that the results could be compared.

3.2.2 LAMMPS simulations

LAMMPS was used to create a cube of atoms. The atom style was atomic, which is appropriate for metals [58]. The cube had periodic boundaries and an FCC or a BCC lattice, for Cu and Ta respectively. For both elements, an Embedded Atom Model (EAM) was applied (the Sheng EAM potential) [59, 60].

During the simulations, the following values were obtained: temperature, pressure, MSD, and CSP. The MSD output from LAMMPS has separate x, y and z values, averaged for all atoms. However, only the total was required as the simulation is

isotropic. The CSP gives an output for each atom, which shows the deviation from a perfect lattice. MSD and CSP are both methods of describing which phase the atoms are occupying, and are discussed in subsection 3.2.4

The units system used was metal, with a time step of 0.001 ps. The data for individual atoms was stored in a dump file and global variables were printed to a text file. The z-profile analysis can be carried out with just the global values of temperature, pressure and MSD, so only the text file is necessary, which reduces run time and the amount of data storage needed. Thermodynamic variables were computed and printed every 100 timesteps, as outputting more frequently increases run time and is unnecessary. Dump files were initially used to image the system in the visualisation software OVITO (Open Visualisation Tool) [61] at different times throughout the simulations. While this was an important step to check that the simulation was running as expected, the CSP and temperature show the onset of melt clearly, so the imaging is not a necessary part of the z-profile analysis, and removing it further increased the efficiency of this method.

The setup was run at 300K for 1000 timesteps of 0.001 ps, in order for the system to equilibrate. The velocity was assigned at 600K, as half of the energy is converted into potential energy due to equipartition. A velocity seed value was also given. Simulations could be run with different velocity seeds to find error bars for the data; using a different seed changed the initial atom velocity distribution, which allowed simulations to be repeated with the same conditions in order to check the accuracy of the results. When working on parallel processors, the velocity assigned to a particular atom is independent of the number of processors, and so there will be consistency between runs, if the same velocity seed is used.

An NVE (microcanonical) ensemble was used and the pressure was fixed with an isotropic Berendsen barostat. The simulation box was set to the desired pressure, with a damping parameter of 1000 bars. This arrangement was chosen so that the pressure of each simulation could be determined in order to locate points on the melt curve to investigate.

After the system had equilibrated, the temperature was increased by the fix heat command. The heat was added every 10 timesteps and the energy flux parameter was varied to find the temperature profiles at different heating rates. The run time was dependent on heating rate, and each simulation was taken well into the liquid phase. The Ta simulations had a longer run time due to the higher melting point.

3.2.3 Box size

As expected, increasing the number of unit cells in the LAMMPS simulations did not alter the temperature of the peak and the trough, but it did affect the amount of thermal noise and the steepness of the profile. This difference can be seen for Cu with 5x5x5 unit cells and 10x10x10 unit cells in figure 3.2. However, using a box size of 20x20x20 makes little further difference, suggesting that a greater increase is not necessary.

An advantage of the numerical melt method is the reduced computational cost, and the 10x10x10 box used for Cu in the chapter (with 20x20x20 sometimes used additionally, to check that the results from the two box sizes always matched) is small compared with the requirements for the coexistence method. Ta needed a larger box to maintain the same number of atoms, due to the difference between an FCC and BCC conventional unit cell.

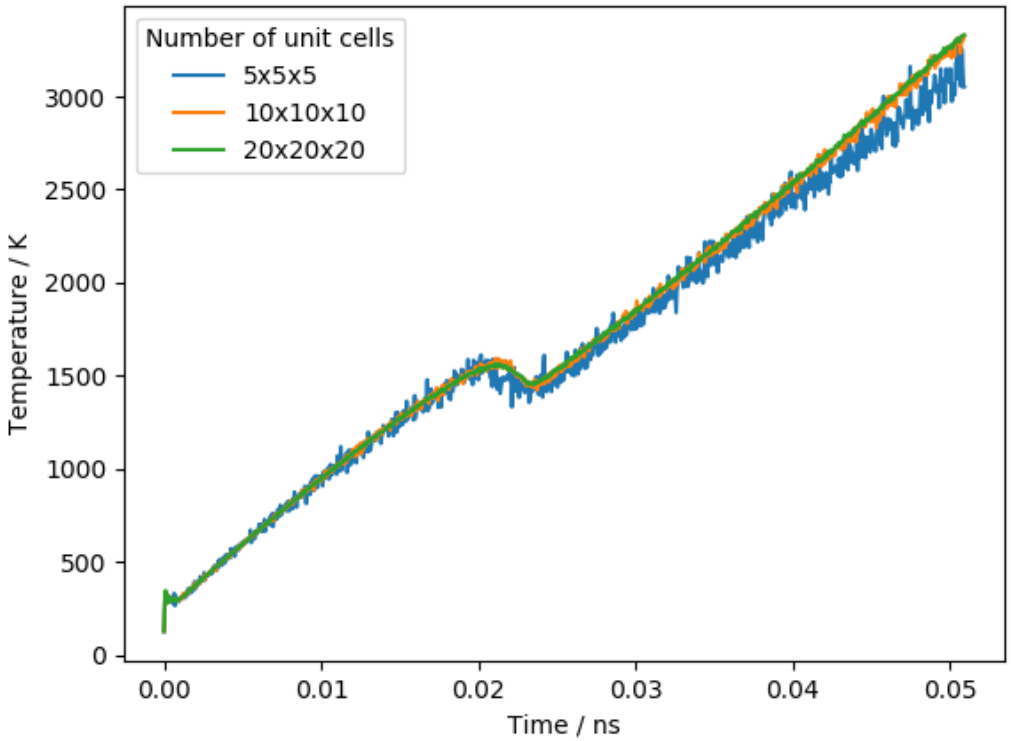

Figure 3.2: Change in z-profile with box size for Cu for a heating rate of 70 K/ps and a lattice parameter of 3.63 Å. The 10x10x10 and 20x20x20 unit cell profiles overlap, with the 10x10x10 showing more noise. The 5x5x5 profile has much more noise and a different shape during melt and at high temperatures.

3.2.4 Defining melt

The centrosymmetry parameter (CSP) can be used to determine the onset of melt. A perfect FCC or BCC crystal will have a CSP of 0, and this increases with disorder. An example of the progression of the CSP during a simulation is shown in figure 3.3. For the mean CSP (in blue) there are three distinct regions. The slow increases are due to heating within the same phase and the sharp increase represents the phase transition.

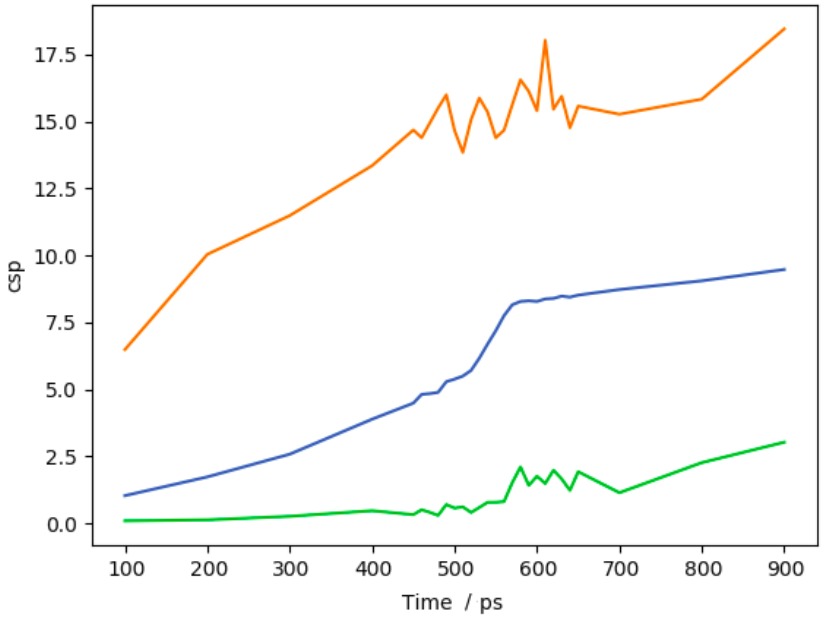

Figure 3.3: The progression of centrosymmetry parameter (CSP) during melting of Cu. CSP is given per atom. The blue line shows the mean CSP, orange and green are the maximum and minimum values.

As shown in figure 3.4, the highest CSP values for each atom occur when that atom is already in a liquid environment, and are not caused by the disorder at a melt boundary. The broad, roughly Gaussian distribution with the peak at a CSP of 9-10 is indicative of the liquid phase, and the sharper peak at lower CSP is from the solid phase. During melting, the distribution would be a combination of those of the two profiles.

CSP was used to define the growth of liquid in all simulations. MSD (Mean Square Displacement) was found to show a similar effect; however, the distributions of solid and liquid MSD had more overlap than those of CSP. In both cases, the mean value was used to determine melting. The standard deviation could also have given the melt temperature, as the distribution of CSP and MSD is widest when two phases

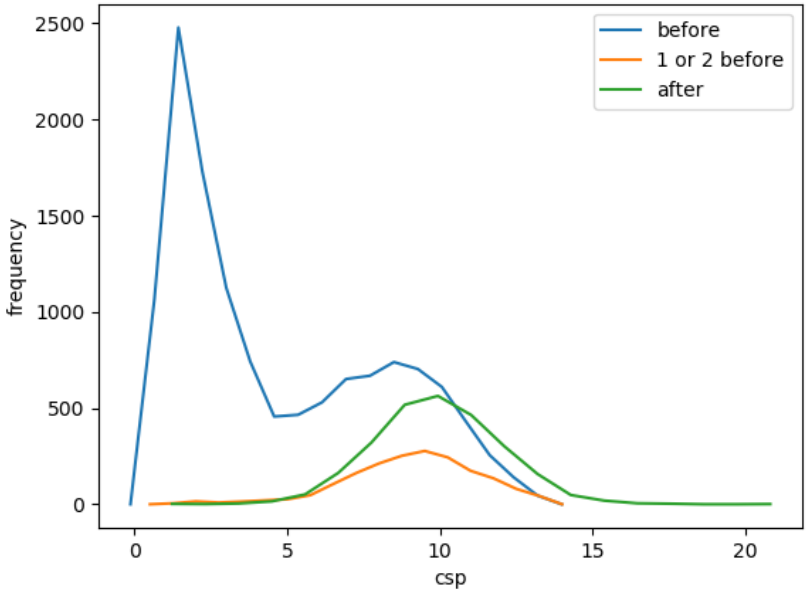

Figure 3.4: Frequency distributions showing the CSP in the timesteps before and after the highest occurring CSP of each atom. Before the highest CSP, the typical histogram profile of solid and liquid can be seen but for just before (defined as 1 or 2 timesteps) and afterwards the profile has a liquid like shape.

are present. Alternatives such as the specific heat capacity, shown for solid and liquid Cu in figure 3.6, could have been chosen to determine the proportion of liquid.

3.2.5 The numerical melt model

A numerical method was developed to model the melting process, and this was then fitted to the LAMMPS data in order to find a more accurate value of the static melt temperature than can be obtained from the trough positions. The amount of liquid produced at each time step, by both nucleation and growth of existing nuclei, was calculated. This caused a reduction in temperature, due to the latent heat, and from this a z-profile was formed.

The numerical melt method process is outlined in figure 3.5. The temperature started at 300K and was increased at each time step according to the heating rate of the LAMMPS simulation. Heat capacity of a solid is temperature dependent, so the amount the temperature was increased by changed each time step (with the rate of input energy constant). Once the melt temperature was reached, melting could begin. The liquid growth rate and nucleation rate were calculated in each step.

The radius of each nucleus was stored so the growth rate could be used to calculate the new volume of every site at each time step. When formed, each nucleus was given

a radius corresponding to the growth rate at that time. This is an approximation, as the nucleation rate is actually determined by the probability of a nucleus with the critical radius being formed.

Once a significant amount of liquid is present, the liquid regions will be prohibited from growing in an ideal sphere, reducing the efficiency of the growth. To account for this, if the predicted amount of growth for a time step was larger than the amount of solid present, the volume added to each nucleus per time step was multiplied by the fraction of solid remaining, in order to slow down melting towards the end, and better fit the LAMMPS profiles.

From this new volume of liquid, the temperature lost due to latent heat was obtained and deducted from the current value. This process was repeated for each time step until no solid remained. After that, the rise in temperature was solely determined by the liquid heat capacity (which is not temperature dependent).

The curve_fit function of the SciPy Python module was used to find the optimum value of the melt temperature, T_m, and the values n_0 and u_0, the nucleation and growth rate parameters defined in section 3.2.7. From this optimised value, the error in T_m was estimated by how much these fitted parameters could be altered with the model remaining, by eye, a good fit to the LAMMPS data.

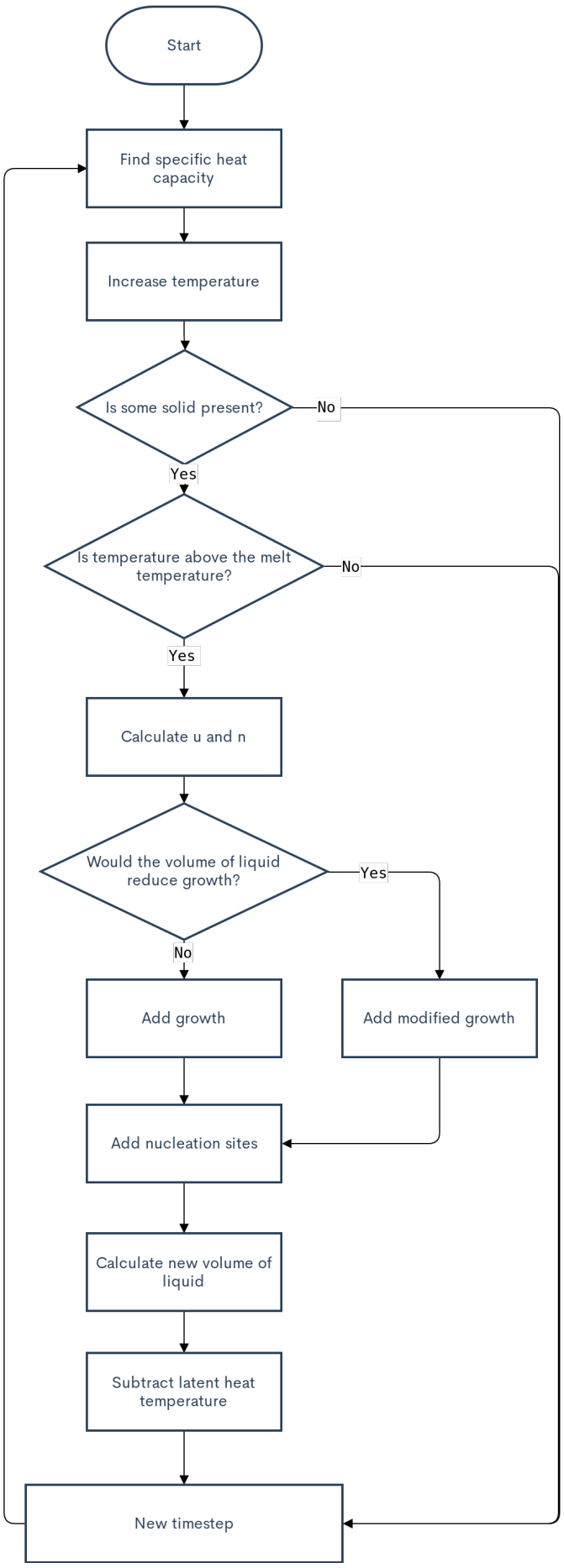

Figure 3.5: Flow chart showing the main stages of the numerical method for modelling the z-profile. For each time step, the temperature is calculated and used as the input for the next time step. The growth and nucleation rates are u and n respectively.

3.2.6 Specific heat capacity

Specific heat capacity of a solid is linear [62] (or approximately linear [63]) with temperature. A graph of this is shown in figure 3.6. Upon melting, there is a jump to the liquid specific heat capacity, which remains constant with temperature.

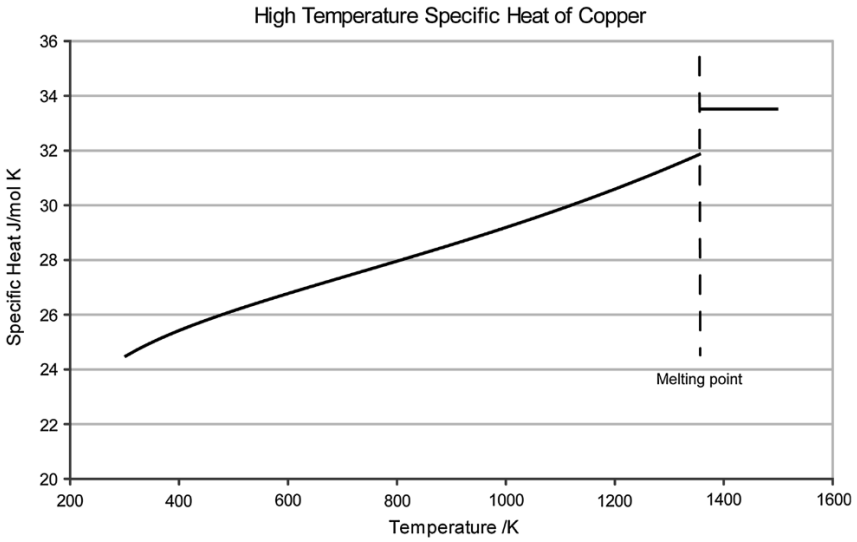

Figure 3.6: The specific heat capacity of solid Cu increases approximately linearly with temperature until reaching the melting point [63]. The heat capacity of the liquid Cu is not temperature dependent. (Reprinted with permission.)

The gradient of the temperature profile, with a constant heating rate, therefore decreases as it approaches the melting temperature, as the specific heat capacity of the solid increases. Assuming a linear fit to be a good approximation for the temperature dependence of specific heat capacity, C_p, the equation

$$C_P(T, T') = c_0 + f(T')\frac{T}{T_{m0}} \tag{3.1}$$

was fitted to the temperature profile for Cu before any melting begins, at different heating rates, T'. T_{m0} is the literature static melt temperature, and c_0 and f were found through fitting. c_0 was constant at 0.38 J/gK, and f was rate dependent, as shown in figure 3.7.

It can be seen in figure 3.7 that the temperature dependence of specific heat capacity is greater at lower heating rates, where f changes the most rapidly. This may be due to the response time either in the numerical model, as the value of temperature in the previous time step is used with f to find the temperature gained in the current step, or in the material, as the non equilibrium conditions mean that heat is being added faster than the material can thermally respond.

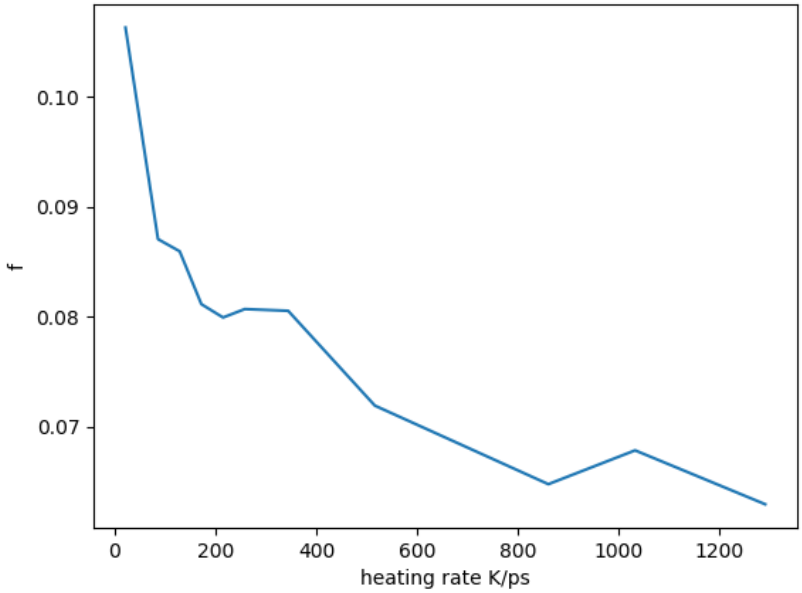

Figure 3.7: Graph showing the how the value of f, used in equation 3.1, varies with heating rate. The specific heat capacity therefore has a greater temperature dependence at lower heating rates.

In order to correct for this, the heat capacity was found using the low temperature region of the temperature profile, before applying the numerical method. However, due to the correlation with heating rate, this is could be predicted for some of the rates without needing to be found for each. A larger range of the temperature profile would give a more precise fit, but as a linear fit for specific heat capacity is sufficient, this should be carried out at low temperatures where it is certain that no melt is occurring. CSP or MSD can be used to check that melting has not begun, and starting the simulations at 300K, rather than closer to the melting point, gives a sufficient temperature range.

The specific heat capacity for Ta had a similar linear fit with temperature, and the same method was applied to it. The dependence on f with heating rate was comparable to Cu, and the pressure dependence is shown in figure 3.8.

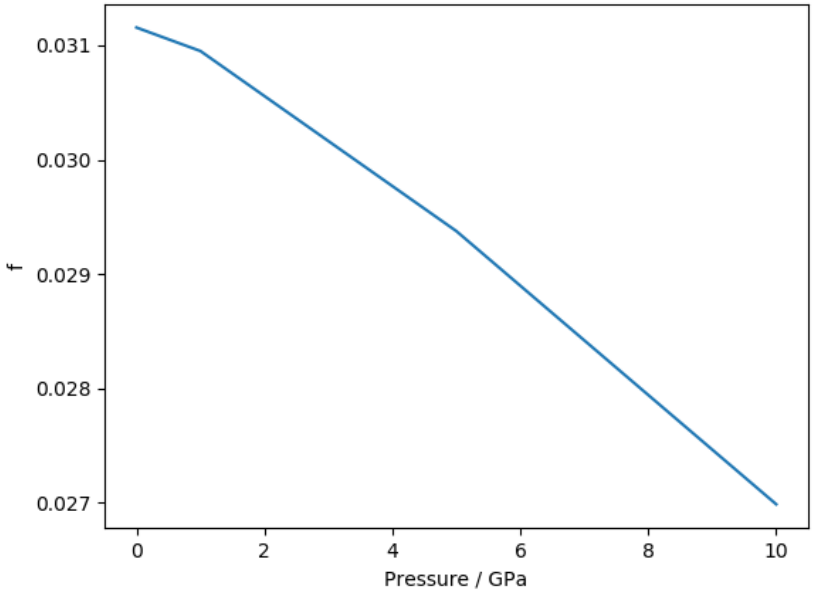

Figure 3.8: Dependence of specific heat capacity on temperature is characterised using the equation $c = c_0 + f(T/T_m)$. The parameter f, for Ta, is plotted here against pressure.

3.2.7 Nucleation and growth rate

Homogeneous nucleation rate, n_{hom}, and growth rate, u, have exponential relationships with temperature [42] (as was described in Chapter 2).

$$n_{hom} = n_0 exp\left(\frac{-\Delta G^*(T)}{kT}\right) exp\left(\frac{-Q}{kT}\right) \tag{3.2}$$

where

$$n_0 \sim \frac{nkT}{h} \tag{3.3}$$

and

$$u = u_0 exp\left(\frac{-Q}{kT}\right)\left(1 - exp\left(\frac{\Delta G}{kT}\right)\right) \tag{3.4}$$

Q is the activation energy of diffusion, $\Delta G^*(T)$ is the free energy barrier of nucleation and ΔG is the difference in free energy of the two phases. T is temperature, n is the number of atoms and k and h are the Boltzmann and Planck constants. The pre-exponential factor u_0 is, unlike n_0, independent of temperature.

This can be simplified to the equations

$$n_{hom} = ATexp\left(\frac{-B}{kT}\right) \tag{3.5}$$

and

$$u = Cexp\left(\frac{-D}{kT}\right)\left(1 - exp\left(\frac{E}{kT}\right)\right) \tag{3.6}$$

where the parameters A, B, C, D and E are found using best fit of the numerical melt model to the LAMMPS data.

The nucleation rate used in the final fit was linear with temperature and the growth rate was constant with temperature. This was a necessary approximation in order to reduce the number of fitting parameters, and was found to be valid as including the exponential terms did not alter the obtained profiles due to the relatively small temperature range during melting. However, this meant that the activation energy and energy barrier could not be extracted from the numerical method as initially hoped, as the approximate model is not sensitive enough to find those values accurately. Additionally, this approximation is less accurate at higher pressures (where there is a greater temperature range during melting, so temperature dependence becomes more significant) and at low heating rates (when the z-profile is less well defined, so is harder to fit to).

3.2.8 The coexistence method

Alternative techniques, which are well established for use in MD, were carried out to compare to the results from the numerical melt method: the coexistence and the hysteresis methods. The coexistence method incorporates solid and liquid regions in order to remove the nucleation barrier to melting as the interface between the two phases already exists. A description of this is given in Chapter 2. The method used here was based on Liu(2008) [64].

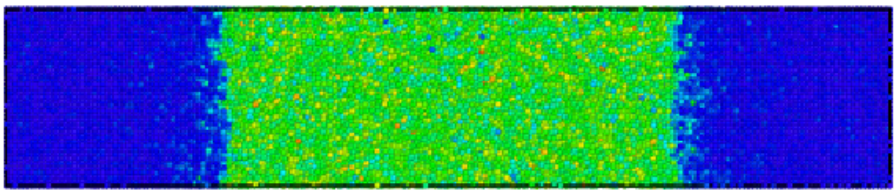

Figure 3.9: Image taken in OVITO showing the arrangement of atoms in the coexistence simulation, with a liquid in between two regions of solid. The colour scale is for CSP, with blue being 0 and green 10.

The setup of the LAMMPS simulation is shown in figure 3.9. The system was given periodic boundaries and the Cu Sheng potential was used [59]. The box size was 20x20x100 unit cells. The initial liquid region was defined as being from 25 to 75

unit cells in the z direction, with the remainder solid. The lattice parameter was adjusted to between 3.73Å and 3.64Å, to give a pressure range of 0 to 10 GPa. These values were obtained by running a small simulation separately for each temperature, to find which lattice parameters corresponded to each pressure.

The liquid region was set at 3000K (well above the melt temperature), and the solid at 300K. This was run in the NVE ensemble for 3000 timesteps of 0.001 ps to thermalise. The atom velocities were then rescaled to set both regions to the desired initial temperature, and the simulation was run for another 20000 timesteps in the NVT ensemble. Finally the NVE ensemble was used for 50000 timesteps, allowing the phases to change.

The required output values (given in a dump file) were CSP and z position, as it is how the liquid region grows or shrinks along the z direction that determines whether the system is in equilibrium. This equilibrium occurs at the melting point, so the simulations were repeated iteratively to find the melt temperature at each pressure.

3.2.9 The hysteresis method

The hysteresis method acknowledges the overshoot of one phase heating and cooling and uses them both to estimate the true static melt temperature [33].

$$T_m = T_l + T_s - \sqrt{T_l T_s} \tag{3.7}$$

T_m is the calculated melt temperature, and T_l and T_s are the overshot temperatures at which the phases changed, found when cooling and heating respectively. The hysteresis method was applied to each heating and cooling rate using one phase MD simulations. Again, the fix heat command was used to increase the temperature of the box (which started at 300K) to well above the expected melting point. The box was then cooled back to a solid. An example of this temperature profile is shown in figure 3.10. This was repeated at different pressures in order to plot the melt curve for comparison with other methods.

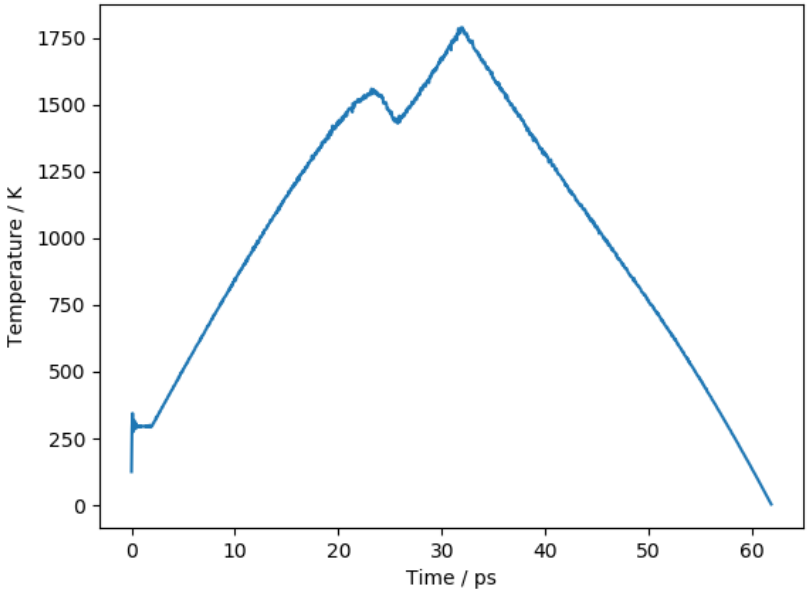

Figure 3.10: The evolution of temperature with time for the hysteresis method for Cu at 0 GPa. The solid is heated to a liquid and then cooled back to a solid. The z shape at around 20-25ps shows melting. The slight bend in the profile at about 50 ps is due to the change in specific heat capacity during and after freezing.

3.3 Results

The numerical melt method was carried out for Cu and Ta. This section begins with an analysis of the peak and trough positions of the LAMMPS data to estimate melt temperature and find latent heat and specific heat capacity. The numerical method is then applied to fit a melting model to the LAMMPS data and better determine melt temperature. This result is then compared to the coexistence and hysteresis methods.

3.3.1 Peak and trough positions

The effect of heating rate on the z-profile obtained in LAMMPS can be seen in figure 3.11. Increased heating rate increases the temperature of both the peak and the trough, as well as reducing the difference between them.

The variation of the peak with heating rate and pressure was found, and is shown in figure 3.12. The gradient of peak temperature against pressure is constant and matches the literature value of the static melt curve [55]. It can be seen that the peak temperature also increase with heating rate. Error bars were calculated by repeating the LAMMPS runs using six different velocity seeds. The errors are larger at lower pressures, possibly due to a greater relative difference in pressure between

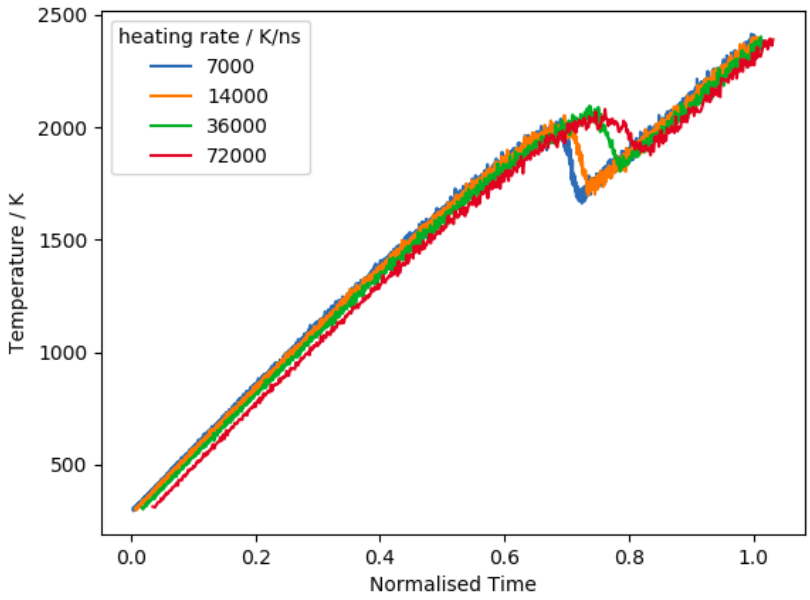

Figure 3.11: Graph showing the effect of the heating rate on the z profile for Cu at 10 GPa. Higher heating rates cause increased temperatures for both the peak and the trough. The time is normalised so that the plots overlay each other for easier comparison.

simulations with different velocity seeds.

Using the trough instead of the peak produced similar results, seen in figure 3.13. Again the trend is linear with pressure over this range, and is parallel to the literature melt curve. In this case, the lowest heating rate simulated (8000 K/ns) lies about 100K above the static literature value.

By plotting the temperature of the trough at 0 GPa as a function of heating rate, a static melt temperature can be inferred at a heating rate of zero. This is shown in figure 3.14.

At low heating rates, the temperature predicted by this linear fit is reasonably close to the expected melt temperature (1314K compared to the literature value 1358K), but as the trough positions do not converge to one value at lower rates, this is an inconclusive way of finding the static melt temperature. A different method, a numerical fit to the z-profile, is therefore required to find the static melt temperature from the temperature profile.

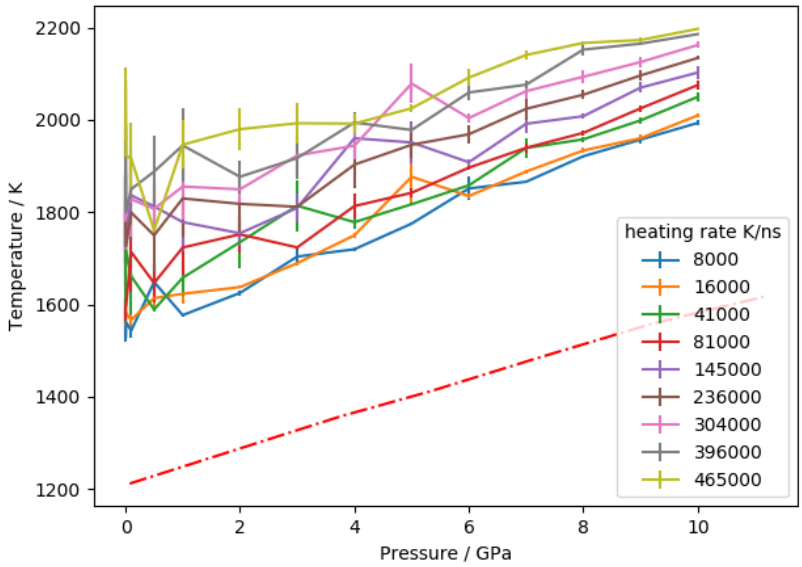

Figure 3.12: The temperature at which the peaks of the z-profile occur in Cu at different heating rates and pressures. Peak temperatures and error bars were obtained by averaging 6 simulations. The red dashed line is the static literature melt curve, taken from figure 3.1 [55], for comparison with the peaks.

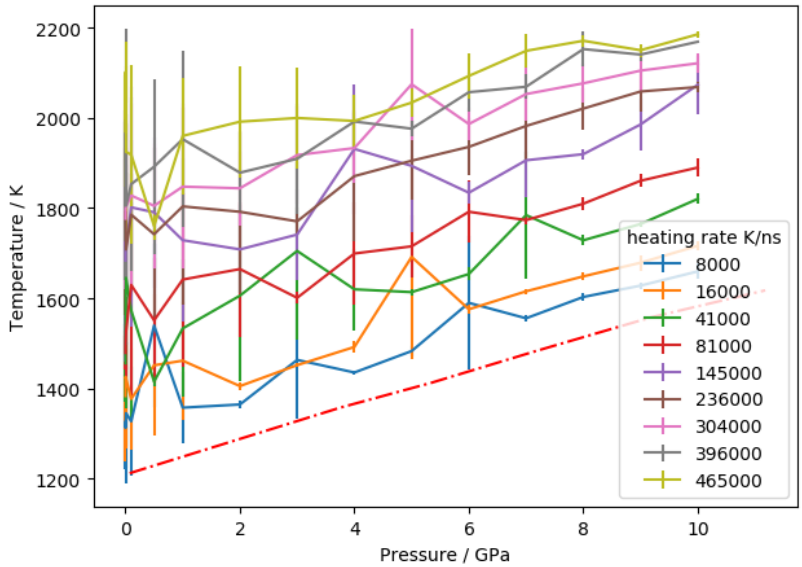

Figure 3.13: The temperature at which the trough of the z-profile occurs for different heating rates and pressures. Temperatures and error bars were obtained by averaging 6 simulations. As in figure 3.12, the red dashed line is the static melt curve, taken from figure 3.1 [55].

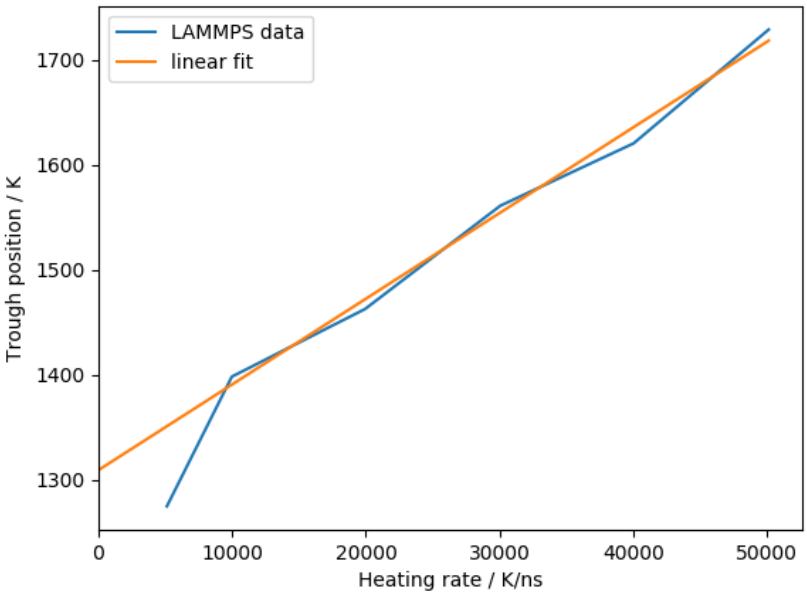

Figure 3.14: Melting temperature obtained from the value of the trough in the z profile against heating rate. At lower heating rates the linear fit approaches the literature static value of melt temperature, 1358K.

3.3.2 Latent heat and specific heat capacity

The latent heat was estimated from the z-profiles by subtracting the temperature of the trough from the extrapolated overshoot (found by continuing the temperature profile of the solid up to the time at which the trough occurs), to obtain the thermal energy which has been lost. This temperature difference, shown in figure 3.15, increases linearly with pressure. It decreases at higher heating rates, while maintaining the same pressure dependence. The specific heat capacity, calculated from the gradient of the temperature profile before melting, was then used, along with the temperature difference, to find the latent heat.

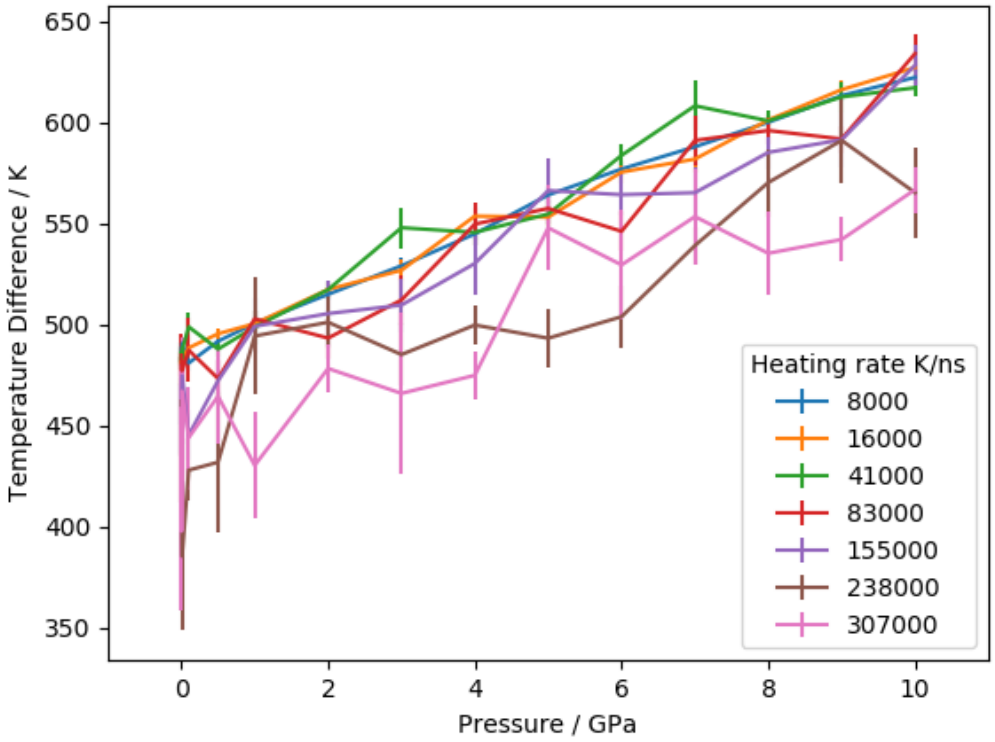

Figure 3.15: The temperature difference between the overshoot of the peak and the trough increases with pressure and decreases with heating rate. Error estimates are based on the standard deviation of six different velocity seeds and are larger at the higher rates.

The value for specific heat capacity of 0.42 J/gK obtained close to 0 GPa is 10% more than the literature value of 0.385 J/gK for Cu at 25^{o}C, which may be due to the potential used or because of the dependence of heat capacity on temperature, as discussed in section 3.2.6. The dependence of heat capacity with pressure is shown in figure 3.16; it decreases with increasing pressure but does not vary with heating rate. The difference between the simulated and literature values demonstrates the

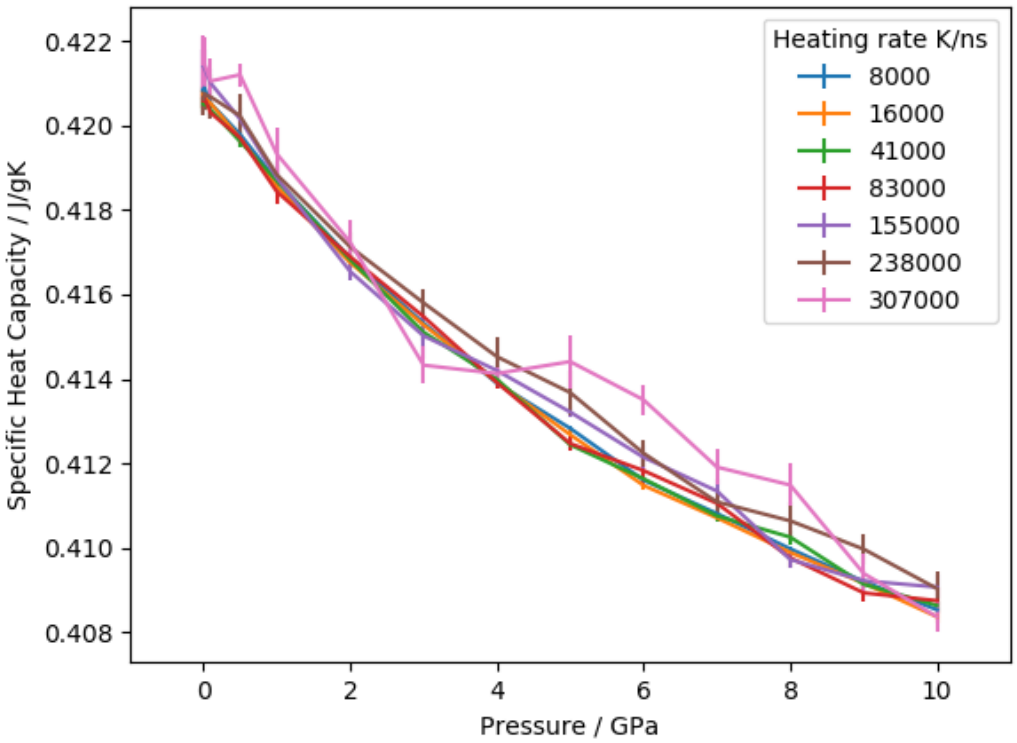

Figure 3.16: Specific heat capacity of solid Cu, calculated from the gradient of the temperature profile before melt, decreases at higher pressure. Error bars are calculated from the standard deviation of 6 simulations. The specific heat capacity is constant with heat rate within one standard deviation, with the exception of the highest heating rate which fluctuates, possibly due to a shorter time before melt increasing the error in the gradient.

need to check the melt curve against those predicted by static methods using the same potential, and not just the literature result.

Calculated latent heat of fusion is shown in figure 3.17. This increases linearly with pressure, and decreases slightly with increased heating rate. At a pressure of 0 GPa, the literature value of 13.05 kJ/mol is within one standard deviation of the calculated results at lower heating rates. Again, errors were found by using 6 different velocity seeds. The error bars are large, particularly at higher heating rates, at up to 10% of the value of latent heat.

These calculated values could be used in the numerical model, in order to reduce the number of fitting parameters.

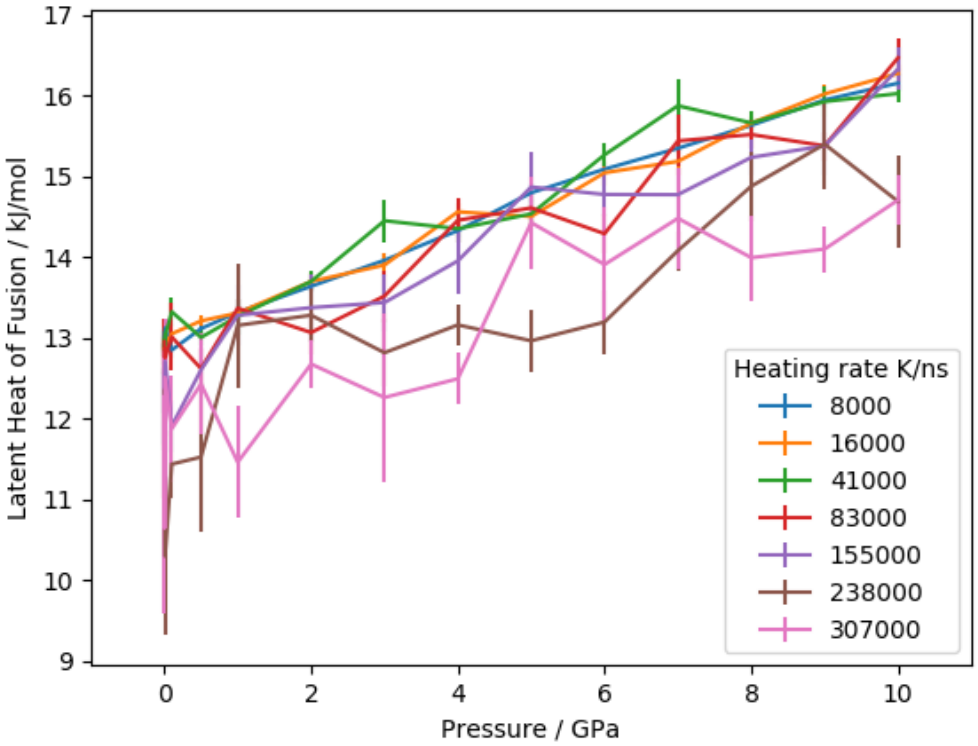

Figure 3.17: The latent heat of fusion for Cu is roughly linear with pressure and decreases at increased heating rate. Error bars generated from 6 velocity seeds are consistently large at all pressures.

3.3.3 Numerical melt model

Using the numerical method, a good fit could be found for the LAMMPS data. This is shown for Cu in figure 3.18 for a heating rate of 300 K/ps. The model predicts a melt temperature of 1350K at 0 GPa and a latent heat of 12 kJ/mol (literature values are 1358K and 13.05 kJ/mol [57]).

The pressure dependence of melt temperature up to 10 GPa is shown in figure 3.19. This matches the literature data [57] within the error bars for 7 out of the 10 data points. Errors were based on the sensitivity of the fit to the value of the melt temperature.

The calculated static melting temperature was constant with heating rate above 400 K/ps, which is an improvement over the peak or trough methods, as these were rate dependent at these heating rates, as shown in figure 3.20. It is also much more accurate, closely matching the literature melt curve. The specific heat capacity's temperature dependence changes with heating rate, so there is loss of precision in estimating this.

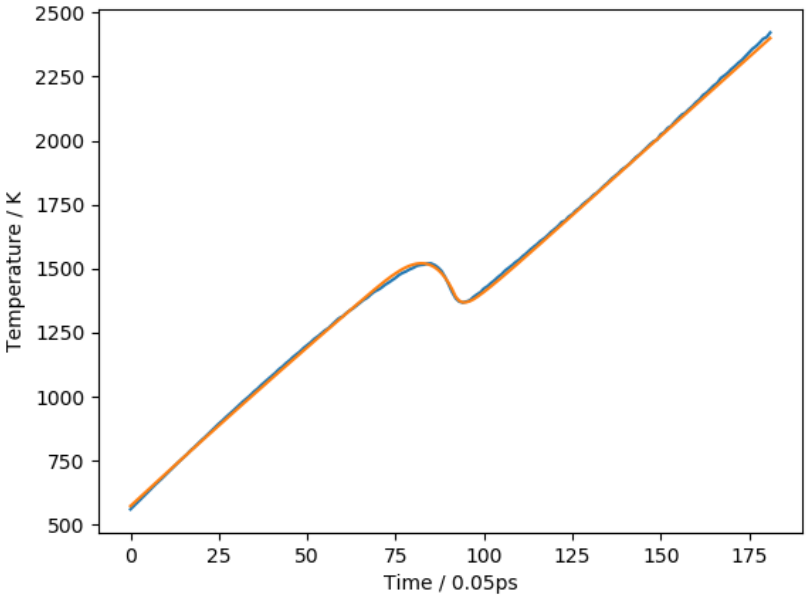

Figure 3.18: Fitting of the numerical method (orange) to LAMMPS data (blue). This was at a heating rate of 300 K/ps, with a box size of 20x20x20 unit cells, and time step of 0.05 ps.

The numerical method was applied to Ta as well as Cu, as shown in figure 3.21. This was repeated for different pressures in the range of 0-10 GPa (figure 3.22), and for each the model fits well to the LAMMPS simulations. It can be seen that the z-profile becomes sharper at higher pressure, and beyond this pressure range the fit becomes less accurate.

The melt temperature predicted by the numerical method is compared to the literature value [56] in figure 3.23. The values of temperature for the trough and the peak are also shown. It can be seen that the numerical method fits literature data well at pressures up to 12 GPa.

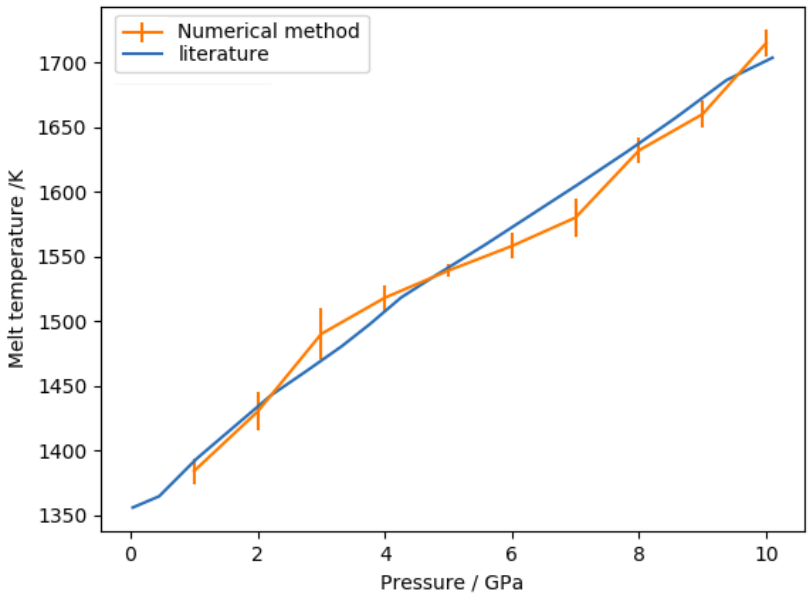

Figure 3.19: The melt curve of Cu up to 10 GPa, comparing literature data (blue) [57] with values obtained using the numerical method (orange). Errors are estimated from the range of melt temperatures which give a close numerical fit to the LAMMPS data.

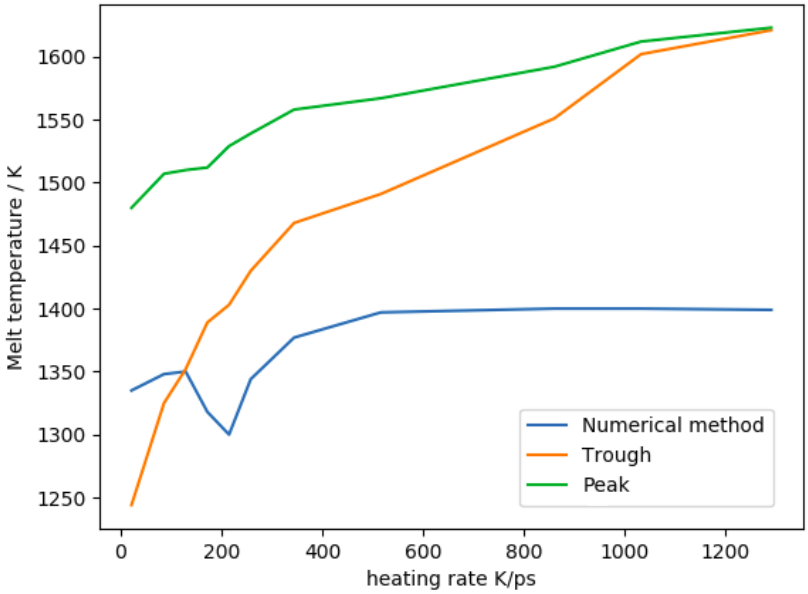

Figure 3.20: Comparison of the melt temperature obtained using the trough (orange) and peak (green) values, with the numerical method (blue) at 1 GPa. The numerical method gives a constant temperature at faster heating rates, while it breaks down at lower rates. At higher rates, it matches the literature melt temperature of 1380K. In contrast, when using the trough, the melt temperature increases rapidly with heating rate until the temperature profile loses its z shape and the peaks and troughs converge.

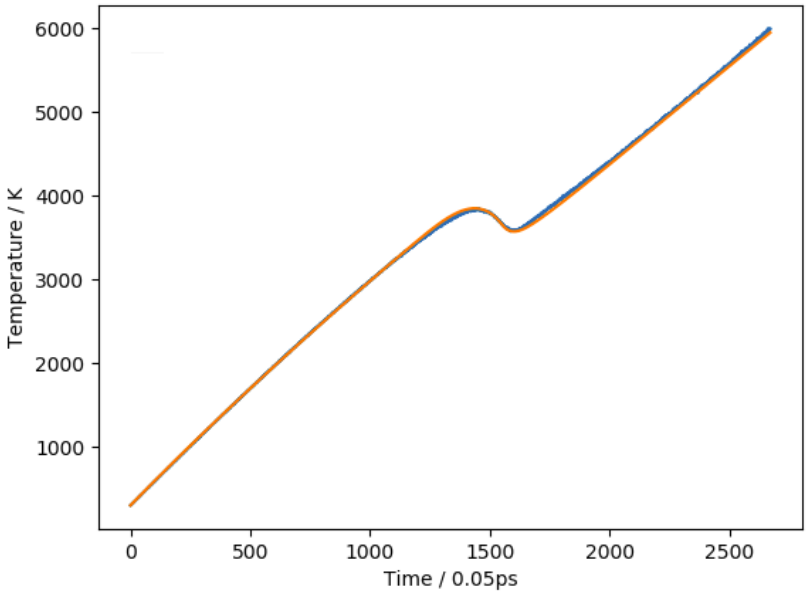

Figure 3.21: The numerical method fit (orange) to LAMMPS data (blue) for Ta at a heating rate of 600 K/ps, and pressure of 0 GPa. As for Cu, the numerical method fits the LAMMPS data closely.

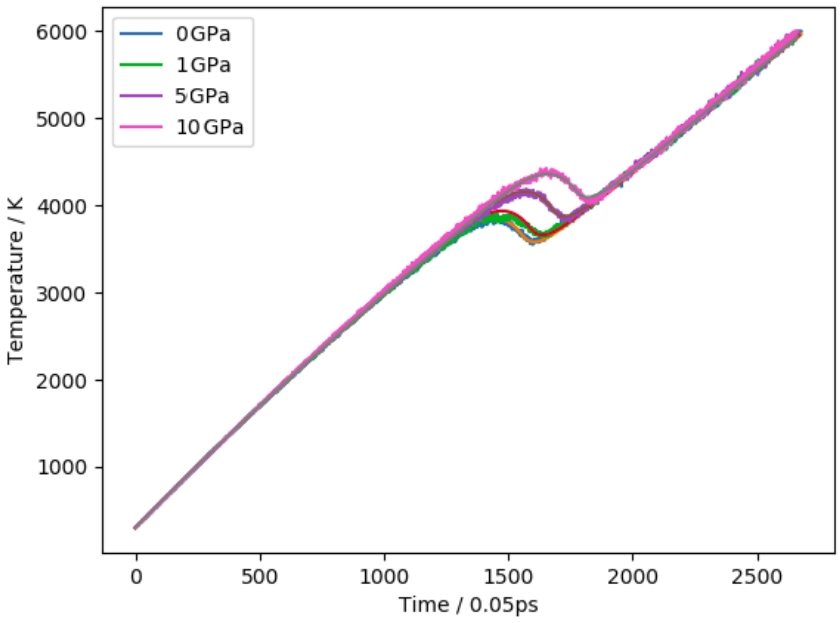

Figure 3.22: The z-profile for Ta is plotted at pressures from 0 to 10 GPa, with a heating rate of 600 K/ps at all pressures. Within this pressure range, the numerical method provides a good fit. Both the numerical method and the LAMMPS data are shown (with the legend referring to the LAMMPS profiles). The temperature difference between the peak and the trough increases with increased pressure, and the fit reproduces this.

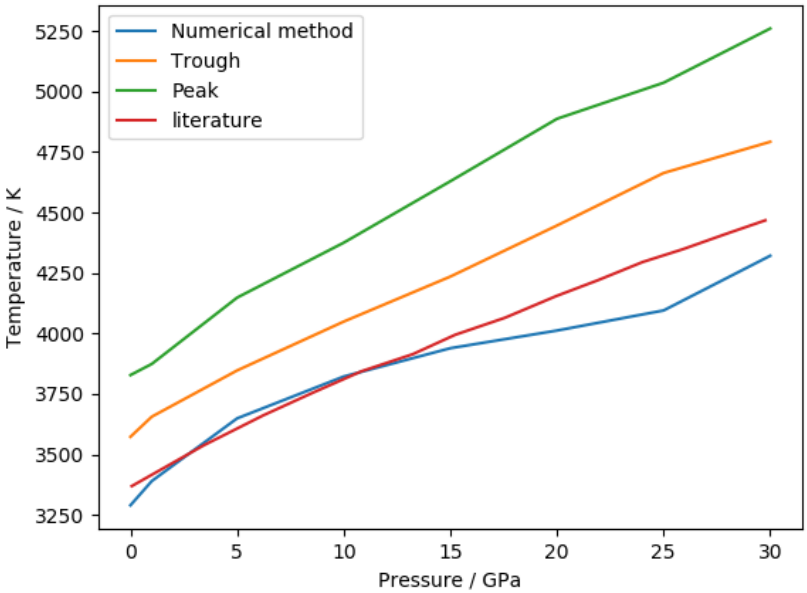

Figure 3.23: The melting temperature predicted using the numerical method (blue) for Ta, plotted against pressure. This is compared to literature values [56] (red), and shown to be a good fit below 12 GPa. The temperature of the peak and trough are also given.

3.3.4 Nucleation and growth

OVITO was used to image the atom positions, and mapping the CSP showed where melting occurred, which gave some information as to whether melting was growth or nucleation dominated. An alternative method to determine the melting mechanism was to plot a histogram of the variation of CSP of an atom's neighbours with the CSP of the central atom. Due to the large number of atoms present, a random sample of central atoms was selected (using a Python random number generator).

If the melting was nucleation dominated, then the CSP of the surrounding atoms would be independent of that of the central atom. If melting was growth dominated, then the CSP values should be correlated, as there would be a smaller number of large liquid regions. The histograms, shown for Cu in figure 3.24, demonstrate that the CSP of an atom is independent of its neighbours, implying nucleation dominated growth. The three figures are for before, during, and after melt.

Unlike Cu, for Ta there was not a sharp increase in CSP at the onset of melt. This can be seen in figure 3.25. However, the distribution of CSP when changing from a solid to a liquid, given in figure 3.26, remains the same as for Cu.

To check the change in CSP for Ta was not an artefact of heating, or due to the potential used, the CSP dependence on temperature was compared to CSP values obtained at static temperatures. This was then repeated using different potentials (Pun 2015 [65], Zhou 2004 [66] and Ravelo 2014 [67]), and the same CSP profiles were observed in all cases.

The absence of a sharp increase in CSP for Ta does not fundamentally change the numerical melt method suggested, but means that the average value of CSP cannot be relied upon alone for all metals to determine whether melting has started. Instead, OVITO or a similar tool can be used to check for the onset of melting.

As with Cu, the CSP distribution, given in figure 3.26, is independent of neighbouring atoms, so melting is again shown to be nucleation dominated.

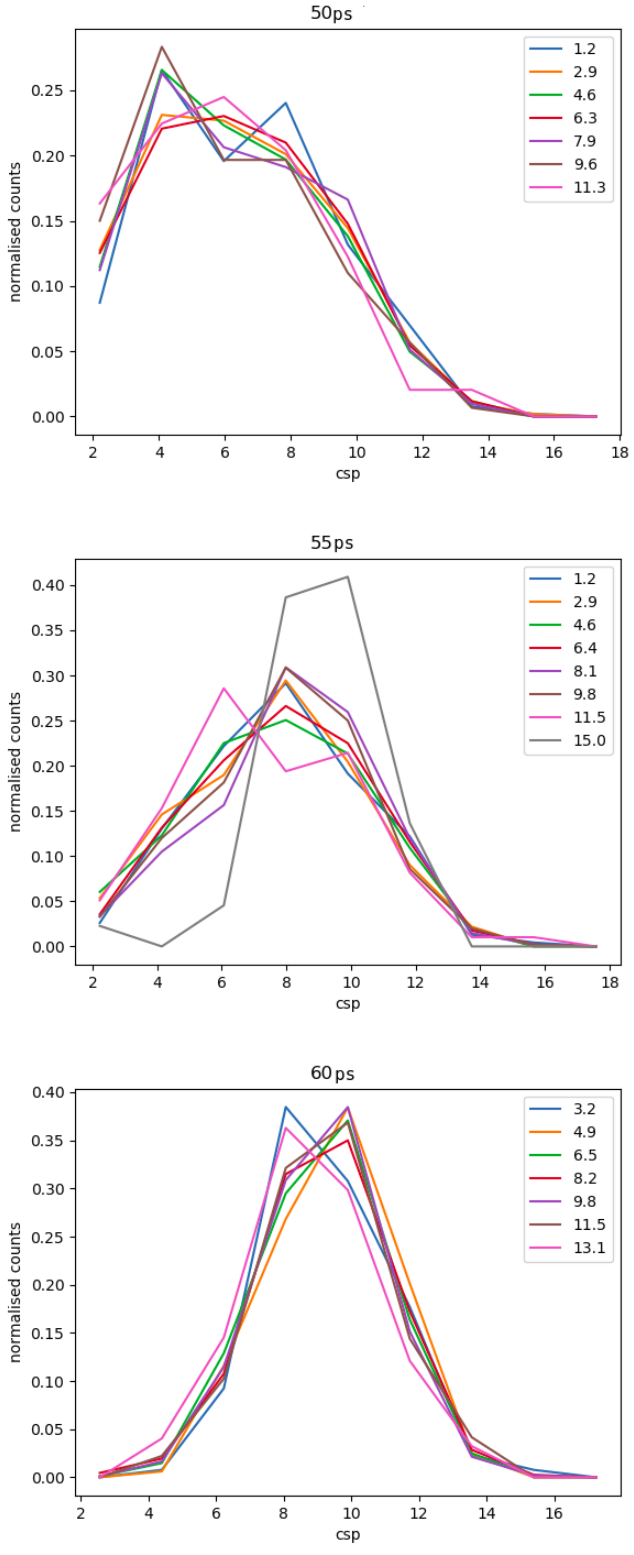

Figure 3.24: Distribution of the centro symmetry parameter (CSP) of neighbouring atoms, separated by the CSP of a central atom (with CSP of the central atom given in the legend) for Cu. The plots were taken at different times (given in the graph titles), and show the typical distributions of CSP for the material as a solid (top), liquid (bottom) and during melting (middle). In most cases the CSP distributions overlap; the only outlier is for the highest central CSP in the middle plot due to the low number of atoms preventing a smooth distribution forming. This shows that the CSP distribution is uniform throughout the sample during melting, rather than most of the melt occurring in a few large nucleation sites.

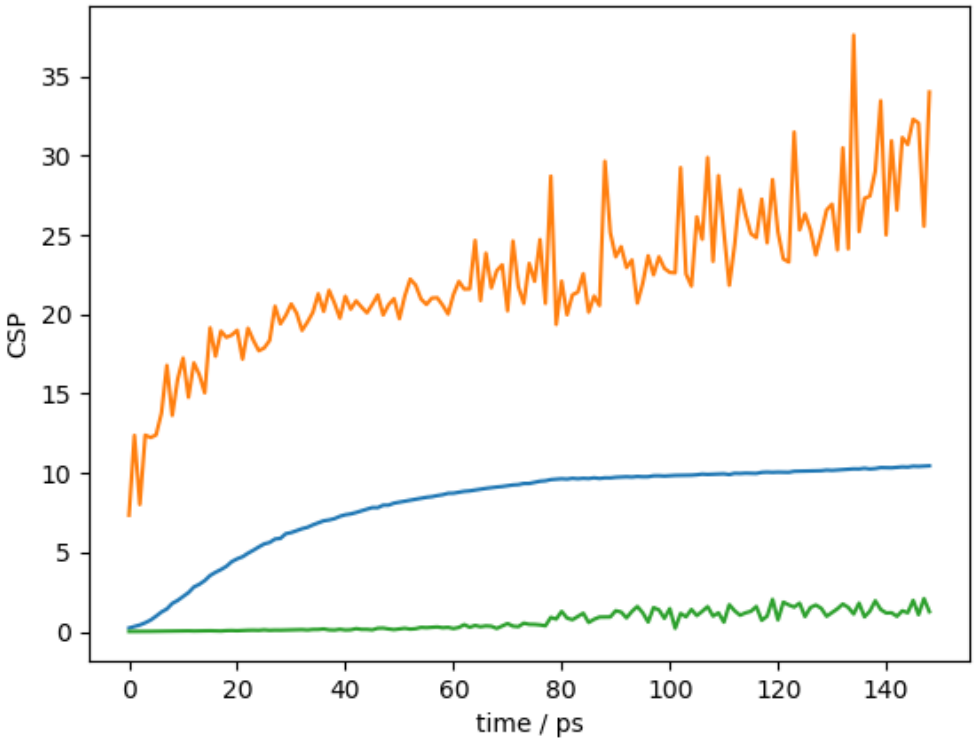

Figure 3.25: CSP against time during heating of Ta. The mean value is shown in blue with the maximum and minimum values given in orange and green. The onset of melt occurs at about 75 ps, as had been determined from the temperature profiles. In the CSP profile, this corresponds to a small jump in the mean value, but is more visible as an increase of minimum CSP.

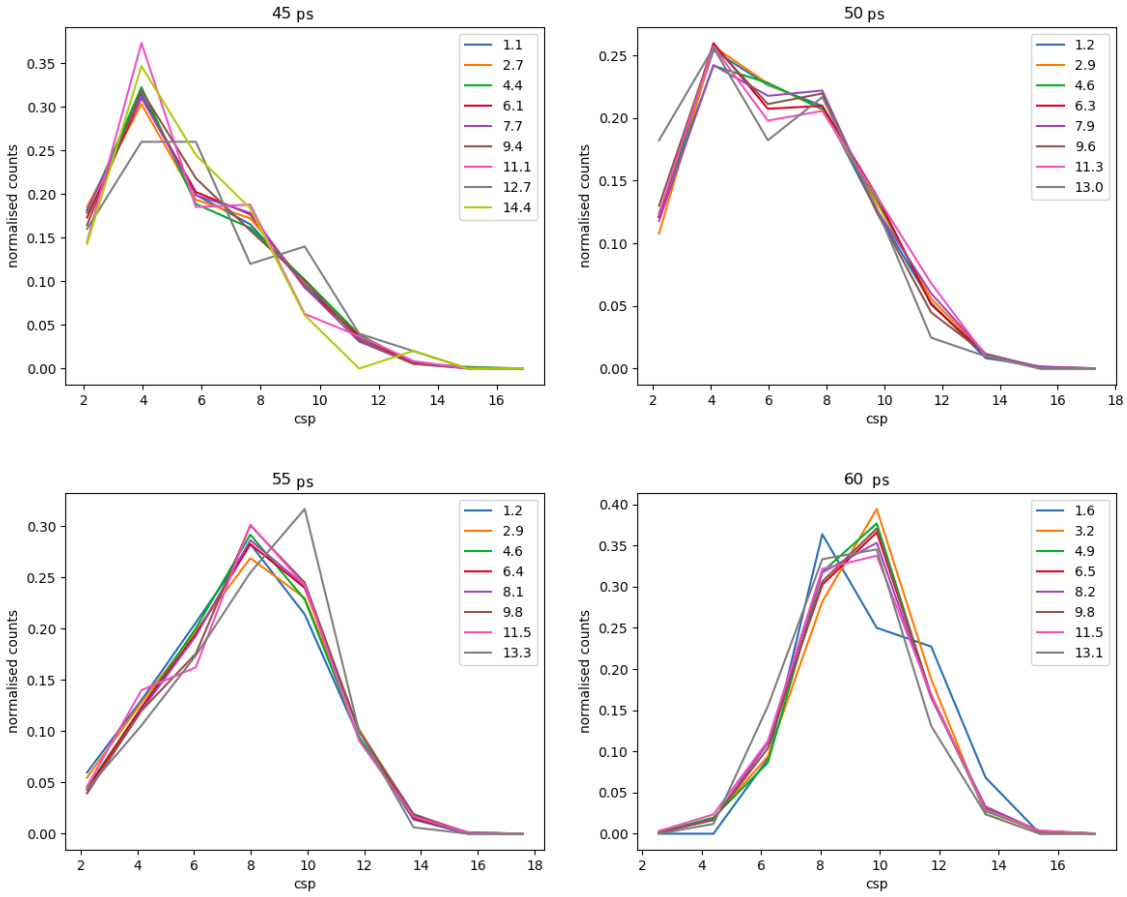

Figure 3.26: The evolution of CSP distributions of neighbouring atoms for Ta during melting, for the CSP of each central atom (given in the legend). Despite the difference in the mean CSP profile, these distributions before, during and after melting, are similar to those obtained with Cu shown in figure 3.24.

3.3.5 The coexistence method

In order to confirm that the numerical method works reliably, the predicted melt curve has been compared to results from other methods, as well as existing literature phase diagrams [55]. The melt temperatures were checked by using the same LAMMPS potential with methods known to produce accurate static results: the coexistence and the hysteresis methods.

The coexistence method is established as the standard way to find static melt curves in MD. With the method described in section 3.2.8, the CSP along the z direction could be used to define the solid and liquid regions, and to determine whether they were growing, shrinking or remaining stable. Examples of these are given in figure 3.27. The melting temperature occurs when the size of the liquid region remains constant.

This was found for a range of pressures to produce the phase diagram, shown in figure 3.28. The error bars are due to the range of temperatures at which the system appears to be in equilibrium, from the CSP plots. In most cases these are between 20-50K.

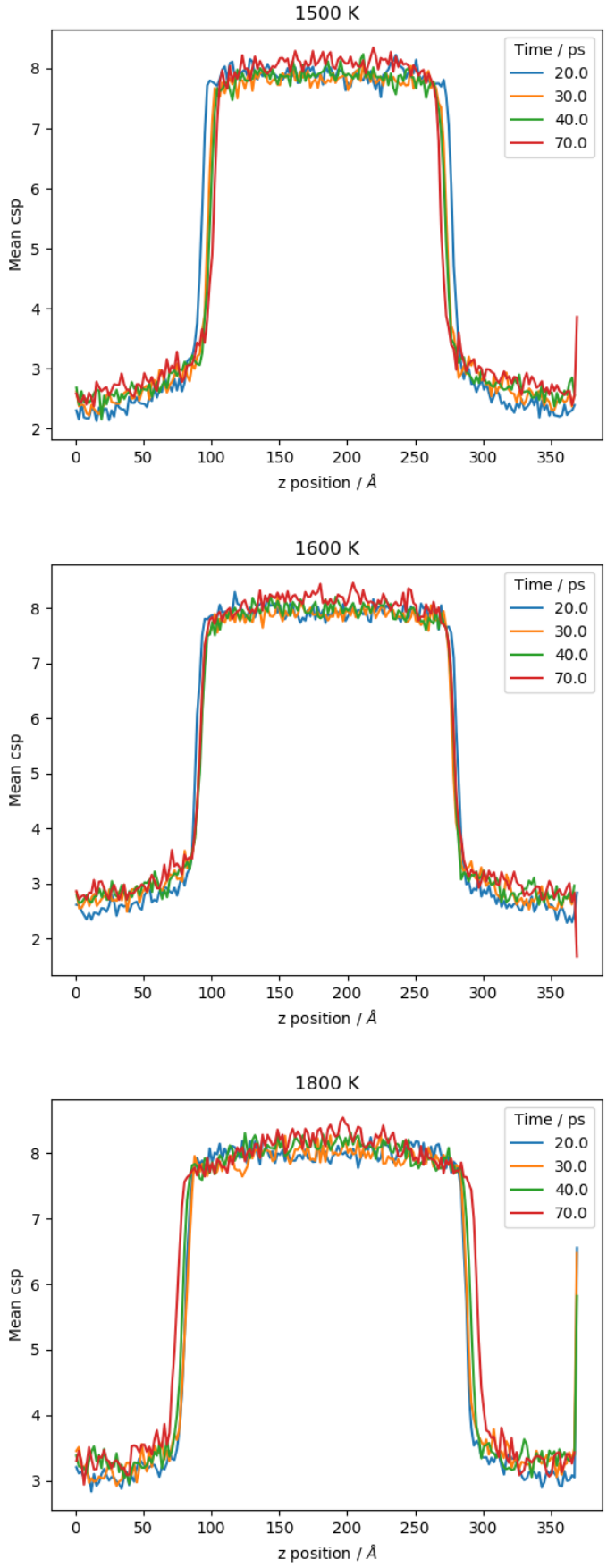

Figure 3.27: Mean CSP along the z direction for Cu at 7 GPa: 1500K (top), 1600K (middle) and 1800K (bottom). The higher CSP corresponds to the liquid region and the lower to the solid. The 1600K plot is in equilibrium, as shown by the overlapping vertical lines on the graph. This is therefore the melting temperature at this pressure.

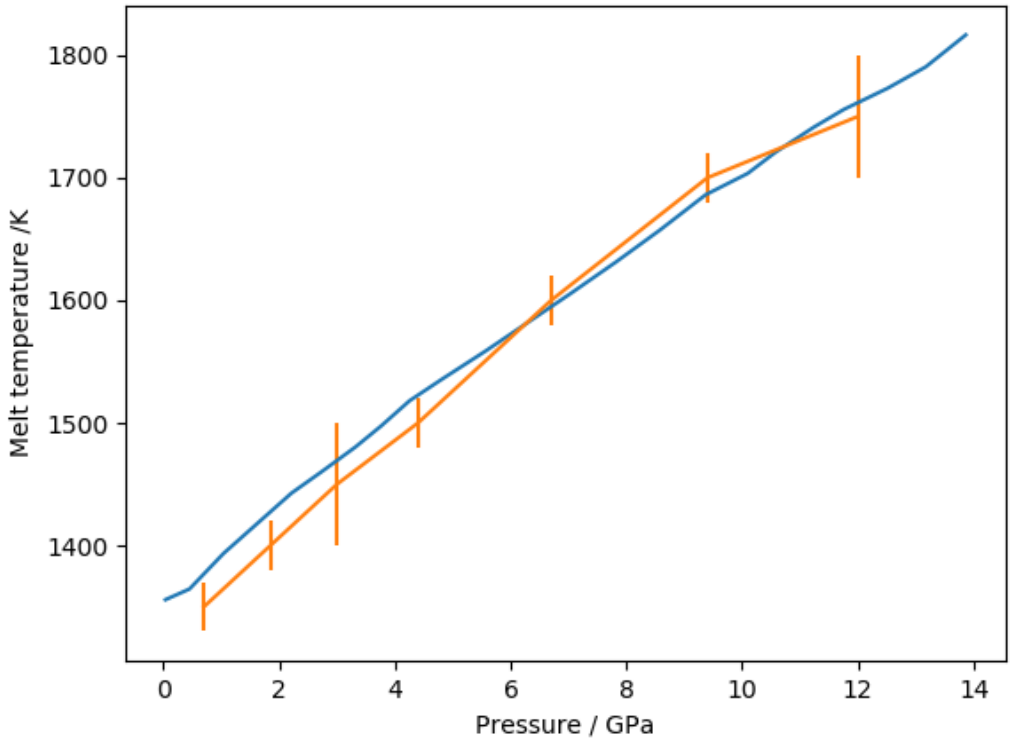

Figure 3.28: Melt curve formed for Cu using the coexistence method (orange). The error bars arise from the ambiguity as to when the system is in equilibrium. Within this error, it matches the literature curve (blue) [57] over the pressure range of 0-12 GPa.

3.3.6 Hysteresis method

The hysteresis method has the benefit of requiring small simulation times, but it does not have a physical basis. It is described in section 3.2.9, and uses the equation

$$T_m = T_l + T_s - \sqrt{T_l T_s} \tag{3.8}$$

T_m is the hysteresis melt temperature, and T_l and T_s are the melting temperatures obtained when cooling and heating. T_l and T_s can be found from the MSD shown in figure 3.29, and the temperature profile given earlier in figure 3.10.

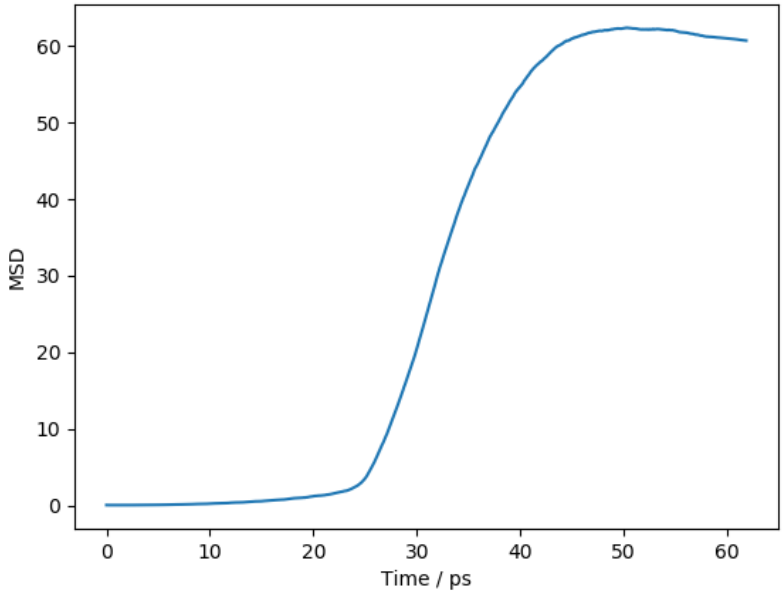

Figure 3.29: The change in MSD with time for Cu at 0 GPa, during heating and cooling for the hysteresis method. Liquid has a greater MSD than a solid, and both have an MSD which increases with temperature. Heating occurs until 32ps (well above the melting point), after which the system is cooled. The onset of melting can be seen when the gradient increases after 20ps, and freezing begins at the decrease in gradient after 40ps.

The phase diagram was again formed by repeating this method at a range of pressures, and is given in figure 3.30. The error bars are based on the imprecision in identifying when the gradient changes in figures 3.10 and 3.29, which indicate a phase change. This method has a large uncertainty, mainly from the T_l component, but agrees with the literature melt curve within this error.

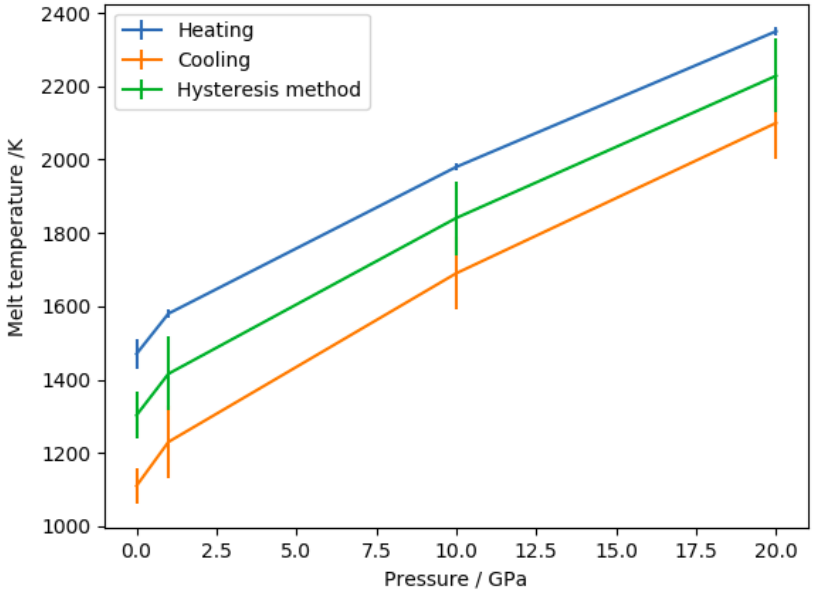

Figure 3.30: The melting curve for Cu obtained from the hysteresis method, up to 20 GPa, is shown in green. This is calculated using equation 3.8, from the superheated melting temperature (blue) and the supercooled freezing temperature (orange). Error bars are given for the uncertainty in temperature when the phase transition occurs. This is larger on cooling, due to the less well defined MSD change shown in figure 3.29. For both heating and cooling the rate of temperature change was approximately 40 K/ps (rate of energy change was constant across simulations, but heat capacity varies with pressure, meaning the rate of temperature change was not constant.)

3.4 Discussion

3.4.1 Peak and trough positions

When the heating rate was too rapid for an equilibrium to be established, the profile of temperature against time formed a z-profile upon melting. The peak and the trough of this profile were found to have an approximately linear dependence on heating rate and pressure. The trough temperature could be used to estimate the static melting point, as in figure 3.14, but it was due to the lack of accuracy that the numerical melt method was produced.

However, as specific heat capacity and latent heat could be determined (from the trough and the temperature profile), these parameters can be used for fitting in the numerical method, to reduce the number of free parameters.

3.4.2 Numerical melt method

The numerical method provided a close fit to the LAMMPS simulations. To check that this was not due to overfitting (meaning that any melt temperature could be made to fit well to the LAMMPS profile by adjusting the nucleation rate and growth rate parameters), the range of values that the temperature could take and still give a reasonable fit was used to form error estimates. The initial parameters were also varied, and this did not change the outcome, implying the function was successfully finding the optimum fit.

Approximations of the temperature dependence of growth rate and nucleation rate were required in order for the fitting to converge, but the close fit to the LAMMPS data implies that these were valid. The fit was worse when the heating rate was lower, and at higher pressures (above 15 GPa), both of which are situations where the approximations would be expected to be less accurate. For low heating rates, growth would have a greater impact rather than the melt being nucleation dominated. As pressure increased, so did the temperature difference between the peak and the trough, and therefore the temperature dependence of the growth and nucleation rates, which could be ignored at lower pressures, would have more of an effect.

Despite these limitations, the numerical melt model was able to fit closely to the LAMMPS data for both Cu and Ta, and reproduce the literature melt curves in the range of 0 to 10 GPa.

3.4.3 Comparison with other methods

As demonstrated in figure 3.31, the numerical method and the coexistence method (which were both carried out using the same LAMMPS potential) produce results which are in agreement with the literature value of the Cu melt curve [57]. Error bars are smaller for the numerical method. The hysteresis method also matched the literature, but had such large error bars that it was not considered further.

Computational cost is a major improvement for the numerical method over the coexistence method. For Cu, the numerical method can be carried out on a small box size of 10x10x10 unit cells, and has a wall time of 23 seconds to run on 20 cores. In contrast, the wall time of a coexistence simulation was about 20 minutes on 20 cores. The coexistence method could potentially be optimised in terms of reducing the box size slightly and the number of time steps, but as iteration is used to find the melt temperature, at least 5 simulations would be needed to predict the temperature to the desired level of precision.

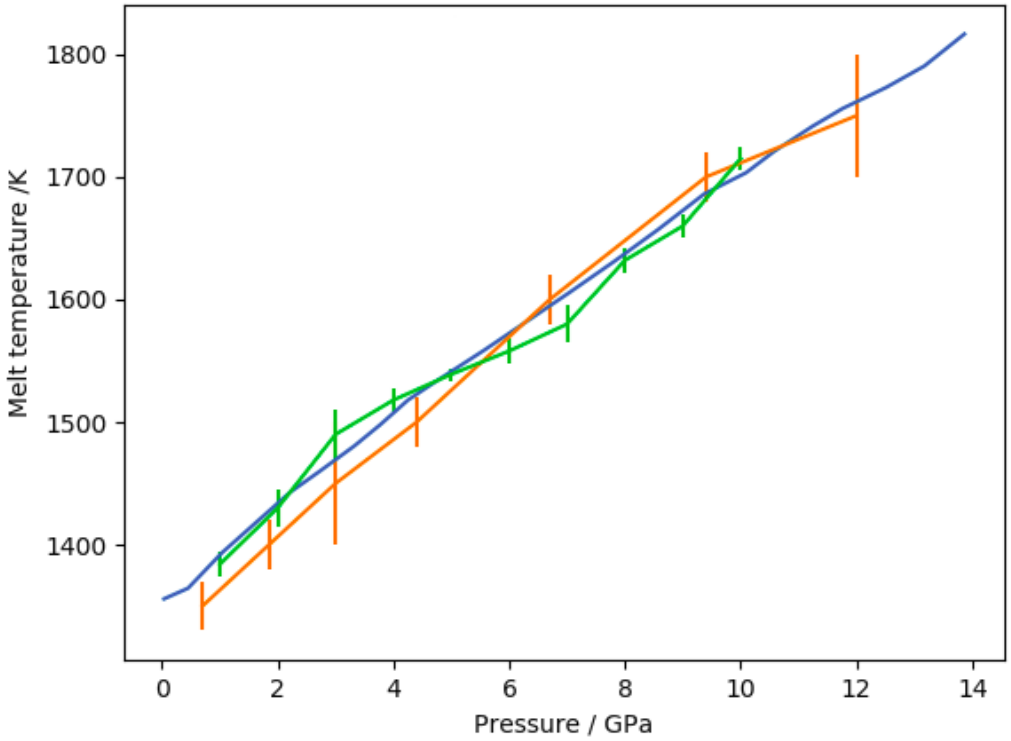

Figure 3.31: Graph showing that both the coexistence method (orange) and the numerical method (green) can be used to reproduce the literature value of the Cu melt curve (blue) in the pressure range 0-10 GPa. Errors for the coexistence method are from the range of temperatures where simulations showed equilibrium, and the errors of the numerical method are judged by the ranges which provided good numerical fits to the LAMMPS data.

For Ta, the numerical method again produced a melt curve which matched the literature, and the method had a similarly small computational cost.

3.5 Conclusion

Applying a numerical model to the temperature profiles of melting at rapid heating rates was shown to reproduce the static melt temperature for pressures in the range 0-10 GPa. This analysis has been carried out for both Cu (FCC) and Ta (BCC) with the same success, implying the method would be applicable for other simple metals. In each case, the numerical method accurately predicted (with an error of approximately 1%) the melt temperature of the metal, when compared to literature values and the coexistence method.

It was established that using the trough of the z-profile to find melt temperature is not accurate at high heating rates. Therefore in dynamic experiments, which are

required to determine the phase diagram at high pressures, the melt temperature obtained would not be equal to the static melt temperature. The method developed in this chapter provides a way of finding the static melt temperature at high heating rates using a numerical model to track liquid growth.

The numerical method uses a simple melt model, without applying the mechanisms of melt nucleation and growth, but even so produces a good match to the MD data. In addition to providing the static melt temperature in MD, with a greatly reduced computing cost compared with the traditional coexistence method, extra information such as the latent heat and specific heat capacity can also be extracted.

A box size of the order of 4000 atoms will generate a smooth and reproducible temperature profile. This is much lower than is needed for the coexistence method, which, when combined with the smaller number of timesteps, reduces the computational requirements by a factor of 100.

Kinetic variables such as energy barriers could not be calculated, as the model was not sensitive enough to fit multivariable equations to nucleation rate and growth rate without introducing large fitting errors and the risk of inaccurate results. However, further work could be done in this area to improve the fitting to include more variables, possibly by studying the CSP distribution to determine the dominant melt mechanism at each heating rate.

By applying a range of heating rates, the static melt curve has been found. While this analysis was carried out using MD simulations, it would also have applications in experimental methods. For example, in a high power laser shock experiment, the heating rate of the incoming shock can be modified, so obtaining the static melt curve from dynamic measurements should be possible. This could also be done on release rather than during the shock, using the tamper method simulated in Chapter 4.

Chapter 4

Finding static melt temperatures, using a tamper to control release rate

In Chapter 3, it was shown that the melt temperature observed in MD was heating rate dependent. In this chapter, this is expanded upon to find how it could be applied to a shock and release experiment.

For a typical shock target, the target material sits between an ablator (which interacts with the laser in order to form the shock wave) and a tamper (which determines the release rate of the material after a shock). Different tamper materials could therefore be used to alter the cooling rate during release, and, if melting occurs on release, allow the static melting point to be calculated from a set of dynamic results.

Simulations were carried out using the molecular dynamics code LAMMPS, and the tamper was modelled as a mobile wall. With Cu as a test material, this method produced static melting points, in the pressure range of 50 to 110 GPa, which agreed with the literature melt curve within the uncertainty in temperature of about 7%.

4.1 Introduction

In a dynamic system, the temperature and pressure at which melting occurs is not the same as the static melting point, and this difference is related to the heating or cooling rate. Laser shock experiments are dynamic systems, and melting can begin due to the initial shock wave, or during release after the shock. This chapter looks at the melting of Cu on release, using multiple cooling rates to calculate static melting points.

Cooling occurs as the release wave, formed when the shock wave reaches the tamper, travels back through the bulk material. As in Chapter 3, the MD code LAMMPS [58, 18] was used for the simulations. The tamper was modelled as a thin strip of material which moved in the direction of shock propagation to provide the correct release wave, but had no thermal velocity and did not interact with the atoms from the bulk material. Tampers need to be long enough to ensure that the second release wave, from the shock wave hitting the end of the tamper, comes too late to interfere with the main simulation, so developing a method where the tamper can be modelled as a thin wall greatly reduces the computational costs. The method also removes the requirement for a tamper material potential, and for an interaction potential between target and tamper. These are the main factors preventing tampers from being routinely modelled [54].

The LAMMPS model provided the temperature and pressure during release, as well as the centro symmmetry parameter which was used to determine the onset of melting. These were found for a slice of material close to the tamper.

For each tamper, the release paths in pressure-temperature should overlap, but have different end points. A power law fit (equation 4.1) was used to calculate the static melting point from several dynamic melting points produced by a range of tampers.

$$T_D = T_S + B\beta^z \tag{4.1}$$

T_D and T_S are the dynamic and static melt temperatures, β is the rate of temperature change, and B and z are constants. An equivalent expression was used for pressure.

The predicted static melt curve produced by this novel method was checked against the literature melt curve (Dai, 2002 [57]) and the melt curve found using the coexistence method, also modelled in LAMMPS. The agreement between the coexistence result and the literature means that the LAMMPS potential used is shown to be accurate in this pressure range.

Work in this chapter was carried out using MD simulations, but it was designed to replicate a laser shock set up. The information needed to find the static melt curve would be obtainable from diagnostics, so this method could be applied to experimental results with minimal change to the analysis.

This chapter is split into two parts: finding an efficient way to model a tamper in LAMMPS, and then using this method to control the release rate in order to infer a static melting point. Both of these topics have their own method, results and discussion sections.

Setting up the LAMMPS simulation and the effect of the tamper are described in section 4.2. The method is tested with several tamper materials, and compared to the expected release pressures in section 4.3, with the discussion in section 4.4.

In section 4.5, a power law fit is applied to the dynamic melting points, and the criteria for determining onset of melting is discussed. The calculated static melting points are compared to the literature and coexistence melting curves in section 4.6. The accuracy of the melt curve and the limitations and applications of this method are presented in section 4.7, and the conclusion to both parts is given in section 4.8.

Part 1: Modelling a tamper in LAMMPS

4.2 Method

4.2.1 Shock waves in LAMMPS

There are several methods to create a shock wave within LAMMPS. In this chapter, a piston is used. The piston acts as a wall which has no internal forces and does not interact with the bulk atoms, except to push them forwards in the direction of shock propagation causing a pressure wave. The velocity of the piston is constant throughout the simulation.

An alternative would be to use a piston with constant force rather than one with constant velocity, and this was tried and was shown to produce the same result. Other ways of producing shock waves in LAMMPS are discussed in Chapter 2. The constant velocity piston was seen as the most straightforward option in this case, as the velocity at which the tamper moves is related to the piston velocity, so it reduced the number of calculations required in the LAMMPS script.

4.2.2 The LAMMPS set up

These simulations were carried out on Cu using the Sheng potential [59], as in Chapter 3. As only one potential has been used to test this method, repeating with different potentials would provide further verification. However, as results obtained with the Sheng potential matched literature data within error bars, it was decided that this was not necessary. The two variables which were changed between simulations were the piston velocity and the linear scaling to this which controlled

the tamper response. The system modelled in LAMMPS was long and thin, as the z direction along which the shock travelled was the most important. At the start of the set up in the z direction was the piston which creates the shock wave, and at the end was the tamper which controls the release wave.

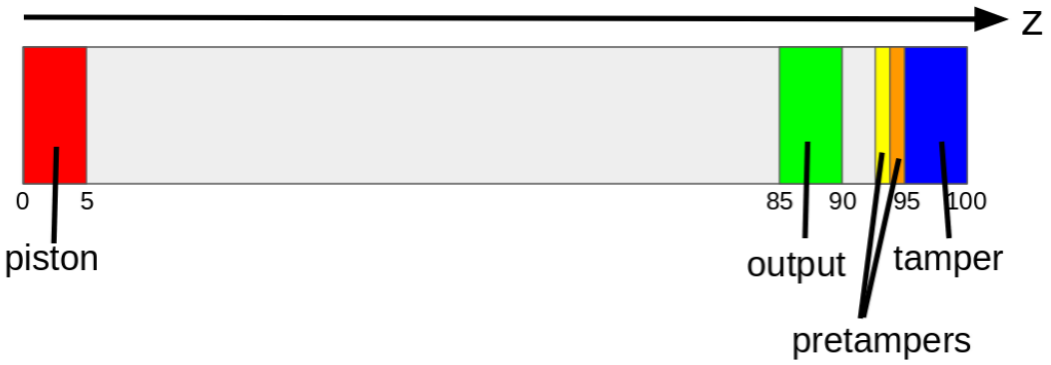

Figure 4.1: The set up of the LAMMPS simulations (not to scale). The scale along the z direction is in conventional unit cells. This shows the piston and the tamper at the ends. Data is taken from the output region and the two pretampers are used to calculate the tamper movement. The bulk material is from 5 to 95 unit cells, and this includes the output and the pretampers.

The dimensions were 10x10x100 conventional FCC unit cells, and the boundaries were periodic in the x and y dimensions and shrink wrapped in z. The different regions along the z direction were the piston from 0 to 5 unit cells, the bulk material from 5 to 95, and the tamper from 95 to 100 unit cells. Within the bulk material were three regions of interest: the output slice from 85 to 90 unit cells, the first pretamper from 94 to 95, and the second pretamper from 93 to 94 unit cells. This is illustrated in figure 4.1.

The output slice, where the data is taken, was chosen to be narrow in the z direction so that the responses to the shock and release waves could be considered uniform, while still containing a sufficient number of atoms to reduce noise. It was close enough to the tamper to be affected by the release wave but far enough away that it would not be used to calculate tamper velocity or experience surface effects. The purpose of the pretamper regions was to calculate when the tamper should move and at what velocity, and the method for this is discussed in section 4.2.5.

All the atoms were created with a temperature of 600K (which becomes 300K due to equipartition) to begin the simulation under ambient conditions. The seed for this velocity was varied for some of the data sets, to check that the initial distribution did not affect the end result. The time steps were 10^{-5}ps, as a consequence of the

potential used. As a result, the box size could be relatively small to reduce the run time of the simulation, as discussed in section 4.2.7. Thermodynamic variables were computed and printed every 1000 timesteps, which was less frequent than in the previous chapter due to the shorter time step.

An NVE ensemble was run for 10000 timesteps to allow the atoms to thermalise. This number of timesteps was found to be sufficient for the temperature and pressure of the simulation to stabilise. The piston and tamper then had their forces set to zero in all directions. The tamper was fixed at zero velocity and the piston was fixed at zero velocity in x and y, but given a constant velocity in the z direction. This stage of the simulation was run until the shock wave almost reached the end of the bulk material. The next step in the LAMMPS script (moving the tamper) is described in section 4.2.5.

4.2.3 Shock wave velocity

For a shock wave travelling through a solid, the shock velocity, U_s is related to the particle velocity, u_p by equation 4.2

$$U_s = Su_p + c_0 \tag{4.2}$$

where S and c_0 are constants for the material.

This equation is an empirical approximation which holds for most materials, and was demonstrated to be applicable in these simulations as the shock velocity, found from the gradient in figure 4.2, is linear with particle velocity, as shown in figure 4.3. The constants S and c_0 of the bulk material, which are required to calculate the tamper velocity, can therefore be determined within the LAMMPS simulation if they are not already known.

Pressure in the bulk material, P, can be found from the shock and particle velocities and the density before the shock, ρ_0, using equation 4.3.

$$P = \rho_0 U_s u_p \tag{4.3}$$

In figure 4.4, equation 4.3 is used to compare the predicted shocked pressure to the pressure calculated using LAMMPS outputs at different particle velocities. They are a reasonable match, again implying that the linear relationship between U_s and u_p is valid in these conditions, and that the method of calculating pressure in LAMMPS, discussed more in section 4.2.6, is correct. This is repeated for several elements, using the Rusbank database [68], in figures 4.5 and 4.6.

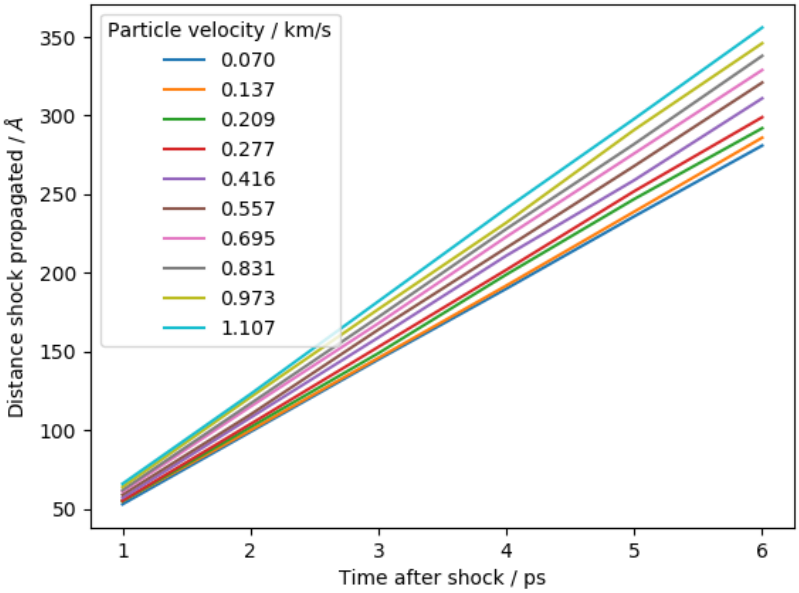

Figure 4.2: The velocity of the shock wave in Cu is calculated from the gradient of displacement of the shock front with time. This was carried out at different particle velocities, and all gave linear displacements, as would be expected if the shock wave did not dissipate.

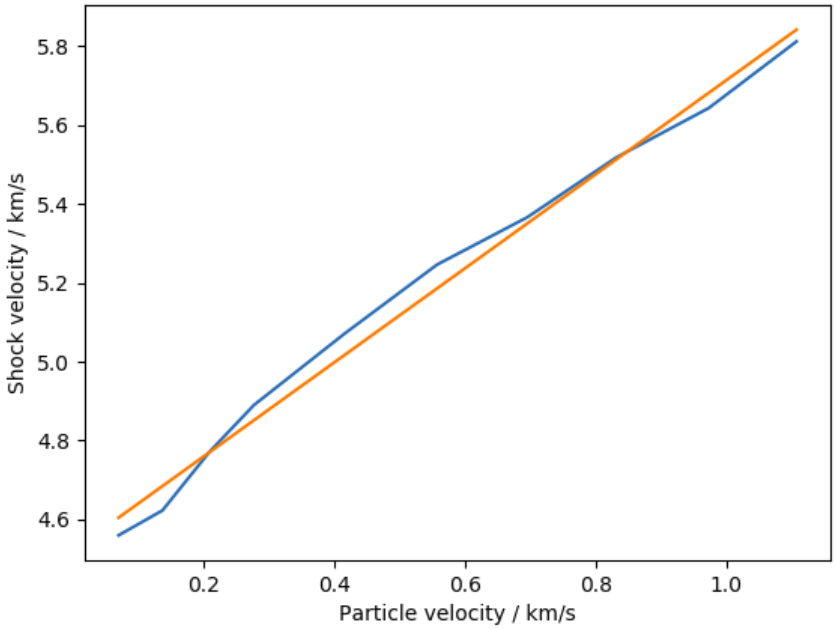

Figure 4.3: The velocity of the shock wave (calculated from the speed of the shock front) against particle velocity for Cu. The LAMMPS data is in blue, with the linear fit in orange, to calculate c_0 and S.

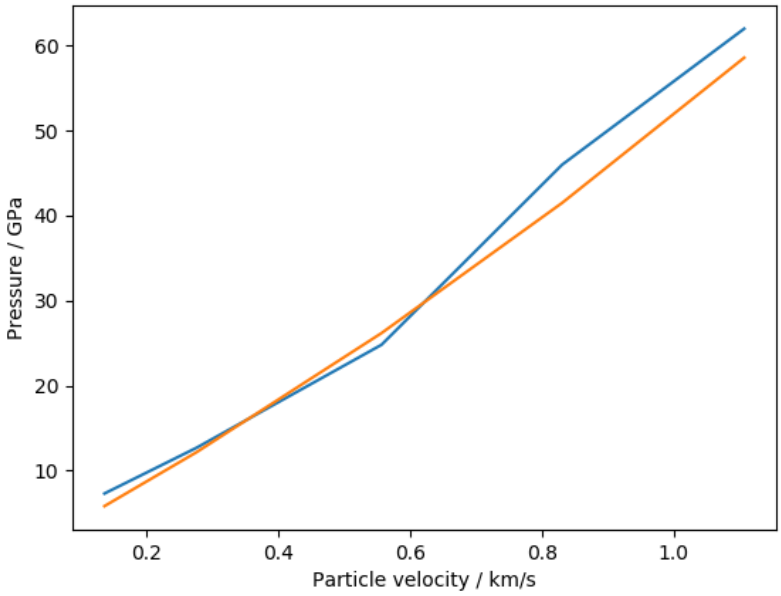

Figure 4.4: The pressure measured in LAMMPS (blue) matches the pressure calculated from the particle and shock speed (orange) for Cu.

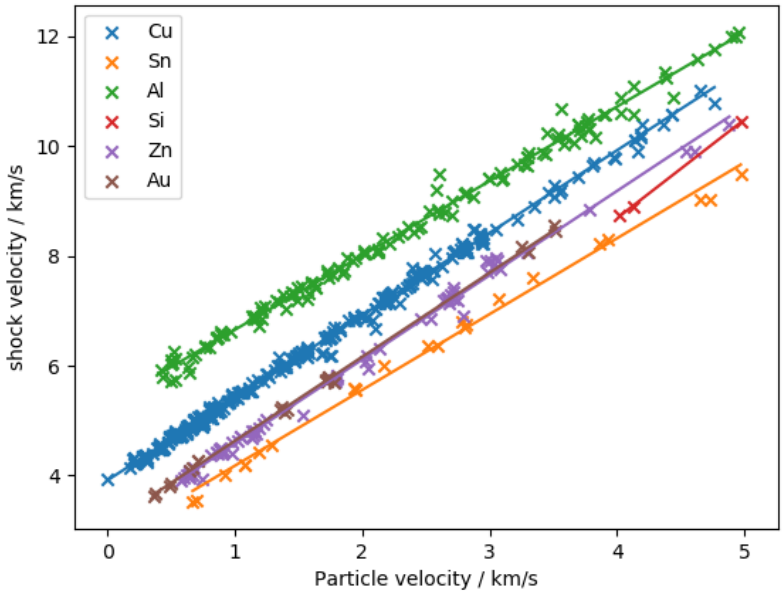

Figure 4.5: Shock velocity is linear with particle velocity. The data points are from the Rusbank database [68], for the elements given in the legend. The linear fit can be used to find c_0 and S from equation 4.2, to be incorporated in the LAMMPS simulations.

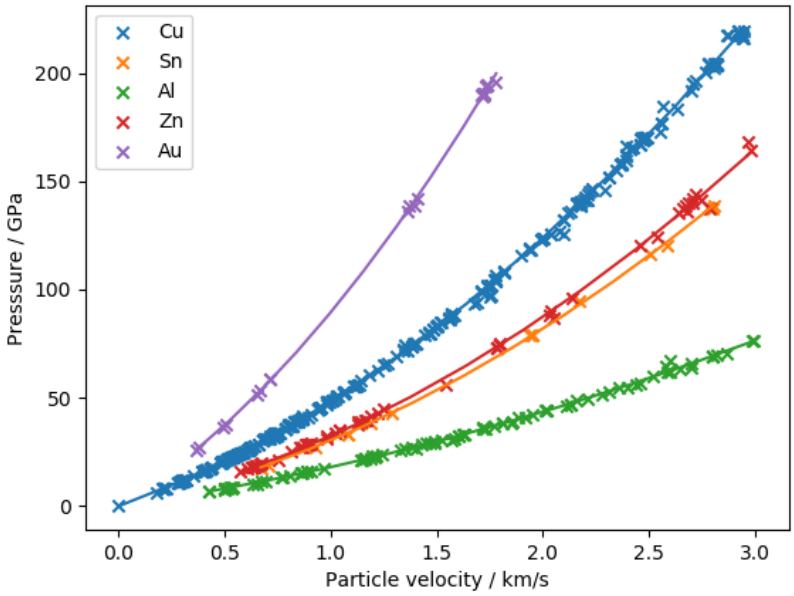

Figure 4.6: The dependence of pressure on particle velocity is found from the Rusbank database [68]. A quadratic equation is fitted for each element, and is in good agreement with the data, as expected from equation 4.3.

4.2.4 Tampers

The effect of the tamper is dependent on the Hugoniot relationship between pressure and particle velocity for both the tamper and the bulk material. The release pressure can be found by combining equations 4.2 and 4.3. Figure 4.7 shows this process for Cu with an Al tamper.

In figures 4.7 and 4.8, the pressure-velocity profile for the bulk material (blue) is reflected at an initial particle velocity, to find the possible release waves [47], as described in Chapter 2. The release particle velocity is found where this reflected line (orange) intersects with the Hugoniot of the tamper material, as seen in figure 4.7. However, if the tamper has a greater shock impedance than the bulk material, the pressure will increase, as a new shock wave will be reflected. This is known as ringing up the target, and is shown in figure 4.8 for Cu with an Au tamper.

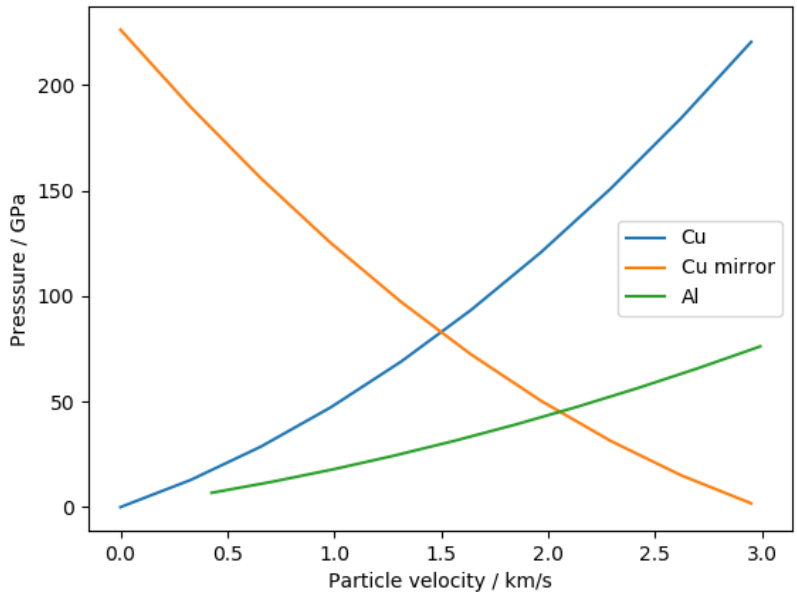

Figure 4.7: The release conditions are found using the mirror image of the velocity-pressure profile at the particle velocity which achieved compression. With a tamper material, the release pressure is found where the bulk mirror image profile intersects with the profile for the tamper material. Here the graph of a Cu target with an Al tamper is shown, with an initial particle velocity of 1.5 km/s, leading to a release pressure of approximately 40 GPa.

This process is described in the following equations. The Hugoniot pressure as a function of particle velocity for the bulk and the tamper have the same form

$$P_H(u_H) = \rho_{0B}(c_B + S_B u_H)u_H \tag{4.4}$$

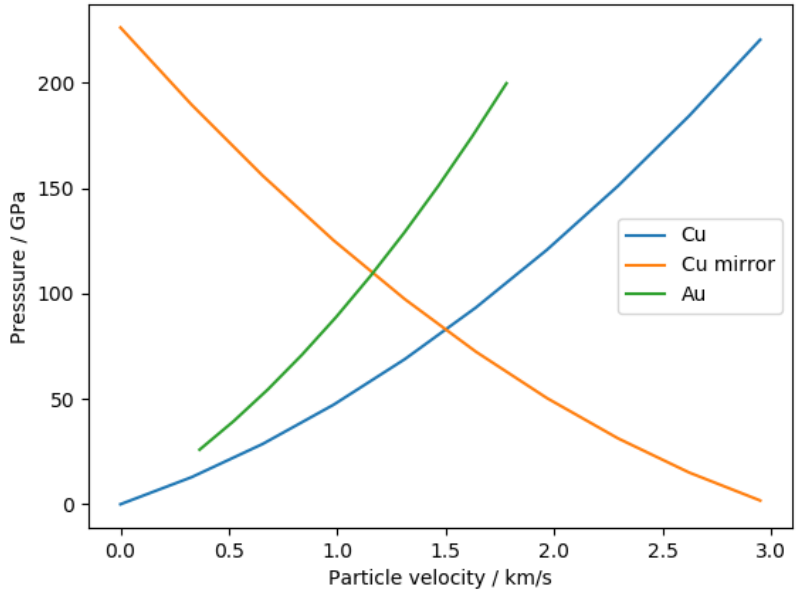

Figure 4.8: When the tamper has a greater shock impedance than the bulk material, shown here for Cu with an Au tamper, the pressure will increase, as a new shock wave will be reflected. The new pressure is again found at the intersection of the tamper pressure-velocity profile and the mirror image of the bulk profile.

$$P_T(u_T) = \rho_{0T}(c_T + S_T u_T)u_T \tag{4.5}$$

where P_H and u_H are the pressure and velocity on the Hugoniot for the bulk material, with the bulk constants of c_B and S_B and initial density ρ_{0B}, and similarly for the tamper in equation 4.5. Equation 4.4 is reflected at a particle velocity for a particular shock u_P to form the release path described in equation 4.6, with the mirror image pressure P_M.

$$P_M(u_H) = \rho_{0B}(c_B + S_B(2u_P - u_H))(2u_P - u_H) \tag{4.6}$$

This mirrored pressure intersects with the tamper pressure at the particle velocity u_R, which is the particle velocity of the tamper and the release wave.

$$P_T(u_R) = P_M(u_R) \tag{4.7}$$

Repeating this process at different initial particle velocities, u_P, gives the reflected release particle velocities, u_R. The relationship between u_R and u_P is shown to be linear (over the range of particle velocities which produce the appropriate pressures) in figure 4.9. The piston velocity in LAMMPS which causes the shock wave is the same as the particle velocity of the shock.

The entire tamper does not need to be modelled; as shown in section 4.4, a thin wall like the piston will be sufficient. As well as reducing the computational requirements,

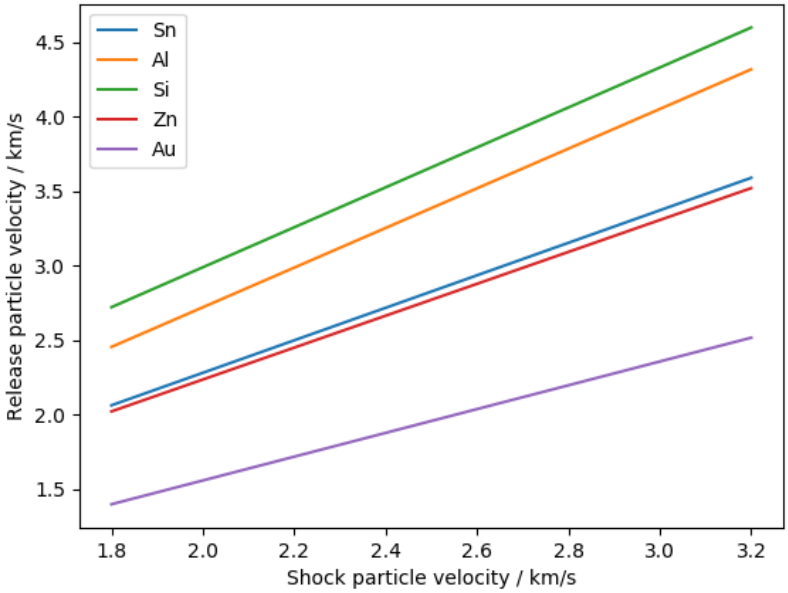

Figure 4.9: Using the method described in this section, the tamper velocity can be calculated for each shock particle velocity. The results shown here are for a Cu target, with the tamper element given in the legend.

this means that tampers for which there is no potential can be used, provided the relationship between pressure and particle velocity is known. This can either be found directly in databases such as Rusbank [68], as in figure 4.6, or from knowing c_0, S and ρ_0.

To obtain a full set of data in section 4.5, a range of values for u_R/u_P from 1.6 to 2 were used in the LAMMPS simulations, which did not correspond to any particular physical tamper materials. When u_R/u_P is equal to 1 there is no release, and at 2 there is complete release from a free surface. Below a u_R/u_P of 1.6, melt did not occur for all pressures, as the release path did not cross the melt curve, so this range was not included. However, real materials were also modelled to confirm that this method is valid, with the results given in section 4.3. The range of piston velocities was chosen so that the shocked state remained solid, but the release path crossed the melt curve.

4.2.5 Moving the tamper

The velocity of the tamper in LAMMPS becomes a variable as the shock approaches it and the time at which this occurs is calculated from the shock velocity. The tamper velocity was increased using the fix move command. The change in velocity, dv, is

found using equation 4.8.

$$dv = (u_R - v_t)(v_{pt1}^3/v_{pt2})\text{x}10^{-6} \tag{4.8}$$

where the release velocity, u_R, is the desired tamper velocity (dependent on the tamper material) and v_t is the current tamper velocity. v_{pt1} and v_{pt2} are the velocities of the pretamper regions, with v_{pt1} being closer to the tamper. All velocities are taken in the z direction. This equation would fail if v_{pt2} was exactly equal to zero; however, there were thermal fluctuations in the model and the value was precise enough that this was never the case. The simulation then continued for long enough for the release wave to reach the piston.

Equation 4.8 was developed empirically to give the tamper velocity a smooth step function which begins when the shock wave hits the tamper, shown in figure 4.10. The velocity of pretamper 2 displays the desired effect: the peak at 3 km/s is the particle velocity of the shock wave, and the end velocity of 4.2 km/s is the velocity of the release wave.

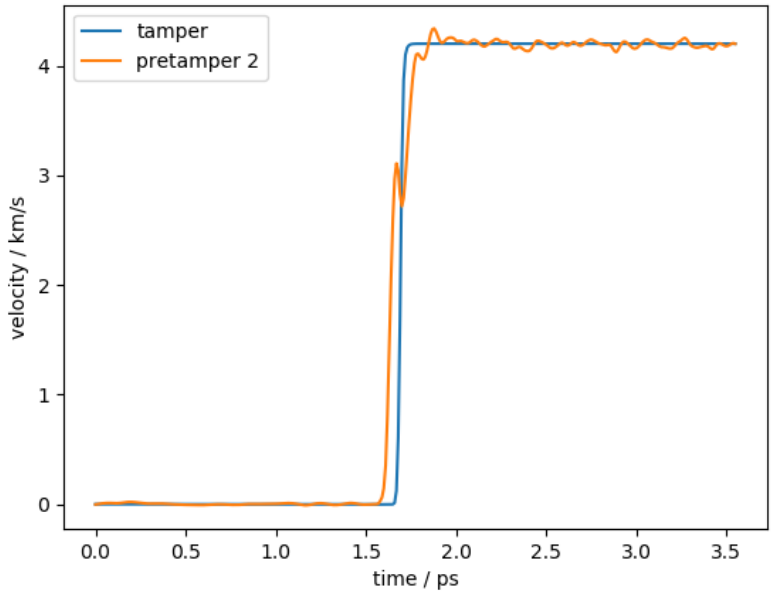

Figure 4.10: Graph showing the mean particle velocities in the z direction in the tamper and a pretamper region. The tamper (blue) starts moving in the direction of the shock when the shock front reaches the pretampers. The final velocity of pretamper 2, and of the release wave travelling back, are equal to the tamper velocity. The peak in the pretamper 2 velocity at 3 km/s is the particle speed of the initial shock wave in this example.

4.2.6 Defining pressure

The pressure from the LAMMPS simulations was calculated using the stress per atom and the Voronoi volume. Only the components of stress in the x and y directions were used, because the waves travelled in the z direction. This is known to be valid for a fully plastic system, and has been shown to be a reasonable assumption here, as the pressures of the Hugoniot found using LAMMPS matched the literature [57]. Using different piston velocities, the Hugoniot was traced out and compared to the literature phase diagram for Cu. This is shown in figure 4.11. The agreement with the literature Hugoniot values also suggests that the LAMMPS potential chosen is accurate within this pressure range.

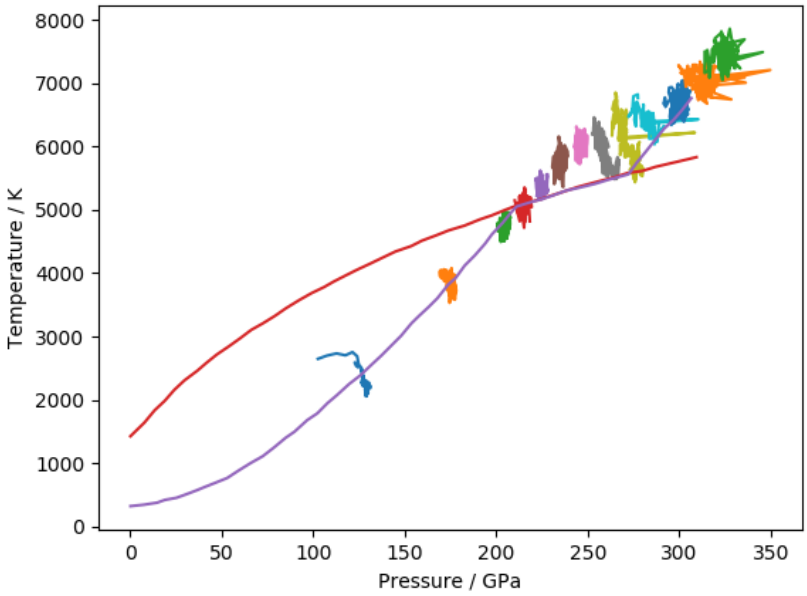

Figure 4.11: Comparison of the Hugoniot from the LAMMPS set up and the literature. The literature Hugoniot [57] is shown in purple and the melt curve in red. The coloured points show the pressure and temperature achieved in LAMMPS after different shocks. These were taken over a period of time, so are lines rather than points. The grey, olive and pale blue lines show release back to the Hugoniot after overshooting due to the high compression rate.

4.2.7 Box size

The Sheng potential [59] was used for Cu due to its accuracy of the Hugoniot and melt curve. A consequence of this was that the time step needed to be very low (10^{-5} ps) in order to cope with the high pressures, and so the box size was reduced to keep the simulation run time reasonable. It was therefore necessary to carry out tests on larger boxes to ensure that the small size did not reduce the plastic effects or delay the onset of melt.

In figure 4.12, the pressure temperature profile is shown for different sized boxes. As the paths overlay each other, both on compression and release, plasticity is not affected, and the smaller box size of 10x10x100 unit cells can be used. There is some variation between the plots, but as this does not correlate with box size, it can be dismissed as noise between different runs.

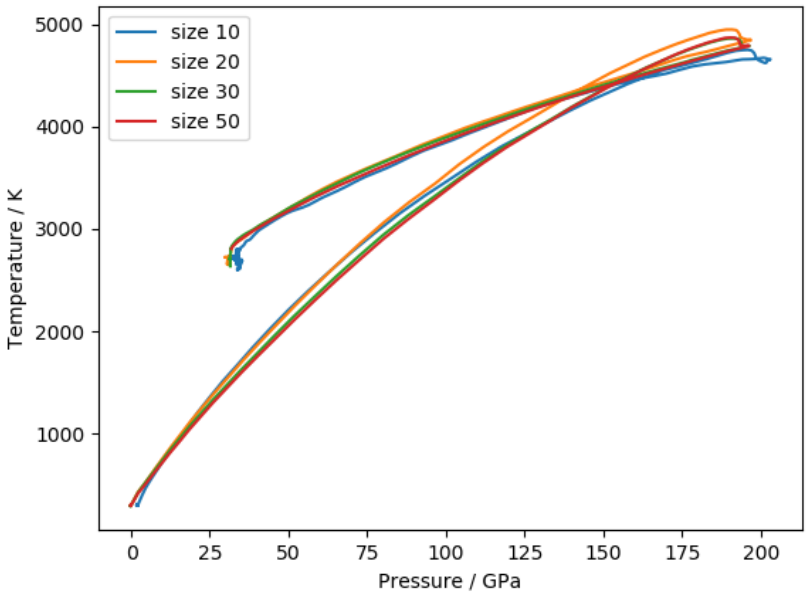

Figure 4.12: Simulations with x and y dimensions of 10, 20, 30 and 50 unit cells were run (the z dimension remained constant with 100 unit cells). Other than size, all conditions were the same. They each followed the same pressure temperature profile, starting at 0 GPa and 300K, being shocked to 200 GPa, and then released.

The centro symmetry parameter (CSP) is plotted against temperature in figure 4.13, to compare the onset of melt for different box sizes. When shocked, the CSP and temperature increase almost linearly, then on release the temperature decreases rapidly and the CSP increases when melting occurs. This point is at a similar temperature for all box sizes, so having a small box is not suppressing the onset of melt.

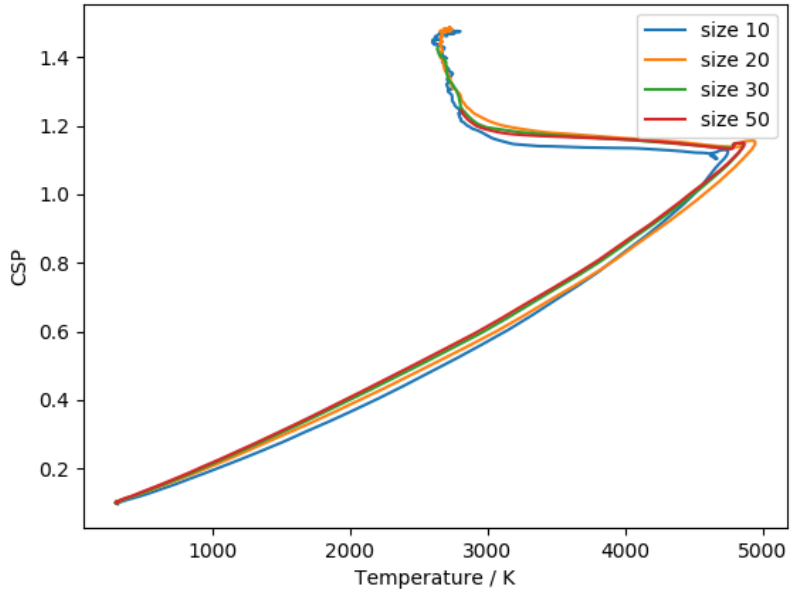

Figure 4.13: The dimensionless centro symmetry parameter (CSP) is plotted against temperature for different box sizes, and these all produce similar pathways. CSP and temperature increase during the shock, then there is a sudden drop in temperature on release, while CSP increases on melting. The box size is given in the legend: the x and y dimensions were 10, 20, 30 and 50 unit cells (the z dimension was always 100 unit cells)

4.3 Results

Physical tamper materials (Cu, Al, Sn, Si, Zn and Au) were modelled, with Cu as the bulk material, to confirm that the release pressures were as expected. Subsequent results in section 4.6 used artificial tampers.

For a Cu tamper, there would not be a boundary between the bulk and the tamper and there should be no release wave as $u_R = u_P$. This is shown to be the case for the pressure profile in figure 4.14.

Shock impedance was used to check the validity of the simulations for Al, Sn, Si, Zn and Au tampers. Shock impedance, Z, is given by

$$Z = \rho U_s \tag{4.9}$$

where U_s is the shock velocity and ρ is density. It would be expected that modelling of the tamper material would produce the reflected pressure, P_r, compared to the incident pressure, P_i, of

$$\frac{P_r}{P_i} = \frac{Z_2 - Z_1}{Z_2 + Z_1} \tag{4.10}$$

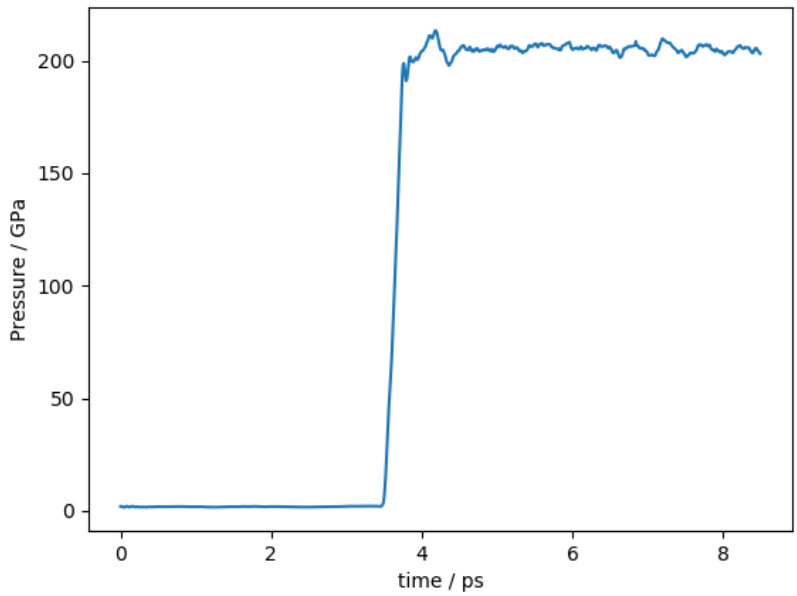

Figure 4.14: With a Cu tamper there is no release wave, as expected. There is some disturbance at 4.2 ps when the shock wave reaches the tamper.

where Z_2 is the tamper shock impedance and Z_1 is the shock impedance of the bulk material.

Figures 4.15 to 4.17 show the pressure profiles of various tampers, with the predicted pressure values given as horizontal lines overlaying the LAMMPS data. They also include the predicted release pressure given by the mirror image method, which would be expected to be consistent with the LAMMPS data, as it was by this method that the LAMMPS tamper velocity was calculated.

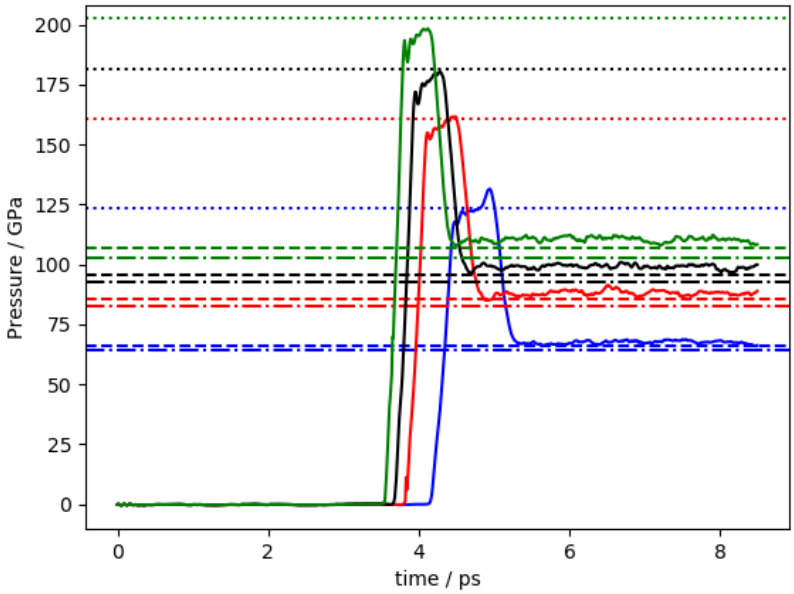

Figure 4.15: The pressure profile for an Al tamper with different piston velocities, each a different colour. The dotted line is the predicted shocked pressure, the dashed line shows the release pressure predicted from the mirror image method, and the dash-dotted line gives the release pressure calculated from impedance.

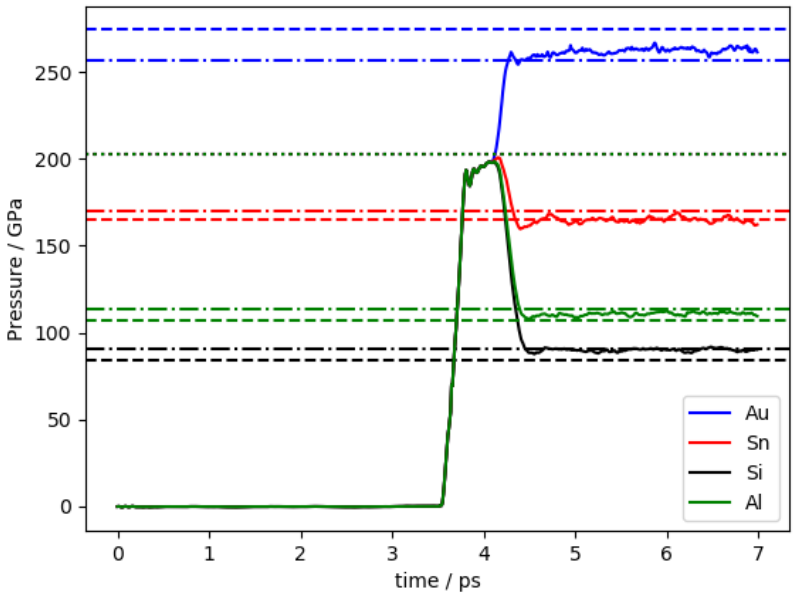

Figure 4.16: The pressure profile for four tamper materials (given in the legend) with the same piston velocity. As in figure 4.15, the dotted line is the predicted shocked pressure (which is the same for all of the tampers), the dashed line shows the release pressure predicted from the mirror image method, and the dash-dotted line gives the release pressure calculated from impedance. Au has a greater impedance than Cu, so the pressure increases.

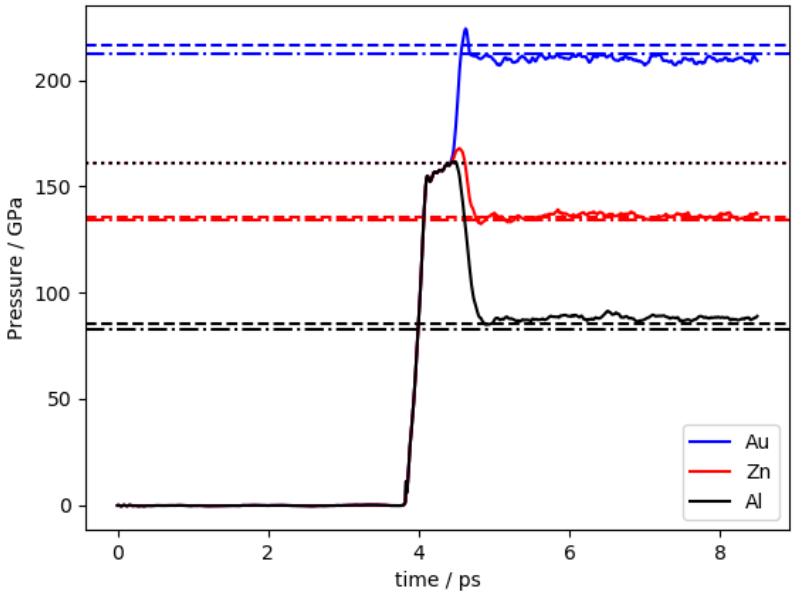

Figure 4.17: The pressure profile for three tamper materials (given in the legend) with a different piston velocity to figure 4.16. As in figure 4.15, the dotted line is the predicted shocked pressure, the dashed line shows the release pressure predicted from the mirror image method, and the dash-dotted line gives the release pressure calculated from impedance.

4.4 Discussion

The combined results of figures 4.15 to 4.17 are given in figure 4.18. It is shown that, within an error of about 5%, the mirror image pressure (equations 4.4 to 4.7) is in agreement with the impedance result from equation 4.10, and the LAMMPS simulation, which is using the mirror image method, is behaving as expected. Both methods of calculating pressure have some values above and some below the LAMMPS pressure, suggesting there is not a systematic error in the LAMMPS set up. The two largest errors of the mirror image pressure are for the ringing up with the Au tamper, and as the main use of this method is to decrease pressure, the relevant results are within a 5% error range.

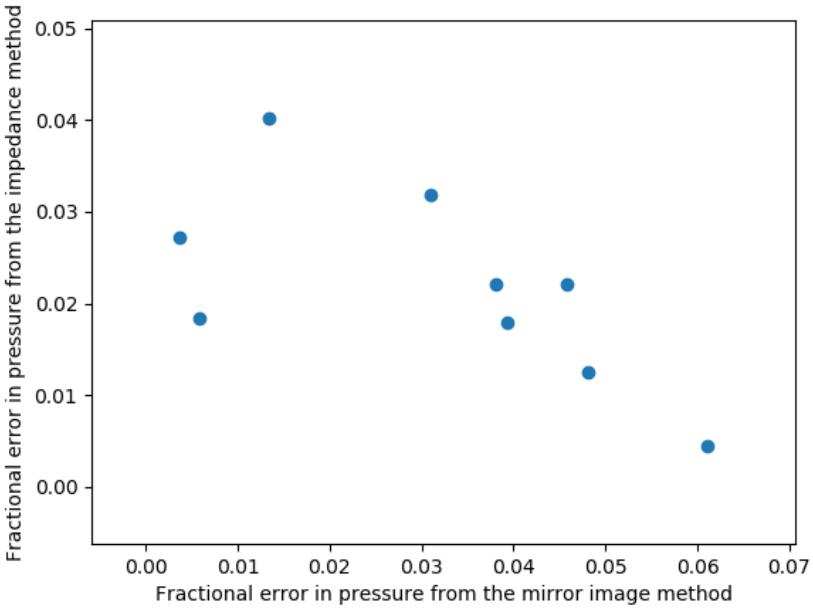

Figure 4.18: For each of the release pressures found in figures 4.15 to 4.17, the error in the pressure calculated from the impedance method is plotted against that of the mirror method. In both cases the fractional error is given relative to the LAMMPS data.

From this low error, it can be concluded that using only a thin wall to model the tamper was sufficiently accurate, reducing the computational requirements and meaning that a potential for the tamper material is not needed. This method has been used in the second part of the chapter, but would also have wider applications as these factors have prevented the modelling of tampers in other research [54].

These simulations were carried out for the test tamper materials of Cu, Al, Sn, Si, Zn and Au. The Cu tamper confirmed the limiting case in which there was no release wave, so the particle velocity on release was the same as the particle velocity

in the shock wave. The tampers produced release velocities which were a factor of 1 to 1.5 greater than the shock particle velocity. The range used for the rest of the simulations was 1.6 to 2 in order to cross the melt curve. Values this high could be achieved experimentally by using tamper materials with a shock impedance which is much less than that of Cu, such as polymers (epoxy would increase the velocity on release by a factor of about 1.7 and polystyrene 1.9).

Part 2: The effect of cooling rate on melting

4.5 Method

4.5.1 Defining melting

As in Chapter 3, the centro symmetry parameter (CSP) was used to define when melting occurred. CSP is volume dependent, so changed as the release wave passed through the output region, in addition to increasing due to melting. To account for this, a unitless CSP was used, calculated by dividing by area to obtain a dimensionless value. There is an initial large increase in the unitless CSP due to the shock wave, with any further increase after this corresponding to melting.

Figures 4.19 and 4.20 give examples of CSP profiles. For the release rate used in figure 4.19, melting only occurs on release in the slice closest to the tamper, due to the dissipation of the release wave as it travels back along the z direction. This is the output slice which is shown in figure 4.1 and is used to obtain the results. There is an increase in CSP in slice 5 at the end of the simulation time; this is due to growth of the melt near the tamper rather than nucleation of melt in this region.

For figure 4.20, the initial shock has gone above the melt curve. Slices 2 to 5 display a delayed onset of melting from the initial shock, rather than on release. Slice 1 is an outlier because of its proximity to the piston. At lower shock pressures, the absence of this trend means that melting must be on release rather than being caused directly by the shock. This is an important step to check, as it was seen in figure 4.11 that the shock Hugoniot continues past the static melt curve before melting occurs.

The standard deviation of the CSP peaks during melting, and then decreases as all the material becomes a liquid. This could be used to ensure that melting was completed on release, because if the release wave only disordered the solid, then the increase in standard deviation would remain high. An example of the CSP standard deviation showing melting, from release with different tampers at the highest shocked

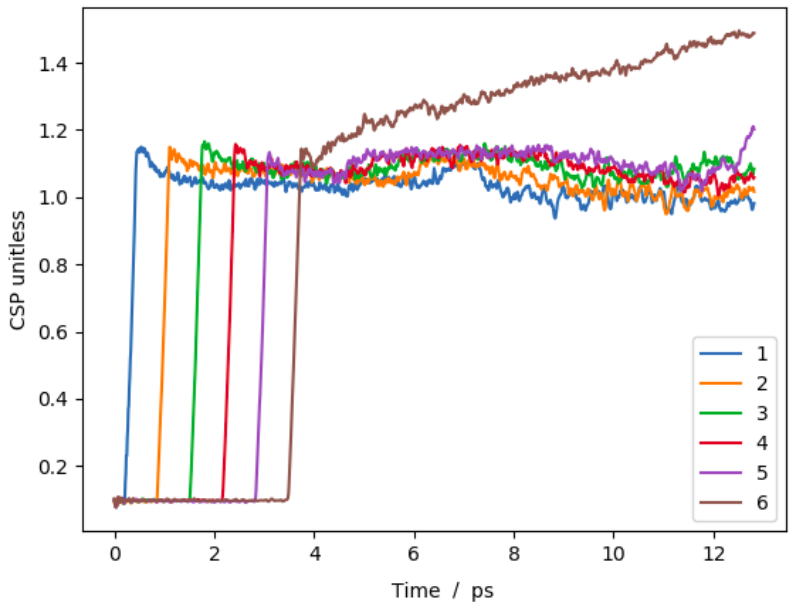

Figure 4.19: Unitless CSP was used to define melting. The graph shows CSP against time for different slices, 5 unit cells wide, equally spread along the z direction. Melting at this release rate, shown by an increase in CSP, only occurs in output 6, which is closest to the tamper (with a position of 85 to 90 unit cells as shown in figure 4.1).

pressure, is given in figure 4.21.

The rate of temperature change, as well as the temperature and pressure at which melting begins, is needed to calculate the static melting point. The temperature gradient for one simulation is given for all slices along the z direction in figure 4.22. The initial positive peak shows the passage of the shock wave, and the smaller, broader trough is from the release wave. The minimum value of the trough is taken as the rate of temperature change. While the temperature gradient of the shock wave remains roughly constant as it moves along the z direction, the release wave clearly dissipates, as the troughs decrease in amplitude and become broader. The exception to this is slice 1, which is affected by the release wave reaching the piston.

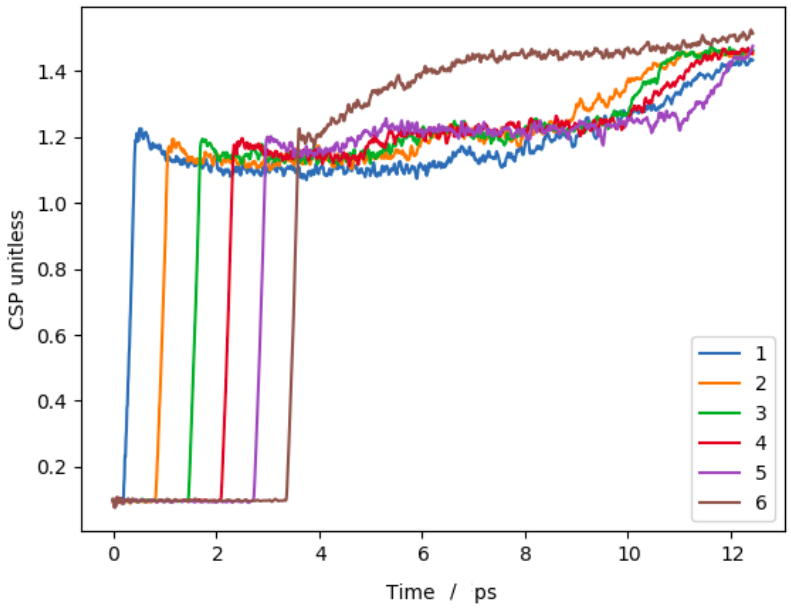

Figure 4.20: When shocked above the melt temperature, slice 6 melts on release. The other slices only melt later, when sufficient time has passed after the initial shock wave, rather than as a result of release.

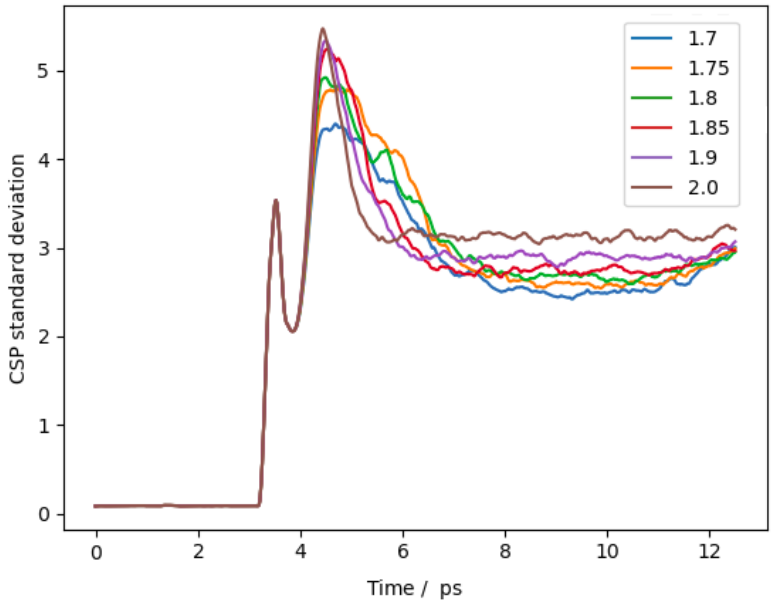

Figure 4.21: The profile of the standard deviation of CSP from slice 6 with different tampers. The first peak is due to the shock wave, the second peak is on release for different tampers (with velocity of the tamper as a fraction of piston velocity given in the legend). Each tamper results in melting, as the standard deviation drops to a constant value.

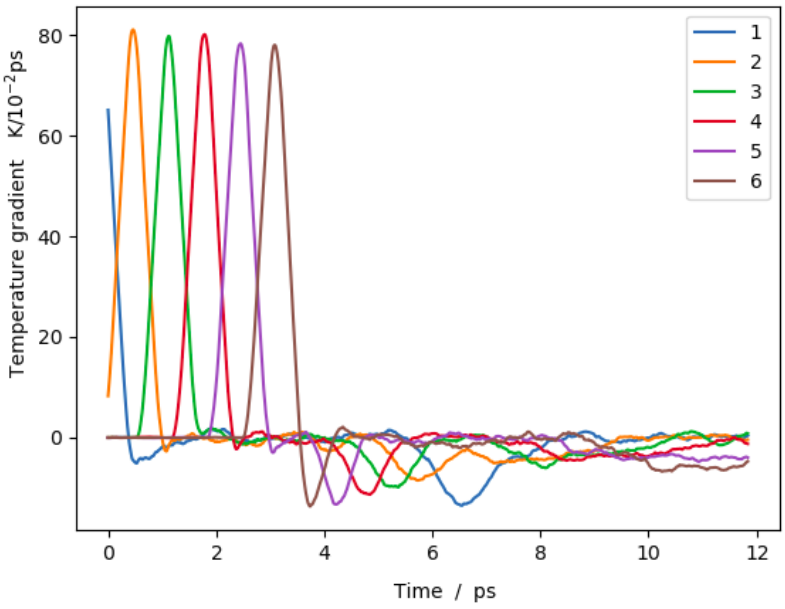

Figure 4.22: In order to define the rate of temperature change, a graph of the temperature gradient was produced. This is shown for 6 slices along the z direction, with output 6 closest to the tamper. The initial positive temperature gradient is caused by the shock wave and the lower amplitude trough is from the release wave.

4.5.2 Fitting temperature and pressure

The change in cooling rate on release was produced by using different tampers. Temperature at melting is related to the static melt temperature and the rate of temperature change by the power law relationship given in equation 4.11 [42].

$$T_D = T_S + B\beta^z \tag{4.11}$$

T_D and T_S are the dynamic and static melt temperatures, β is the rate of temperature change, and B and z are constants. This same relationship is assumed to also hold for pressure, P, but with different constants.

$$P_D = P_S + A\beta^y \tag{4.12}$$

Six initial shocked pressures were used, with around eight tampers each. The fitting was carried out for every initial pressure. An example is given for the maximum shocked pressure of 200 GPa in figures 4.23 and 4.24, for temperature and pressure respectively.

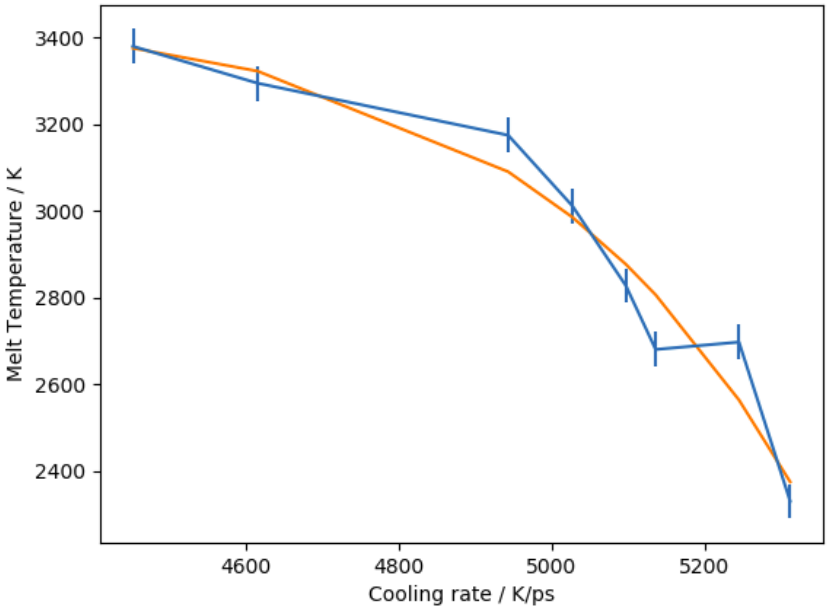

Figure 4.23: Using equation 4.11 to plot dynamic melt temperature against cooling rate. The fitted curve is orange. The error bars are from the noise in temperature at the point of melting; the error due to this noise is much greater than the uncertainty as to what time the melt occurs.

For each tamper, the release path in pressure and temperature was the same for each starting pressure. The static melting point predicted using this fitting method was confirmed to lie on the release path. An example is shown in figure 4.25, which

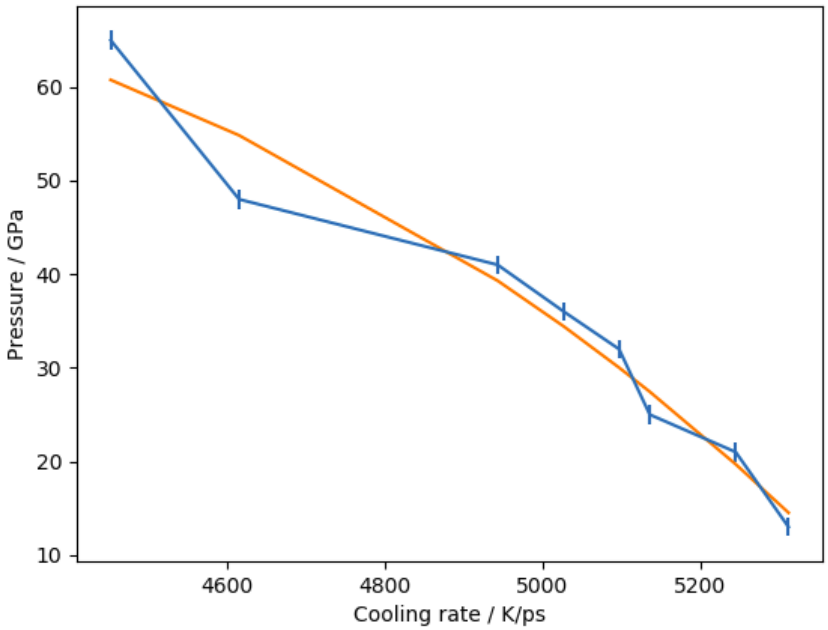

Figure 4.24: Fitting pressure to cooling rate using the assumed power law relationship equation, 4.12, with the fit shown in orange for the blue data points. The error in pressure at melting is from the uncertainty in the time at which melt occurs.

includes the dynamic melting points and the predicted static melting point (blue and orange circles) as well as the release path (red) and the power law fit (green). The predicted static melting point agrees with the literature melt curve [57]. The release path shows fluctuations in temperature, which were the cause of the error bars in figure 4.23. These fluctuations were due to only 500 atoms being used in the slice along the z direction.

The process was repeated with different shocked pressures in the range 150 to 200 GPa. This pressure range was used as the release paths from these points on the Hugoniot cross the melt curve.

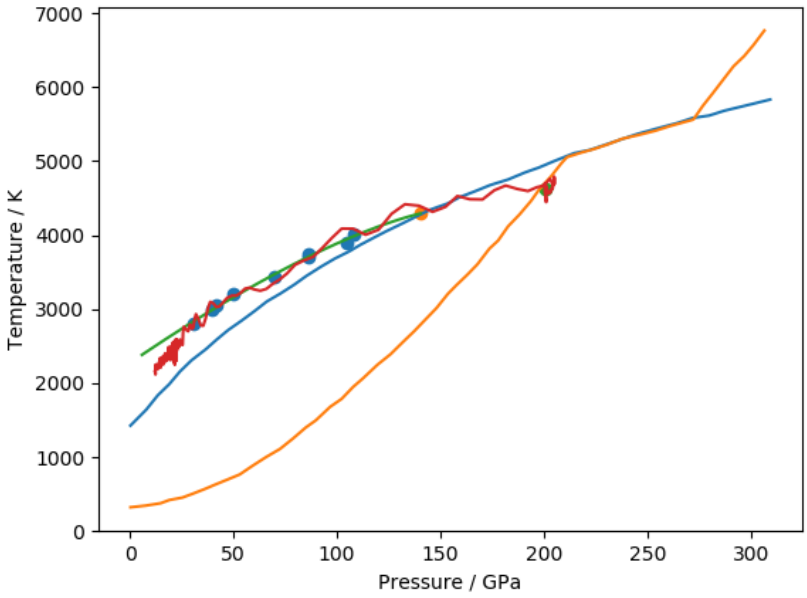

Figure 4.25: For one example of shocked pressure, the melting points for each tamper (blue circles) are shown. The fitted power law is green, and the static melting point predicted from this is the orange circle. This lies on the literature melt curve (blue). The longest release path (red), shows that all melting points and the extrapolated static melting point lie on the same release path. This path starts at the shocked pressure, which lies on the literature Hugoniot (orange).

4.6 Results

4.6.1 Predicted melt curve

The main result of this chapter is given in figure 4.26. All except one of the predicted static melt temperatures, obtained by fitting power law equations to the dynamic melting points, agree with the literature melt curve within the error margins.

Due to the melt being found on release, the melting points were limited to the pressure range of 50 to 110 GPa. Below 50 GPa, the full range of release rates did not cross the melt curve. Above 110 GPa, the initial shocked pressure was close to the melt curve, so the upper limit was set to ensure that all melting came from the release wave rather than the shock. This range is shown in figure 4.27. As can be seen in this graph, while there is clear agreement with the literature melt curve, the error bars are large, especially in pressure. These were calculated from the uncertainty in fitting the power law function, as this was the dominant source of error. For the two largest errors in pressure, the calculated static melting points are close to the literature value, so this uncertainty may have been overestimated. By comparison, the uncertainties in temperature and pressure at the time of melting, shown in the error bars of figures 4.23 and 4.24, were an order of magnitude smaller.

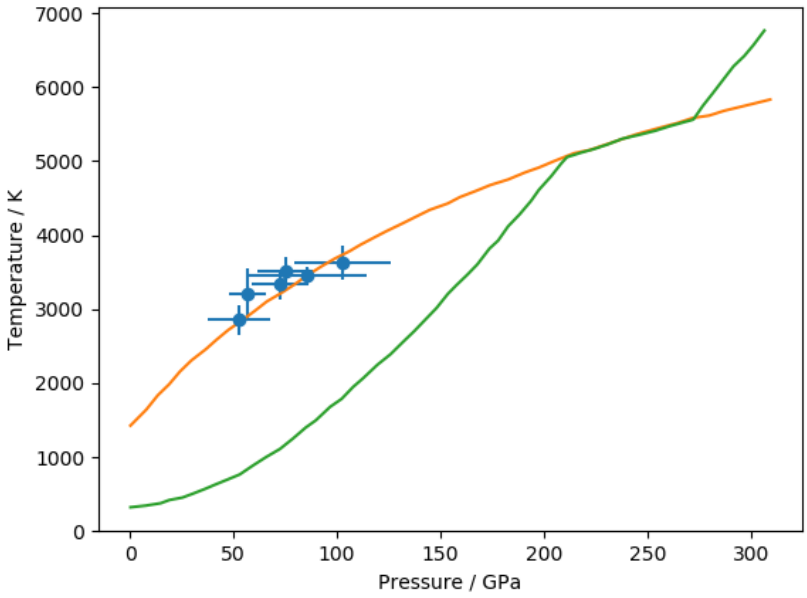

Figure 4.26: Predicted static melting points of Cu (blue) compared to the literature melt curve (orange). The error bars are calculated from the uncertainty in fitting the power law function to pressure and temperature, and are generally larger for pressure. The calculated values for temperature and pressure correspond well with the literature values [57].

The calculated melting points were fitted with a polynomial to form a melt curve in figure 4.28. It is weighted by the uncertainty in each point and includes the ambient melting temperature as the value at close to 0 GPa. Although individually these melting points match the literature results, the fit through all of them becomes too shallow at about 100 GPa, so could not be used to extrapolate the melt curve to higher pressures.

Despite the limited pressure range and large error bars, the calculated static melting points do reproduce the literature melt curve, unlike the dynamic results which had large overshoots of up to 1000 K and 50 GPa at the highest cooling rates used, as shown in figures 4.23 and 4.24.

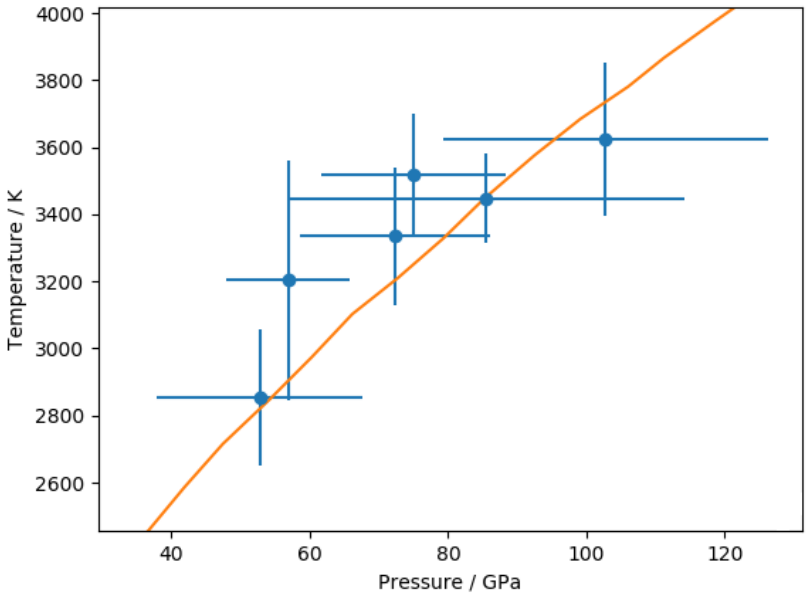

Figure 4.27: An enlarged section of figure 4.26 showing the relevant pressure range of 40 to 120 GPa. Five of the six static melting points agree with the literature melt curve within the error bars.

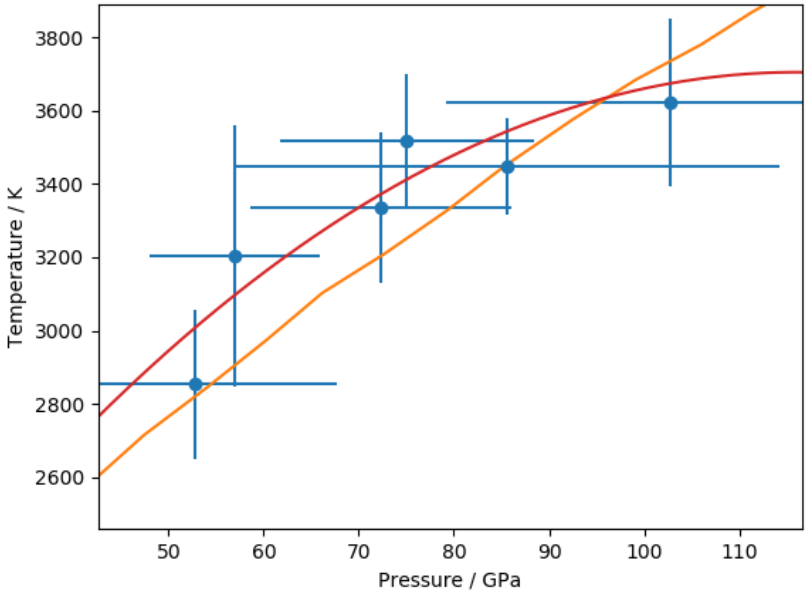

Figure 4.28: Fitting a polynomial (red line) to the obtained melting points (blue). This is compared to the literature melt curve in orange. The fit is weighted by the error bars in pressure and temperature, and the ambient melting point is also used in the fit.

4.6.2 The coexistence method

The melting points found using the coexistence method are shown in figure 4.29. The error bars indicate the uncertainty as to whether the liquid region is staying the same size over the length of the simulation. Running simulations for longer and at more frequent intervals in temperature may reduce this uncertainty. This graph shows that, for the pressure range of 10 to 100 GPa, the coexistence method reproduces literature values within error. The potential used in this chapter must therefore be valid, and the close agreement suggests that the literature data can be accepted as the true value of melt temperature for comparison with the melt curve obtained using the tamper method.

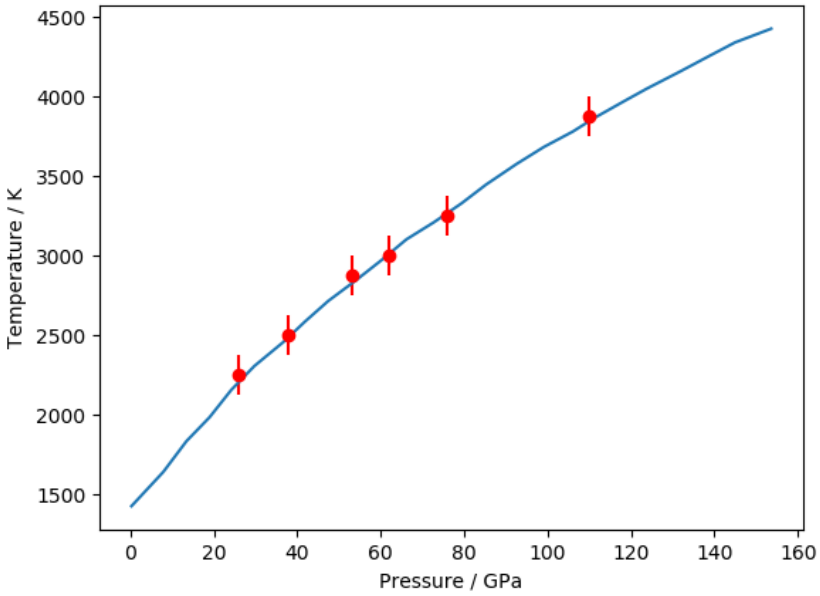

Figure 4.29: Melting points for Cu obtained using the coexistence method (red) correspond to the literature melt temperature (blue) [57] within error, in the pressure range 10 to 100 GPa.

4.7 Discussion

4.7.1 Predicted melting points

The literature melt curve for Cu is matched by the calculated static melting points, with a 7% uncertainty in temperature. This was obtained over a 60 GPa pressure range, a substantial part of the melt curve before the Hugoniot. Each point is the result of about 8 dynamic simulations. Using different velocity seeds in the LAMMPS script did not affect the results, and the error in determining onset of melt was small compared with the uncertainty in fitting a power law to the

melt temperatures and pressures against cooling rate. These fitting errors may be overestimated, and there are potential methods for reducing them, by finding static pressure using a different technique.

4.7.2 The power law fit

The large error bars for the calculated melting points, shown in figure 4.26, are due to the uncertainty in fitting equation 4.12 to the dynamic melting pressures. It was thought that this may have been because the assumption that the relationship for temperature against cooling rate could also be used for pressure was incorrect. To check, an exponential fit was applied to pressure against cooling rate, to see if this gave a more precise fit to the literature melt curve than the power law. This is shown in figure 4.30, where it can be seen that it did not lead to an improvement. Error bars are similarly large, and the melting points are less accurate when compared to the literature.

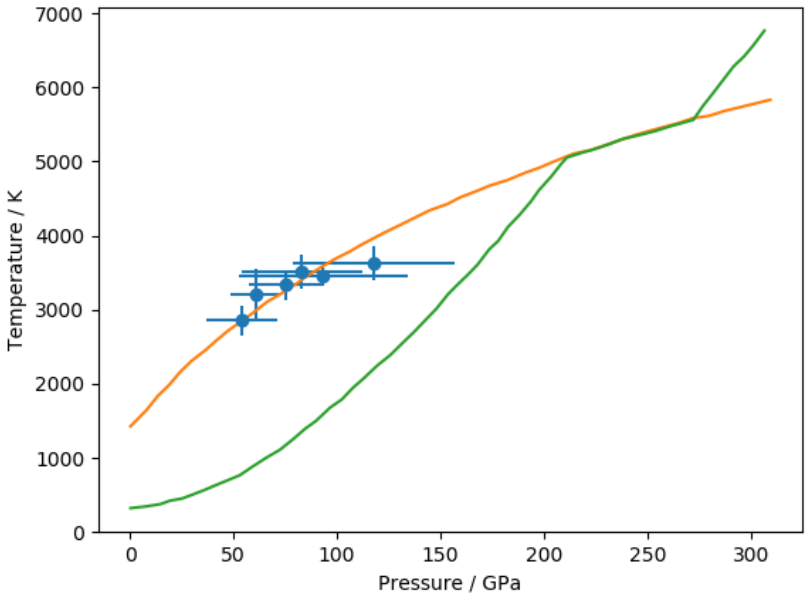

Figure 4.30: Testing an exponential fit to pressure against cooling rate, rather than a power law. Some pressures remain similar, but one is much further from the literature melt curve, and all except one of the error bars are larger.

A different approach was to use the power law fit for temperature only, and find the pressure from the temperature-pressure release path. This reduced the pressure error bars to about the same size as the uncertainty in temperature. The results are shown in figure 4.31. Despite the slightly smaller error bars, the accuracy of the melting points compared to the literature value is similar to that of the power law method. However, it would not be possible to use this technique with experimental

rather than computational data.

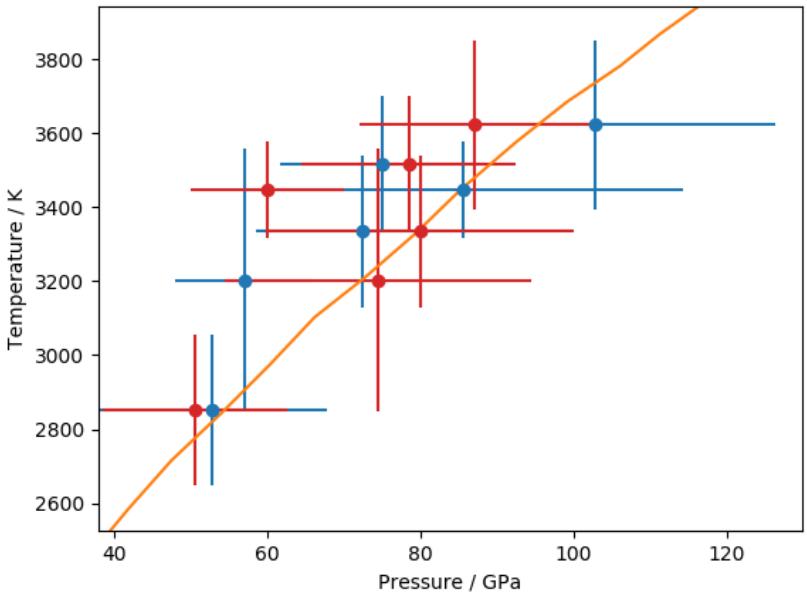

Figure 4.31: Comparison of the predicted melt points found by fitting temperature and pressure (blue) and just temperature (red). The literature melt curve is in orange.

An issue which exacerbates the problem of the large error bars is that only a relatively small pressure range is available to study. This is due to the conditions of melting on release; shocking in the range of 150 to 200 GPa for Cu corresponds to the release path crossing the melt curve at 50 to 110 GPa. An option would be to use multiple shocks to release from an off Hugoniot position, but this would be experimentally challenging, limiting its use, and is beyond the scope of this thesis.

4.7.3 Experimental applications

Experiments using X-ray diffraction have previously been carried out to monitor melt on release from a laser shock in dynamic conditions, but did not account for kinetic effects [32]. In this chapter, simulations of different tamper materials have allowed the release rate to be changed, making the static melt temperature obtainable from a dynamic system by utilising the power law fit method. To repeat this experimentally, the temperature and pressure of the melting point would need to be found for several tampers from each shock pressure.

While there are limitations to this method at present, such as the large error bars produced, and the restricted pressure range available from release off the Hugoniot, it has the potential to open up a new laser shock technique, with the aim of finding

static melt curves experimentally for materials which do not have a known equation of state.

4.8 Conclusion

Using LAMMPS to model a shock and release experiment with multiple tampers proved to be a successful method of obtaining the static melt curve for Cu, in the pressure range 50 to 110 GPa, from dynamic data. The melt curve predicted agreed, within error bars, with the literature melt curve and the coexistence method.

The tamper was modelled as a thin slice of material forming a wall which did not interact with the bulk material and, when the shock wave reached it, moved at a velocity determined by the tamper's shock impedance in order to send a release wave back through the bulk. Although most of the simulations were carried out using artificial tampers to give a range of cooling rates, initially physical tamper materials (Al, Sn, Si, Zn and Au) were tested to ensure that the tamper modelling method produced the expected pressure on release. It was found to be accurate within a 5% error. These metals were test materials: for a Cu target, a lower impedance tamper, such as a polymer, would be required to give the appropriate release pressure experimentally.

This novel method of modelling a tamper greatly reduces the computational cost, as the full length of the tamper is not included, and means that a potential for the tamper material is not required. It will therefore also have applications in other research areas, as tampers are often neglected from MD simulations due to these limitations [54].

As in Chapter 3, melting was defined using the centro symmetry parameter (CSP). However, to account for the change in volume caused by the shock and release waves, this was made to be dimensionless. The standard deviation of the CSP for a slice of material, as well as its mean value, also gave ways of determining melt, as a result of the distribution of CSP in solids and liquids.

The different tampers altered the cooling rate of the material on release, but did not change the release path. The power law relationship between the rates of temperature change and the dynamic melting points was fitted, for each shocked pressure, and the static melting point obtained. This point also lay on the release path and, within error bars in pressure and temperature, agreed with both the literature melt curve and the coexistence method.

The limitations of this method come from the large uncertainty in fitting the power law relationship to pressure and the restricted pressure range of the melt curve available on release. Together this means that, although the individual static melting points lie on the literature melt curve within their error bars, they cannot be used to accurately extrapolate to higher pressures. The pressure range was limited by the release paths from the Hugoniot which cross the melt curve. If the method was applied to materials other than Cu, or if an alternative compression path was used, then the range would be different.

Experimental applications for this method could be designed based on existing laser shock experiments, with an X-ray diffraction diagnostic to find the dynamic melting points. Artificial tamper materials were used in the simulations, but physical tamper materials could be found in order to carry this out.

The primary aim of this chapter was to develop a method for calculating the static melt temperature on release from a shock, and this was achieved with an uncertainty of about 7%. This means that dynamic temperatures obtained in a shock experiment could now be used to predict a static result.

Chapter 5

Conclusion

5.1 Motivation

The primary aim of this thesis was to investigate, using molecular dynamics (MD), the effect of kinetics on the melt temperature, in order to produce a method for determining the static melt temperature in dynamic situations. A model for converting dynamic melt measurements into static values is needed because of the large discrepancy in timescales for the rate of temperature change between high pressure systems and the experimental methods of reaching them.

Additional benefits of the melt model created in Chapter 3 include a reduction in the computational cost of finding the static melt temperature in MD by two orders of magnitude when compared with the established coexistence method, along with a means of accessing other kinetic variables, and of predicting the temperature of melting for any given heating rate.

To link this melt model to dynamic experiments, a method of simulating the release from a tamper was developed in Chapter 4. The tamper is often omitted from MD simulations as conventionally it requires additional potentials and increases the computational costs significantly, so this new method will have applications beyond the one presented here.

5.2 Summary of methods and results

Two novel methods were produced in this thesis. The first was a numerical model to fit to the z shaped temperature profile of a rapidly melting block of material, in order to find the temperature at which melting began for a range of heating rates. The second was a new approach to modelling a tamper to control the cooling rate of the release wave, and from this predict the static melting point.

5.2.1 Numerical melt model

In LAMMPS, thermal energy was added to a cube of material at a constant rate, for a range of pressures and heating rates. The temperature profile was tracked and the centro symmetry parameter (CSP) was used to find the onset of melting. The rapid nature of the heating meant that equilibrium was not achieved, and so the temperature profile formed a z shape.

Initial analysis focused on the peak and the trough of the z profile. They were both found to increase with heating rate and were linear with pressure. A linear fit was applied to the graph of trough temperature against heating rate, to estimate the static melt temperature. This was about 5% lower than the literature value, but had no physical basis as the melt temperatures did not converge at low heating rates.

To improve upon this estimate, a numerical melt model was developed to fit to the z profile, and from that the static melt temperature at which melting began for all heating rates could be found. At each time step, the temperature was increased according to the LAMMPS heating rate. The amount of melt growth and nucleation was calculated and used to adjust the volume of liquid present. The temperature was then decreased due to loss of thermal energy through latent heat for any melting occurring in that time step.

This method provided a good match to the MD data, despite using a simple melt model. For high heating rates of 600-1200 K/ps, the static melt temperature found using the model was accurate and constant with rate.

In the pressure range of 0 to 10 GPa, the literature Cu melt curve was reproduced using the numerical model, with errors in temperature of about 1%, making this method very successful at these pressures. It was also in agreement with the coexistence method, which is an established technique for finding the melt temperature in MD. For pressures of 20-30 GPa, the z profiles became too steep for the numerical model to fit closely, and as a result the predicted static melt temperatures were less accurate.

The simulations were also carried out using Ta, and were found to be just as reliable over 0-10 GPa as Cu, when compared to the literature melt curve. Cu and Ta are FCC and BCC metals respectively, which implies that the method would be applicable for other simple metals.

The numerical model's computational requirements were reduced by two orders of magnitude, compared with the coexistence method. Additionally, the latent heat of

fusion and specific heat capacity could be found from these simulations. However, the most significant consequence of this method is that by accurately finding the static melt temperature from dynamic melting, it could be applied to laser shock experiments.

5.2.2 Modelling a tamper

The tamper was modelled in LAMMPS as a thin slice of material forming a wall which did not interact with the bulk material. When the shock wave, caused by a constant velocity piston, approached the tamper, it began to move; the time at which it started was determined using the mean velocity in the pretamper regions. The tamper velocity formed a step function when plotted against time.

The required tamper velocity was found using the established mirror image method of plotting the pressure-particle velocity profiles for the bulk and tamper materials, and reflecting the bulk profile about a given particle velocity to find the release velocity at the intersection. This was carried out using profiles from the Rusbank database [68], but could alternatively have been calculated from the constants S and c_0 which link particle and shock velocity.

Five physical tamper materials were investigated (with Cu as the bulk material) at several shock velocities, to check that the tamper modelling method matched the pressures on release which had been calculated using the shock impedances of the tamper and bulk materials. All results fell within a 5% error. Subsequently artificial tamper impedances were used to produce a range of release rates for analysis.

Melt was observed to occur in the bulk material after the passage of the release wave, as the decrease in temperature and pressure caused the material to cross the melt curve. The onset of melt was defined by examining the CSP, corrected to account for the change in volume. Measurements were taken from thin slices of the model, to increase precision and ensure melting was caused by the release wave, rather than the initial shock wave.

For each shocked pressure, a power law relationship was fitted for the temperature or pressure at melt with the rate of temperature change, to find the static melting point extrapolated at a cooling rate of zero. The tampers all followed the same pressure-temperature release path (but had different final positions along the curve), and the static melting point obtained from fitting the power laws also lay on this path.

Simulations were carried out, using Cu as the bulk target material, to obtain static melt temperatures at pressures between 50 and 110 GPa. This was the full pressure range for which melt occurred on release. Within error bars (of around 7% in temperature), these values agreed with the melt curves both from the literature and formed using the coexistence method.

The largest source of error came from the uncertainty in fitting the power law function to pressure. An alternative fitting function may be preferable, and this could be the focus of any further work to improve the accuracy of the method.

5.3 Further work

The numerical melt model was successful in establishing the static melt temperature from dynamic measurements, but there is potential for including more kinetic components in the model. This would improve the accuracy at higher pressures, and mean it could be used to obtain additional information, such as energy barriers.

The numerical method could also be expanded to incorporate cooling. Cooling temperature profiles lack the prominent z shape, but fitting a numerical model to estimate the amount of melt may be possible. This would link directly to the tamper model, and provide a further method of finding the static melting point from dynamic simulations.

The power law equation used in Chapter 4 proved to be a good fit for temperature against cooling rate, but caused large uncertainties for pressure. This was the greatest source of error in the method, so other attempts at optimisation would be negligible without addressing this first, possibly by using an alternative relationship. Within this thesis, an exponential fit was tried with no improvement, and while finding the pressure from the temperature did reduce the error, it does not have an experimental equivalent.

The range of pressures available for release after a shock is limited by the position of the Hugoniot relative to the release pathway and the melt curve. Compressing to a different point of pressure and temperature would allow more of the melt curve to be explored. This could be achieved using multiple shocks or a ramped shock to reach a compression state off the Hugoniot, but it would be difficult to do this experimentally and still have the desired release response from the tamper.

For both methods developed, further test materials should be used, as only Cu and Ta have been studied so far. Before carrying out a shock and release experiment,

target materials could be investigated which would have the maximum amount of melt curve accessible by release from the Hugoniot, to fully utilise the tamper method. Further optimisation would also be achieved if a suitable high impedance bulk metal could be found, as that would give a greater range of release rates available from the tampers.

5.4 Experimental applications

High power lasers are used for shock compression, and may produce melt either during the shock, or on release. The heating rate of the shock is determined by the laser parameters, and cooling rate can be altered by the choice of tamper material. As has been shown in this thesis, carrying out dynamic experiments at a range of rates gives melting points from which the static melt curve of the target material can be calculated.

Artificial tampers were modelled in Chapter 4, but physical materials could be used with the same effect. The ideal tamper materials would depend on the bulk target. For Cu, low impedance materials such as polymers or certain metals (for example Al) would ensure the release wave crossed the melt curve; if a higher impedance target was chosen then more metals would be suitable options for the tamper.

The onset of melt can be determined by X-ray diffraction (as the liquid diffraction signal is broader and of lower intensity than a solid signal), and as the position of the diffraction peaks gives the strain, the temperature and pressure can be inferred. X-ray diffraction has been used previously to find melt on release [32], but without applying different rates of temperature change to check for kinetic effects affecting the position of the melt curve. The proposed experiment would be repeated with different tamper materials, to utilise a range of release rates and thus allow the static melt curve to be generated.

Two laser beams are needed to do this: one to drive the shock, and the other to produce X-rays. X-ray Free Electron Lasers (XFELs), for example LCLS, have previously been required to image liquid diffraction, due to its low intensity compared with crystal diffraction. However new imaging techniques, such as Single Photon Energy Dispersive X-ray Diffraction (SPEDX) [69], can detect lower intensity signals, making them a feasible diagnostic for experiments carried out in UK laser facilities (e.g. Gemini at the Rutherford Appleton Laboratory) without an XFEL, if integrated over several shots.

One difficulty of applying this method experimentally is obtaining independent pressure and temperature measurements. Diffraction finds the spacing between atoms, so gives density. From density, for points on a known Hugoniot, pressure and temperature can be calculated. Away from the Hugoniot, or when the material does not have a known equation of state, another method for determining pressure and temperature is needed. VISAR (Velocity Interferometry System for Any Reflector) could be used to calculate pressure, but temperature is harder to measure independently. With several diffraction peaks visible, the relative intensities of the peaks are affected by the Debye-Waller effect, in theory meaning temperature could be extracted directly from XRD. In practice, this method would be imprecise because of the large error in the Debye temperature and uncertainties in intensity caused by texture of the target. Other alternatives include Extended X-ray Absorption Fine Structure (EXAFS), Streaked Optical Pyrometry (SOP), Raman Scattering and Neutron Resonance Spectroscopy (NRS). However, all of these methods have limited applications (due to requiring transparent materials or certain pressure ranges) or large errors.

In addition to a melt on release experiment, the novel impedance method of modelling tampers could be applied to other research areas. Previous experiments using tampers have shown a discrepancy between experimental and modelled results, as the tamper has been omitted from simulations due to difficulties which this method would overcome [54].

5.5 Conclusion

This thesis has investigated MD simulations for dynamic melting. In doing so, two techniques have been developed: a numerical model to track melt at high heating rates and a method for modelling a tamper in MD. Combined, these show how laser shock and release experiments could be carried out in order to obtain static melt curves at high pressures.

The tamper method also has wider applications, as it allows release to be modelled accurately, without the need for a potential of the tamper material. Both methods have the additional advantage of significantly reducing the computational cost of the MD simulations, compared with established techniques.

Bibliography

[1] L. Dubrovinsky, N. Dubrovinskaia, V. B. Prakapenka and A. M. Abakumov. Implementation of micro-ball nano diamond anvils for high-pressure studies above 6 Mbar. *Nature Communications*, 3:1163, 2012.

[2] W. A. Bassett. Diamond anvil cell, 50th birthday. *High Pressure Research*, 29(2):163, 2009.

[3] L. Dubrovinsky, N. Dubrovinskaia, E. Bykova, M. Bykov, V. Prakapenka, C. Prescher, K. Glazyrin, H.-P. Liermann, M. Hanfland, M. Ekholm, Q. Feng, L. V. Pourovskii, M. I. Katsnelson, J. M. Wills and I. A. Abrikosov. The most incompressible metal osmium at static pressures above 750 gigapascals. *Nature*, 525:226, 2015.

[4] A. Jayaraman. Diamond anvil cell and high-pressure physical investigations. *Reviews of Modern Physics*, 55(1):67, 1983.

[5] M. J. Schmitt, R. A. Kopp, D. S. Moore and S. D. McGrane. Analysis of laser-driven shocks in confined and unconfined geometries. *AIP Conference Proceedings*, 706:1409, 2004.

[6] D. Batani, H. Stabile, A. Ravasio, G. Lucchini, F. Strati, T. Desai, J. Ullschmied, E. Krousky, J. Skala, L. Juha, B. Kralikova, M. Pfeifer, C. Kadlec, T. Mocek, A. Präg, H. Nishimura and Y. Ochi. Ablation pressure scaling at short laser wavelength. *Physical Review E*, 68(6):067403, 2003.

[7] D. Grady. Physics of shock and impact, Volume 1: fundamentals and dynamic failure. page 20, 2017.

[8] Q. An, S. N. Luo, L. B. Han, L. Zheng and O. Tschauner. Melting of Cu under hydrostatic and shock waveloading to high pressures. *Journal of Physics: Condensed Matter*, 20:095220, 2008.

[9] D. Grady. Physics of shock and impact, Volume 1: fundamentals and dynamic failure. pages 6–7, 2017.

[10] D. Grady. Physics of shock and impact, Volume 1: fundamentals and dynamic failure. page 21, 2017.

[11] D. Hayes, R. S. Hixson and R. G. McQueen. High pressure elastic properties, solid-liquid phase boundary and liquid equation of state from release wave measurements in shock-loaded copper. *AIP Conference Proceedings*, 505:483, 2000.

[12] N. Stringfellow. Obtaining scalable performance from molecular dynamics codes on HPC machines. 2002.

[13] B. J. Alder and T. E. Wainwright. Studies in molecular dynamics. I: General method. *The Journal of Chemical Physics*, 31(2):459, 1959.

[14] J. Roth, F. Gähler and H. R. Trebin. A molecular dynamics run with 5,180,116,000 particles. *International Journal of Modern Physics C*, 11(2):317, 2000.

[15] D. Alfè. Temperature of the inner-core boundary of the Earth: melting of iron at high pressure from first-principles coexistence simulations. *Physical Review B*, 79(6):060101, 2009.

[16] L. Burakovsky, S. P. Chen, D. L. Preston, A. B. Belonoshko, A. Rosengren, A. S. Mikhaylushkin, S. I. Simak and J. A. Moriarty. High-pressure - high-temperature polymorphism in Ta: resolving an ongoing experimental controversy. *Physical Review Letters*, 104:255702, 2010.

[17] S. Plimpton. Fast parallel algorithms for short-range molecular dynamics. *Journal of Computational Physics*, 117(1):1–19, 1995.

[18] S. Plimpton. LAMMPS user's manual. *Sandia National Laboratories*, 2017.

[19] M. F. Guest, A. M. Elena and A. B. G. Chalk. DL_POLY - A performance overview analysing, understanding and exploiting available HPC technology. *Molecular Simulation*, 47(2):194, 2021.

[20] M. S. Daw and M. I. Baskes. Embedded-atom method: derivation and application to impurities, surfaces, and other defects in metals. *Physical Review B*, 29(12):6443–6453, 1984.

[21] G. Manai and F. Delogu. Homogeneous and heterogeneous melting behavior of bulk and nanometer-sized Cu systems: a numerical study. *Journal of Materials Science*, 42:6672, 2007.

[22] G. Kimminau, P. Erhart, E. M. Bringa, B. Remington and J. S. Wark. Phonon instabilities in uniaxially compressed FCC metals as seen in molecular dynamics simulations. *Physical Review B*, 81(9):092102, 2010.

[23] R. Ravelo, L. Holian, T. C. Germann and P. S. Lomdahl. Constant-stress Hugoniostat method for following the dynamical evolution of shocked matter. *Physical Review B*, 70(1):014103, 2004.

[24] Z. H. Jin, P. Gumbsch, K. Lu and E. Ma. Melting mechanisms at the limit of superheating. *Physical Review Letters*, 87(5):055703, 2001.

[25] F. Spaepen. Homogeneous nucleation and the temperature dependence of crystal-melt interfacial tension. *Solid State Physics*, 47, 1994.

[26] T. P. Duy and V. V. Hoang. Atomic mechanism of homogeneous melting of BCC Fe at the limit of superheating. *Physica B*, 407:978, 2012.

[27] K. Lu and Y. Li. Homogeneous nucleation catastrophe as a kinetic stability limit for superheated crystal. *Physical Review Letters*, 80(20):4474, 1998.

[28] S. A. Cho. Role of lattice structure on the Lindemann fusion theory of metals. *Journal of Physics F: Metal Physics*, 12(6):1069–1083, 1982.

[29] J. Wang, S. Yip, S. R. Phillpot, and D. Wolf. Crystal instabilities at finite strain. *Physical Review Letters*, 71(25):4182–4185, 1993.

[30] Z. H. Jin, P. Gumbsch, K. Lu, E. Ma. Melting mechanisms at the limit of superheating. *Physical Review Letters*, 87(5):055703, 2001.

[31] G. Kimminau, B. Nagler, A. Higginbotham, W. J. Murphy, N. Park, J. Hawreliak, K. Kadau, T. C. Germann, E. M. Bringa, D. H. Kalantar, H. E. Lorenzana, B. A. Remington and J. S. Wark. Simulating picosecond X-ray diffraction from shocked crystals using post-processing molecular dynamics calculations. *Journal of Physics: Condensed Matter*, 20:505203, 2008.

[32] M. G. Gorman, R. Briggs, E. E. McBride, A. Higginbotham, B. Arnold, J. H. Eggert, D. E. Fratanduono, E. Galtier, A. E. Lazicki, H. J. Lee, H. P. Liermann, B. Nagler, A. Rothkirch, R. F. Smith, D. C. Swift, G. W. Collins, J. S. Wark and M. I. McMahon. Direct observation of melting in shock-compressed bismuth with femtosecond X-ray diffraction. *Physics Review Letters*, 115(9):1–5, 2015.

[33] A. B. Belonoshko and A. Rosengren. High-pressure melting curve of platinum from ab initio z method. *Physical Review B*, 85(17):174104(1–7), 2012.

[34] J. Bouchet, F. Bottin, G. Jomard and G. Zèrah. Melting curve of aluminum up to 300 GPa obtained through ab initio molecular dynamics simulations. *Physical Review B*, 80(9):094102, 2009.

[35] S. N. Luo. Non equilibrium melting and crystallization of a model Lennard-Jones system. *The Journal of Chemical Physics*, 120(24):11640, 2004.

[36] A. B. Belonoshko. Melting of corundum using conventional and two-phase molecular dynamic simulation method. *Physics and Chemistry of Minerals*, 25:138, 1998.

[37] J. R. Morris, C. Z. Wang, K. M. Ho and C. T. Chan. Melting line of aluminium from simulations of coexisting phases. *Physical Review B*, 49(5):3109, 1994.

[38] J. R. Morris and X. Song. The melting lines of model systems calculated from coexistence simulations. *The Journal of Chemical Physics*, 116(21):9352, 2002.

[39] S. Wang, G. Zhang, H. Liu and H. Song. Modified Z method to calculate melting curve by molecular dynamics. *The Journal of Chemical Physics*, 138(13):134101, 2013.

[40] A. B. Belonoshko, N. V. Skorodumova, A. Rosengren and B. Johansson. Melting and critical superheating. *Physical Review B*, 73(1):012201, 2006.

[41] D. Alfè, C. Cazorla and M. J. Gillan. The kinetics of homogeneous melting beyond the limit of superheating. *The Journal of Chemical Physics*, 135(2):024102, 2011.

[42] S. Vyazovkin. Power law and Arrhenius approaches to the melting kinetics of superheated crystals: are they compatible? *Crystal Growth and Design*, (18):6389−6392, 2018.

[43] T. Liavitskaya, L. Birx and S. Vyazovkin. Melting kinetics of superheated crystals of glucose and fructose. *Physical Chemistry Chemical Physics*, 19:26056, 2017.

[44] C. Daia, J. Hu and H. Tan. Hugoniot temperatures and melting of tantalum under shock compression determined by optical pyrometry. *Journal of Applied Physics*, 106:043519, 2009.

[45] P. G. Heighway, M. Sliwa, D. McGonegle, C. Wehrenberg, C. A. Bolme, J. Eggert, A. Higginbotham, A. Lazicki, H. J. Lee, B. Nagler, H.-S. Park, R. E. Rudd, R. F. Smith, M. J. Suggit, D. Swift, F. Tavella, B. A. Remington and J. S. Wark. Nonisentropic release of a shocked solid. *Physical Review Letters*, 123(24):245501, 2019.

[46] B. Romanowicz, A. Dziewonski and G. Schubert. Treatise on geophysics, volume 1: deep Earth seismology. page 396, 2015.

[47] J. W. Enig. A complete E, P, V, T, S thermodynamic description of metals based on the P-u mirror image approximation. *Journal of Applied Physics*, 34(4):746, 1963.

[48] H. Tan and T. J. Ahrens. Shock temperature measurements for metals. *International Journal of High Pressure Research*, 2(3):159–182, 1990.

[49] J. M. Walsh and R. H. Christian. Equation of state of metals from shock wave measurements. *Physical Review*, 97(6):1544, 1955.

[50] S. L. Pistinner, S. Pecker, M. Werdiger, and S. Eliezer. On the maximal deviation from the mirror image approximation due to solid liquid phase transition. *AIP Conference Proceedings*, 955:185–188, 2007.

[51] H. Liu, H. Song, Q. Zhang, G. Zhang and Y. Zhao. Validation for equation of state in wide regime: copper as prototype. *Matter and Radiation at Extremes*, 1:123–131, 2016.

[52] D. Grady. Physics of shock and impact, Volume 1: fundamentals and dynamic failure. pages 58–59, 2017.

[53] W. J. Gray, M. E. Foord, M. B. Schneider, M. A. Barrios, G. V. Brown, R. F. Heeter, L. C. Jarrott, D. A. Liedahl, E. V. Marley, C. W. Mauche and K. Widmann. Investigation of the hydrodynamics and emission of a laser heated tamped high-z target. *Physics of Plasmas*, 25(6):062702, 2018.

[54] J. Coakley, A. Higginbotham, D. McGonegle, J. Ilavsky, T. D. Swinburne, J. S. Wark, K. M. Rahman, V. A. Vorontsov, D. Dye, T. J. Lane, S. Boutet, J. Koglin, J. Robinson and D. Milathianaki. Femtosecond quantification of void evolution during rapid material failure. *Science Advances*, 6(51):1–10, 2020.

[55] L. Vočadlo, D. Alfè, G. D. Price and M. J. Gillan. Ab initio melting curve of copper by the phase coexistence approach. *Journal of Chemical Physics*, 120(6):2872, 2004.

[56] J. A. Moriarty, J. F. Belak, R. E. Rudd, P. Soderlind, F. H. Streitz and L. H Yang. Quantum-based atomistic simulation of materials properties in transition metals. *Journal of Physics Condensed Matter*, 14(11):2825, 2002.

[57] C. Dai, H. Tan and H. Geng. Model for assessing the melting on Hugoniots of metals: Al, Pb, Cu, Mo, Fe and U. *Journal of Applied Physics*, 92(9):5019, 2002.

[58] http://lammps.sandia.gov. (Date viewed 20/12/2021).

[59] H. W. Sheng, M. J. Kramer, A. Cadien, T. Fujita and M. W. Chen. Highly optimized embedded-atom-method potentials for fourteen FCC metals. *Physical Review B*, 83(13):134118, 2011.

[60] https://sites.google.com/site/eampotentials/. (Date viewed 20/12/2021).

[61] A. Stukowski. Visualization and analysis of atomistic simulation data with OVITO–the Open Visualization Tool. *Modelling and Simulation in Materials Science and Engineering*, 18(1):1–7, 2010.

[62] Y. A. Chang and L. Himmel. Temperature dependence of the elastic constants of Cu, Ag and Au above room temperature. *Journal of Applied Physics*, 37(9):3567, 1966.

[63] J. W. Arblaster. Thermodynamic properties of copper. *Journal of Phase Equilibria and Diffusion*, 36(5):422, 2015.

[64] Z. L. Liu, L. C. Cai, X. R. Chen and F. Q. Jing. Molecular dynamics simulations of the melting curve of tantalum under pressure. *Physical Review B*, 77(2):024103, 2008.

[65] G. P. P. Pun, K. A. Darling, L. J. Kecskes and Y. Mishin. Angular-dependent interatomic potential for the Cu–Ta system and its application to structural stability of nano-crystalline alloys. *Acta Materialia*, 100:377, 2015.

[66] X. W. Zhou, R. A. Johnson and H. N. G. Wadley. Misfit-energy-increasing dislocations in vapor-deposited CoFe/NiFe multilayers. *Physical Review B*, 69(14):144113, 2004.

[67] R. Ravelo, T. C. Germann, O. Guerrero, Q. An and B. L. Holian. Shock-induced plasticity in tantalum single crystals: Interatomic potentials and large-scale molecular-dynamics simulations. *Physical Review B*, 88(13):134101, 2014.

[68] http://www.ihed.ras.ru/rusbank/. (Date viewed 20/12/2021).

[69] A. Higginbotham, S. Patel, J. A. Hawreliak, O. Ciricosta1, G. W. Collins, F. Coppari, J. H. Eggert, M. J. Suggit, H. Tang and J. S. Wark. Single photon energy dispersive X-Ray diffraction. *Review of Scientific Instruments*, 85(3):033906, 2014.